IN SITU NONDESTRUCTIVE EVALUATION OF IN-PHASE THERMOMECHANICAL FATIGUE AND SUSTAINED LOAD DAMAGE IN AN SCS-6/TI-6AL-4V METAL MATRIX COMPOSITE

Thesis Submitted to:

Graduate Engineering & Research
School of Engineering

UNIVERSITY OF DAYTON

In Partial Fulfillment of the Requirements for

The Degree

Master of Science in Materials Engineering

by

Gregory Scott Clemons

UNIVERSITY OF DAYTON

Dayton, Ohio

May 1997

***IN SITU* NONDESTRUCTIVE EVALUATION OF IN-PHASE THERMOMECHANICAL FATIGUE AND SUSTAINED LOAD DAMAGE IN AN SCS-6/TI-6AL-4V METAL MATRIX COMPOSITE**

Approved by:

Prasanna Karpur, Ph.D.
Advisory Committee Chairman
Associate Professor, Graduate Chemical and Materials Engineering Department

David A. Stubbs
Committee Member
Research Engineer
University of Dayton Research Inst.

Daniel Eylon, Ph.D.
Committee Member
Professor, Graduate Chemical and Materials Engineering Department

Noel E. Ashbaugh, Ph.D.
Committee Member
Senior Research Engineer
University of Dayton Research Inst.

Theodore Nicholas, Ph.D.
Committee Member
Senior Scientist, Materials Directorate, USAF

Donald L. Moon, Ph.D.
Associate Dean
Graduate Engineering Programs & Research
School of Engineering

Joseph Lestingi, D. Eng., P.E.
Dean, School of Engineering

ABSTRACT

IN SITU NONDESTRUCTIVE EVALUATION OF IN-PHASE THERMOMECHANICAL FATIGUE AND SUSTAINED LOAD DAMAGE IN AN SCS-6/TI-6AL-4V METAL MATRIX COMPOSITE

Name: Clemons, Gregory Scott
University of Dayton, 1997

Thesis Advisor: Dr. Prasanna Karpur
Technical Advisor: Mr. David A. Stubbs

This study demonstrated that *in situ* nondestructive ultrasonic longitudinal wave and acoustic emission techniques can monitor the onset and accumulation of damage produced by either sustained loading or in-phase thermomechanical fatigue loading in a titanium matrix composite. Damage was monitored in a unidirectional $[0]_8$ SCS-6/Ti-6Al-4V composite *in situ* as a function of time at elevated temperature. Acoustic emission nondestructive techniques were utilized because of their ability to detect internal damage occurring within a material.

Damage progression was monitored by complementary destructive and nondestructive techniques. Damage evaluation of unidirectional $[0]_8$ SCS-6/Ti-6Al-4V metal matrix composite (MMC) tested at elevated temperature was achieved using *in situ* nondestructive ultrasonic longitudinal wave and acoustic emission techniques, and subsequently verified with the use of ultrasonic immersion backscatter shear wave C-scans and metallographic techniques. The *in situ* data showed that the higher the stress level, the more abrupt the damage initiation and progression.

Detection and characterization of damage accumulation was achieved with the use of *in situ* nondestructive ultrasonic longitudinal bulk wave and acoustic emission techniques in conjunction with current load-displacement modulus measurements. The location of damage accumulation within the specimen also was determined from the acoustic emission *in situ* technique. Ultrasonic modulus data correlated well with traditional extensometry data, however, neither technique provided information on damage accumulation or impending fractutre of the composite. Ultrasonic amplitude information however, did, provide information on damage accumulation within the composite. Acoustic emission data provided information on damage characterization, damage progression and accumulation, and the location of the damage occurring within the composite material.

The *in situ* nondestructive data allowed a correlation to be developed between sustained load and in-phase thermomechanical fatigue life. Through mechanical and fracture analysis, similarities in damage progression in sustained load and in-phase thermomechanical fatigue specimens were determined. Nondestructive data in conjunction with mechanical data and fracture analysis conclusively showed the ability to correlate the results of the two testing conditions. An inefficiency factor of 15% was estimated from an empirical fit of the mechanical test data for a stress range of 100 MPa below the estimated UTS of the material.

ACKNOWLEDGMENTS

Funding for this project was provided through the Air Force Office of Scientific Research Grant No. F49620-93-1-0461DEF, Program Manager Dr. Walter F. Jones; partial support from Air Force Contract No. F33615-94-C-5213 and F33165-94-C-5200. I would like to offer my thanks to Dr. Prasanna Karpur, my thesis advisor, for providing the opportunity for me to obtain this degree. His time spent directing my work and bringing it to a conclusion is much appreciated. I would also like to thank my technical advisor, Mr. David A. Stubbs, for all of his help in completing this study.

I would like to thank the government and contractor personnel at the Metals, Ceramics and Nondestructive Evaluation Division, both Ceramics Development and Materials Behavior Branch, and Nondestructive Evaluation Branch, Wright Laboratory Materials Directorate Wright-Patterson Air Force Base, OH: Dr. Theodore Nicholas, for providing the area of study and information on fiber fracture; Jay R. Jira, for providing the material necessary for this thesis; Dr. Andrew H. Rosenberger, for allowing the use of IP TMF data and for providing insight into the use of acoustic emission and TMF equipment; Dr. Noel Ashbaugh, for sharing his data and insights on sustained load of composites; Ms. Debbie Garner, for aid in determining fiber fractures within the material and fiber strength of the composite; Dr. Reji John and Mr. Dennis Buchanan for sharing their insights on the use of the ultrasonic bulk wave technique at room temperature; and the NDE branch for providing the NDE data collection facilities and equipment.

I would also like to thank other fellow UDRI employees from the Nondestructive Evaluation Branch at Wright Patterson AFB: Mr. Jeffrey A. Fox, for his aid with all computer equipment; Mr. Mark Ruddell, for giving his aid in the area of electronics; Dr. S. Sathish and Dr. Theodore Matikas, for sharing their knowledge of wave theory and ultrasonic immersion scanning techniques.

I would like to express my sincere gratitude to Dr. Mike Gorman for his trip to Wright Patterson Air Force Base. His knowledge of modal acoustic emission, event characterization and location proved invaluable in analysis of the acoustic emission data acquired from the mechanical tests.

I would like to thank those people closest to me, my family, especially my mom and dad who made this all possible. Finally, my deepest thanks goes to my loving companion and soon to be wife, Monda for all of her support through these rough times.

PREFACE

A multitude of nondestructive studies have been and are being performed on composite materials to evaluate and characterize composite behavior under simulated operating conditions. The University of Dayton Research Institute (UDRI), under contract with the United States Air Force, has performed nondestructive evaluation of ceramic matrix composites and metal matrix composites. During the course of expanding the nondestructive evaluation effort, the need to use *in situ* nondestructive techniques to characterize such damage initiation and progression as fiber fracture, matrix cracking and fiber/matrix interfacial failure has become apparent. The purpose of this thesis is to attempt to respond to that need. By tracking damage progression, different test conditions such as sustained load and thermomechanical fatigue may be able to be compared on the basis of time-to-failure.

TABLE OF CONTENTS

LIST OF ILLUSTRATIONS

Figure **Page**

Figure **Page**

LIST OF SYMBOLS AND ABBREVIATIONS

(in alphabetical order)

SYMBOLS

at. %	Atomic Percent
c_l	Longitudinal Bar Wave Velocity
d	Distance form source to sensor
E_c	Composite Modulus
E_f	Fiber Modulus
E_m	Matrix Modulus
f	Frequency
λ	Wavelength
ν	Poisson's Ratio
ν_f	Fiber Volume Fraction
ν_m	Matrix Volume Fraction
σ_c	Composite Stress
σ_f	Fiber Stress
σ_m	Matrix Stress
σ_{max}	Maximum Stress
σ_{min}	Minimum Stress
R	Stress Ratio
ρ	Density

ABBREVIATIONS

A/D	Analog to Digital
AE	Acoustic Emission
BW	Bulk Wave
CMF	Carbon Monofilament
CTE	Coefficient of Thermal Expansion
CVD	Chemical Vapor Deposition
DAC	Data Acquisition Cycle
FFT	Fast Fourier Transform
FWD	Fracture Wave Detector
HIP	Hot Isostatic Pressing
IP	In-Phase
LMP	Larson-Miller Parameter
MATE	Materials Testing and Environment
MMC	Metal Matrix Composite
NDE	Nondestructive Evaluation
OP	Out-of-Phase
PC	Personal Computer
PID	Proportional Integral Derivative
ROM	Rule of Mixtures
RT	Room Temperature
SAM	Scanning Acoustic Microscopy
SEM	Scanning Electron Microscopy
SiC	Silicon Carbide
TMC	Titanium Matrix Composite
TMF	Thermomechanical Fatigue
TOF	Time of Flight
UDRI	University of Dayton Research Institute
UT	Ultrasonic
UTS	Ultimate Tensile Strength
WPAFB	Wright-Patterson Air Force Base

CHAPTER I.

INTRODUCTION

1.1 Composites Research

Structural and propulsion systems for aerospace applications require low density, high modulus materials with high strength and the capacity to endure large stresses and temperature gradients over extended periods of time. Neither naturally occurring metals nor metal alloys can meet all these requirements. Therefore, anisotropic, heterogeneous composite materials have been developed which can be tailored to an application (e.g., aerospace vehicles, advanced engine components, actuator rods, etc.). Titanium matrix composites (TMC), which are a specific type of metal matrix composite (MMC), are designed to offer unique advantages in terms of a variety of weight-specific properties at high temperatures [1].

The TMC, like all materials, are susceptible to failure at some point in operation. The goal of nondestructive evaluation (NDE) is to determine when the material should be repaired or replaced in order to eliminate material failures during operation. The various types of failure modes in a composite are 1) matrix dominated, 2) fiber dominated, 3) self-similar damage growth, and 4) fiber/matrix interfacial failures [2-6]. The failure mode depends on the operational conditions, such as environment and load to which the composite is exposed.

Environmental conditions affect composite life and failure mechanisms. Vacuum conditions, for instance, reduce oxidation of the MMC at high temperatures. However, vacuum conditions are rarely present in such applications as turbine engines, therefore, most testing is performed in laboratory air to simulate actual service conditions. Metal matrix composites also are not always operated at room temperature as sometimes they can reach temperatures exceeding 650°C in aircraft engine applications [7]. Therefore, composite testing must be done to determine the effects of the environment on composite life and failure mechanism.

Composites can experience various types of loading conditions including sustained load (creep) and in-phase thermomechanical fatigue (IP TMF). The effects of these specific loading conditions are currently being studied on SCS-6/Ti-6Al-4V composites by several researchers [8-10]. Data analysis has led to the belief that the two dissimilar loading conditions have a very similar effect on composite failure. Nicholas [11] has stated that the IP TMF test is an inefficient sustained load test based on theoretical modeling of fiber stress.

Information regarding the damage mechanisms occurring in a composite has been acquired mainly by analyzing mechanical, metallographic and nondestructive data after testing specimens in simulated environments under conditions representative of the service conditions. However, *in situ* nondestructive techniques are being used more prominently today in conjunction with destructive testing to offer more information as to the type and severity of damage occurring in the specimen during testing [12-14]. NDE can supplement the knowledge of the damage mechanisms of composites by not only

detecting and locating, but also characterizing flaws and defects, which leads to useful information regarding the failure modes and mechanisms in TMC. The ability to fully characterize TMC allows for the comparison of different load conditions applied to composite materials. The results of the comparison may lead to a correlation between the loading conditions.

1.2 Background

TMC are being considered for a multitude of applications that would expose the material to various operating conditions. Mechanical tests must be designed to characterize material response before mass production of the structural components begins. At the early stages of composite design, production and testing are very expensive processes. An attempt is being made to eliminate unnecessary tests by developing correlations between various loading conditions. Nicholas and Johnson [11] have developed a theory that sustained load and IP TMF time-to-failure could be compared using an inefficiency factor. A brief explanation of composite response to sustained load and IP TMF conditions is necessary to understand the similarities and differences between them.

1.2.1 Sustained Load Composite Response

The sustained load test maintains the specimen at constant load and temperature throughout the life of the material. When a composite specimen is under a sustained load, the strain accumulation rate is usually several orders of magnitude less than if the matrix alone is tested under identical conditions. Upon initial loading of a composite specimen, the applied load is distributed between the fiber and matrix. As time progresses, the

creep rate of the composite decreases to a level close to the creep rate of the fiber. To obtain steady state conditions, Khobaib et al. [15] reported that the matrix must relax to a very low stress level below the applied stress to exhibit a creep rate equivalent to the fiber alone. Several models have been developed to predict the sustained load response of MMC [16-19]. A model developed by Coker [20] theoretically determined the stresses existing in the components of the composite; results from the model are depicted in Appendix G. In theory, to allow the matrix to relax to extremely low stress levels, the fibers must carry the greater portion of the total load. Khobaib [21] has determined that the matrix stress can reduce to approximately 10% of the initial value in a short time. There is a rapid increase in stress in the fibers and the failure mode becomes fiber dominated. Matrix relaxation and individual fiber fracture increase the stresses in the remaining fibers and eventually, the applied stress to the fibers becomes larger than the fiber strength distribution. Once the applied stress surpasses the fiber strength distribution, the fibers can no longer support the applied load, and the composite fails.

1.2.2 IP TMF Composite Response

IP TMF combines a constant cyclic stress and temperature such that the maximum and minimum temperature and stress coincide. The failure mechanism is fiber dominated due to high fiber stress range and relaxation of the matrix [11, 20, 22]. In a study by Nicholas and Johnson [11], the cyclic contribution to damage accumulation was found to be a result of time-dependent phenomena. By treating the process as time dependent, Nicholas and Johnson were able to demonstrate that sustained load data and sustained load/fatigue data constitute a single population of failure times as a function of

maximum applied stress. Nicholas and Johnson then theorized that an IP TMF test could be considered as an inefficient method of sustained load testing [11]. Figure 1 hypothetically shows the portion of IP TMF cycle that represents sustained load (creep) type damage. *In situ* NDE analysis in this work is meant to help in the determination of the validity of the statement by Nicholas and Johnson by providing data on damage mechanisms and damage location. The NDE data in addition to mechanical test results may provide information on the stress range over which the inefficiency factor is valid.

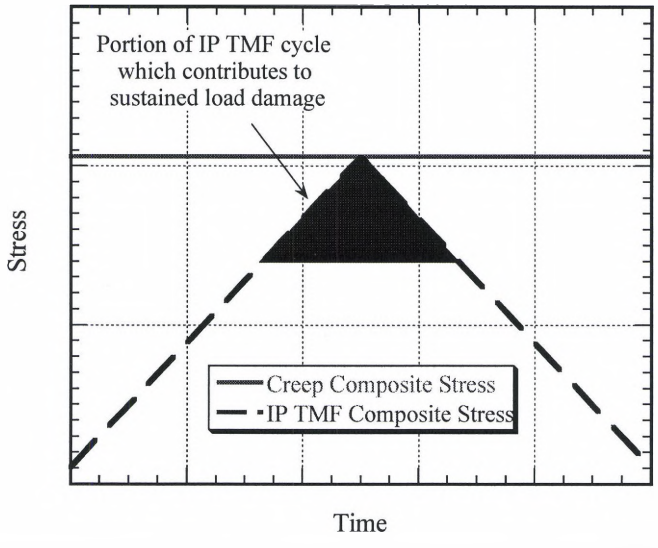

Figure 1. Comparison of IP TMF cycle to sustained load conditions for inefficiency factor determination.

A schematic depicting ideal material response to sustained load and IP TMF conditions is shown in Figure 2. The IP TMF response deviates from sustained load response as the applied stress is decreased. Therefore only a small stress region near the ultimate tensile strength of the material may be used in the comparison of the two loading conditions.

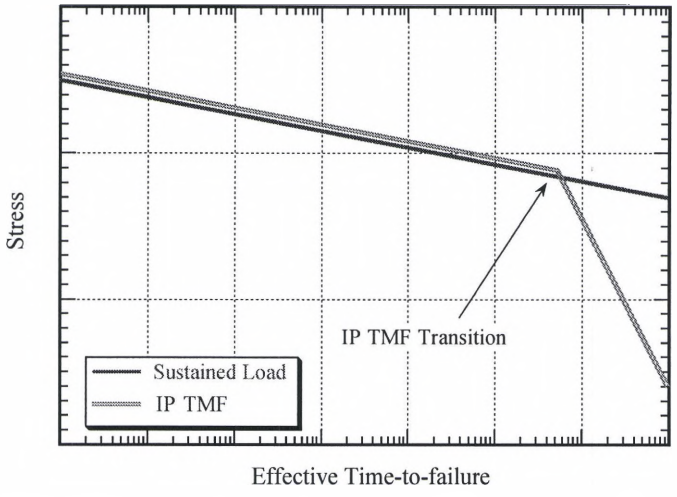

Figure 2. Ideal sustained load and IP TMF material response. IP TMF response exhibits a transition as stress is decreased due to a change in damage progression mechanisms.

1.3 Objective

The main objective was to characterize damage mechanisms in an SCS-6/Ti-6-4 composite under sustained load and IP TMF, to draw a conclusion on the similar or dissimilar type of damage accumulation, and to compare the two test results based on time-to-failure over a range of stress levels. The characterization and comparison was achieved with the aid of the following *in situ* nondestructive techniques:

1) Ultrasonic longitudinal bulk rod wave analysis.
2) Modal acoustic emission analysis.

Several techniques were used in an attempt to corroborate and validate the *in situ* analysis:

1) Mechanical test data.
2) Metallographic and fracture analysis using scanning electron microscopy.
3) X-ray radiography
4) Ultrasonic immersion reflector plate, surface wave, and backscatter shear wave scans.

1.4 Methodology and Test Plan

1.4.1 Test Design Parameters

The maximum load and temperature applied in the sustained load and IP TMF tests corresponded with conditions used by Ashbaugh [8] and Rosenberger [9] to generate the baseline mechanical test data. Baseline tensile, sustained load and IP TMF data generated by Ashbaugh [8] and Rosenberger [9] at Wright Laboratory Materials Directorate Wright-Patterson AFB, OH were analyzed to select appropriate mechanical test load levels and interruption points for ultrasonic immersion C-scanning and residual strength testing. Due to unexpected failure of the composite specimens, however, no residual strength testing was possible. The maximum applied stress range was between 70% and 90% of the UTS value of the material at 427°C. Comparable stress levels were chosen to compare with baseline material tested under the same conditions. Stress levels also were chosen to compare the IP TMF and sustained load conditions at exact stress values. All sustained load tests were performed in load-control at 427°C. All IP TMF tests were performed in load-control at a maximum temperature of 427°C and a minimum temperature of 23°C (room temperature). The IP TMF tests were performed in sawtooth waveform tension-tension fatigue with a stress ratio, R, of 0.05 and a cycle time of 100 seconds. Baseline curves and *in situ* ultrasonic and acoustic emission data were used in the determination of interruption points during the mechanical tests. The *in situ* nondestructive ultrasonic and acoustic emission techniques monitored damage accumulation throughout all sustained load and IP TMF mechanical tests.

1.4.2 Correlation of Observed Damage With Material Life

Post mechanical test NDE C-scans were performed to locate damage accumulation within the composite that could be correlated to *in situ* data. Metallographic techniques were used to verify *in situ* NDE findings. The metallographic results along with NDE data and mechanical data were used to determine a failure scenario. All data were used to determine the extent of a correlation between sustained load and IP TMF life prediction.

Following the post mechanical test NDE analysis of the specimens, the specimens were sectioned, mounted, polished, and analyzed using various metallographic techniques such as optical and electron microscopy and microhardness testing to determine the reason for short composite life. One specimen was interrupted and the matrix material was dissolved to count fiber fractures and determine fiber fracture locations. The post test analysis information was compared with the NDE *in situ* test results. All other post mechanical test NDE information was used to determine the sensitivity of the *in situ* NDE techniques to damage progression within the composite, and the capability of the *in situ* NDE techniques to locate damage initiation and progression in the form of internal crack growth within the composite. The *in situ* data supported the comparison of the sustained load and IP TMF test conditions and helped to develop the time-to-failure inefficiency factor.

1.4.3 Comprehension of Damage Mechanisms

Metallography and scanning electron microscopy were used to verify and characterize damage detected by nondestructive evaluation. The information obtained about the fracture surface from scanning electron microscopy explained the short material

life. The existence of early fiber fracture and internal matrix crack growth were compared with NDE information. SEM examination of the fracture surfaces supported NDE and mechanical data in determining a failure scenario.

CHAPTER II.

MATERIAL AND EQUIPMENT

2.1 Titanium Matrix Composites

TMC are being developed for critical aerospace structural applications, however, many processing inconsistencies such as undulated fibers, fiber coating thickness, and inclusions, such as those observed in the SCS-6/Ti-6Al-4V composite, must be eliminated. Once processing errors are eliminated, the TMC may replace titanium and nickel-base superalloys in aerospace applications. The SCS-6/Ti-6Al-4V TMC was manufactured by Textron Specialty Materials Division for the PRDA IV program under contract No. F33601-95-C-0029 for the Materials Directorate at WPAFB.

The TMC was an 8-ply unidirectional SCS-6/Ti-6Al-4V metal matrix composite. The SCS-6/Ti-6Al-4V TMC is an alpha-beta titanium-base alloy with embedded continuous silicon carbide fibers designated SCS-6 by Textron. The fibers constitute approximately 34% of the total volume of the composite. Appendix C contains detailed information on the constituents, their mechanical properties, and the processing of the composite.

2.2 Specimen Description

The composite panel was machined by Bomas Machine Specialties, Inc. machining company (Somerville, MA) into dogbone shaped specimens using a diamond saw to cut and grind the material. The diamond saw gives the specimens smooth edges, a necessity for contact ultrasonic analysis. A smooth flat surface allows for good contact between transducer and specimen, which provides high signal clarity.

Figure 3 provides a comparison of the geometry of the long, NDE specimens, and the geometry of the short, baseline specimens tested by Rosenberger and Ashbaugh. An additional inch is added to the tab length to allow for the *in situ* NDE techniques to be incorporated into the test frame. All material in the PRDA IV program was required to go through a second HIP process as would material going into aircraft application. The individual specimens were C-scanned before mechanical testing began. All information on test specimen C-scans can be found in Appendix A.

2.2.1 Baseline Samples

The information used to develop test parameters can be found in Table 1. Table 1 contains the sustained load and IP TMF testing conditions used by Ashbaugh [8] and Rosenberger [9] for the baseline samples. Stress levels and temperature ranges for *in situ* NDE mechanical testing were extracted from the baseline data.

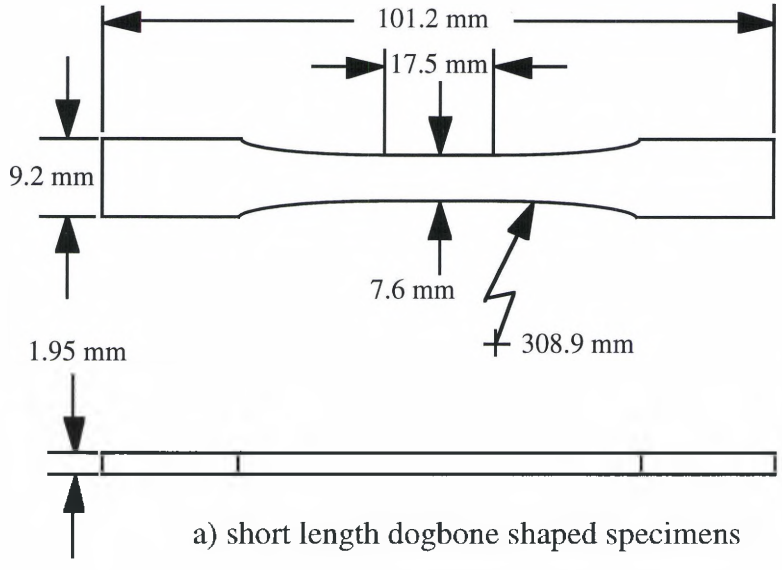

a) short length dogbone shaped specimens

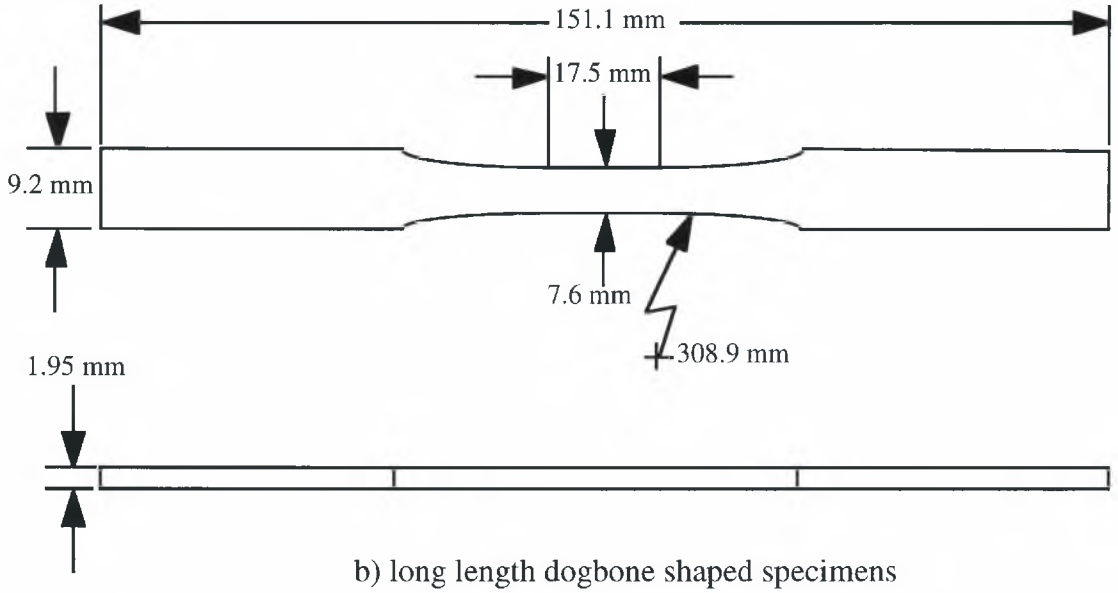

b) long length dogbone shaped specimens

Figure 3. Specimen geometry a) short length and b) long length dogboned shaped specimens. The longer specimens allowed for NDE equipment to be placed on the specimen during testing.

Table 1. Baseline Test Conditions: Sustained Load and IP TMF								
Test Type	**ID #**	**Plate #**	**Tmin (°C)**	**Tmax (°C)**	**R**	**f (Hz)**	**Max. Stress (MPa)**	**RT E (GPa)**
Baseline Sustained Load Specimens								
Creep	95713	24-6L	427	N/A	N/A	N/A	1170	N/A
Creep	95714	24-7L	427	N/A	N/A	N/A	1030	N/A
Creep	95A05	2-1L	538	N/A	N/A	N/A	1030	N/A
Creep	95A06	2-2L	427	N/A	N/A	N/A	1030	N/A
Creep	95A13	3-1L	427	N/A	N/A	N/A	1170	N/A
Creep	95A14	3-2L	538	N/A	N/A	N/A	1170	N/A
Creep	95A48	6-2L	427	N/A	N/A	N/A	1170	N/A
Creep	95A49	6-3L	427	N/A	N/A	N/A	1170	N/A
Creep	95A51	6-5L	538	N/A	N/A	N/A	827	N/A
Creep	95A53	6-7L	427	N/A	N/A	N/A	827	N/A
Baseline IP TMF Specimens								
IP TMF	95A23	4-3L	23	427	0.05	0.01	1200	188
IP TMF	95A24	4-4L	23	427	0.05	0.01	1200	207
IP TMF	95A25	4-5L	23	427	0.05	0.01	1050	207
IP TMF	95A27	4-7L	23	427	0.05	0.01	1150	223
Sustained load temperature listed in Tmin column is the constant test temperature								

2.2.2 NDE Samples

The term 'NDE samples' refers to the specimens from panel 9 of the PRDA IV project. Thirteen specimens were available for testing. Tensile test results at room temperature and 427 °C determined the strength of the composite, and the remaining specimens were designated for either sustained load or IP TMF testing conditions. Table 2 lists the specimen, geometry, and test type.

2.3 Testing Equipment

Three separate systems were necessary to collect and analyze all of the data acquired during the mechanical tests. Each system was controlled with a personal computer (PC). The mechanical test system controlled the test and acquired mechanical

data such as stress, strain, and temperature. The other two systems, also controlled by PC acquired the ultrasonic data and acoustic emission data. The ultrasonic system was manually operated, and the acoustic emission system automatically acquired acoustic signals generated by the specimen. Descriptions of each of the three systems and the equipment necessary to operate them can be found in Appendix B. Figure 4 displays all the equipment used for test control.

Table 2. NDE Specimen, Geometry, and Test Type

ID #	**Plate #**	**Geometry**	**Test Type**
96-771	9-13L1	SS	Tensile
96-772	9-1L	DB	Creep
96-773	9-2L	DB	Creep
96-774	9-3L	DB	IP TMF
96-775	9-4L	DB	IP TMF
96-776	9-5L	DB	Creep
96-777	9-6L	DB	IP TMF
96-778	9-7L	DB	Creep
96-779	9-8L	DB	IP TMF
96-780	9-9L	DB	Creep
96-781	9-10L	DB	Creep
96-782	9-11L	DB	IP TMF
96-F31	9-13L2	SS	Tensile
SS: Straight sided		DB: Dogbone shaped	

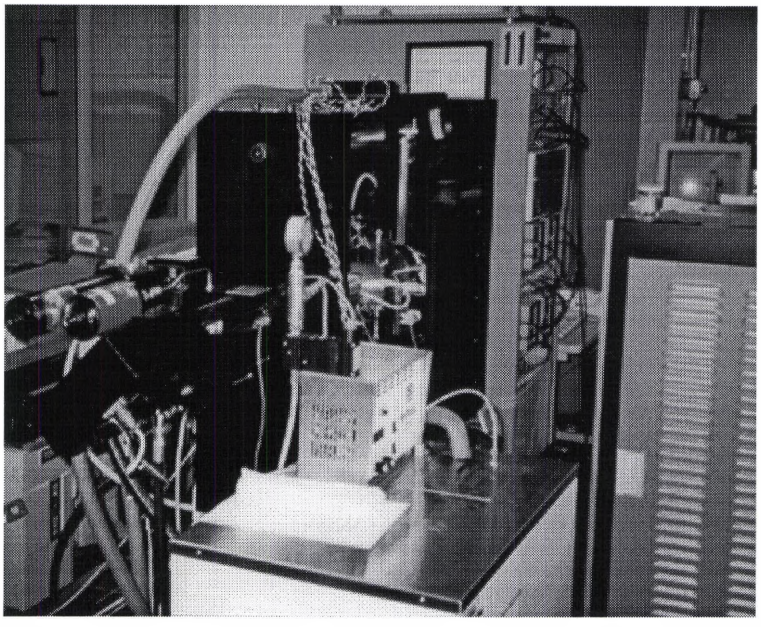

Figure 4. Test control equipment. Clockwise from bottom center: chiller, test frame, MTS controller, MATE system, nitrogen dewars, AE system (monitor on right edge), and UT system (backside shown in right bottom corner of photo).

CHAPTER III.

NONDESTRUCTIVE EVALUATION

3.1 Pre-mechanical test NDE

Nondestructive Evaluation is a very useful screening method to determine the quality of the material before mechanical testing. There are several techniques that can be performed to determine if the composite should be mechanically tested, or should be analyzed using metallographic techniques to provide information on the composite before mechanical testing. Each NDE method contributes information that together provide a complete picture as to the condition of the material. A description of the NDE techniques and the results of the techniques are described fully in Appendix A.

The NDE results revealed several potential problems with the panel. One edge of the panel contained undulated fibers, and several low amplitude (darker) regions were located in the panel using ultrasonic immersion techniques (refer to Appendix A). The low amplitude (dark) regions were examined to determine if they would cause the material to deviate from the predicted performance in mechanical testing. A higher resolution C-scan was performed to obtain more information about the condition of the panel. The scan demonstrates that the dark regions may be of serious concern due to the larger decrease in signal amplitude over those regions. Note that the three dark regions on the panel (shown in Figures 54 and 55 in Appendix A) are of a lower amplitude on the high

resolution scan than on the low resolution scan according to the scale. The severity and effect of the low amplitude regions detected using the ultrasonic immersion reflector plate C-scan will be addressed in the post mechanical test results using metallographic analysis.

The individual specimens from the panel were then C-scanned using the reflector plate technique to determine which specimens contained the dark regions. All regions were located within one specimen, 96-775, causing the specimen to be set aside unless needed. The surface wave C-scan detected scratches on the surface of some specimens, which were due to tantalum removal from the composite specimens. Tantalum protected the titanium from oxidizing during the second HIP process. Some tantalum pieces adhered to the specimen surface, and had to be removed using a razor blade. The backscatter shear wave C-scan was performed to determine if any internal cracks and defects existed in the material. No internal cracks were detected before mechanical testing. The pre-mechanical test C-scans were also used to compare with post mechanical test C-scans results to determine if any cracks were developing in the material due to the mechanical and thermal loading of the composite.

3.2 *In Situ* NDE

3.2.1 Ultrasonic Longitudinal Bulk Wave

The *in situ* ultrasonic longitudinal bulk wave technique is a relatively new technique for *in situ* applications. The *in situ* ultrasonic longitudinal bulk wave technique has been demonstrated as a useful high temperature technique [13, 14]. The longitudinal bulk wave provides information on amplitude and TOF of the ultrasonic signal traveling through the length of the composite specimens (Figure 5). Amplitude is measured from

largest positive-to-negative peak value of the longitudinal wave. The TOF is the time measured from the initial pulse from the transmitter (main bang) to the arrival of the longitudinal wave at the receiver.

Ultrasonic signal amplitude has been demonstrated as sensitive to material changes during the progression of damage [12, 13]. As damage progresses in the material, the amplitude of the ultrasonic signal decreases. The decrease in ultrasonic amplitude is due to microcracks that reflect and scatter the ultrasound, allowing less signal energy to reach the receiving transducer. The *in situ* setup is demonstrated in Figure 6.

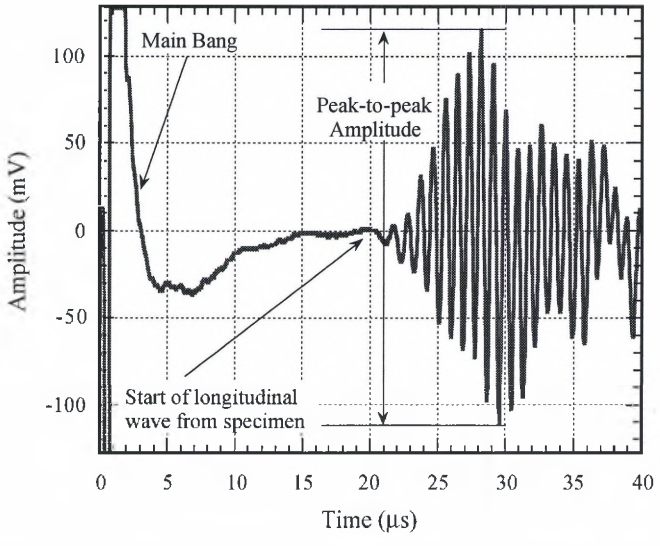

Figure 5. Sample longitudinal bulk wave signal from an SCS-6/Ti-6Al-4V composite before mechanical testing.

The TOF is the time it takes for sound to travel from the transmitter to the receiver. The TOF is very useful in characterizing a material and determining material properties and constants. By dividing the length of the material through which the sound passes by the TOF, a longitudinal velocity measurement can be calculated. The

longitudinal velocity is a key component in the determination of many material properties such as elastic modulus, shear modulus and bulk modulus of the material. The material property of interest is the elastic modulus of the composite (E_c). Changes in the elastic modulus during the test period may indicate the onset of damage.

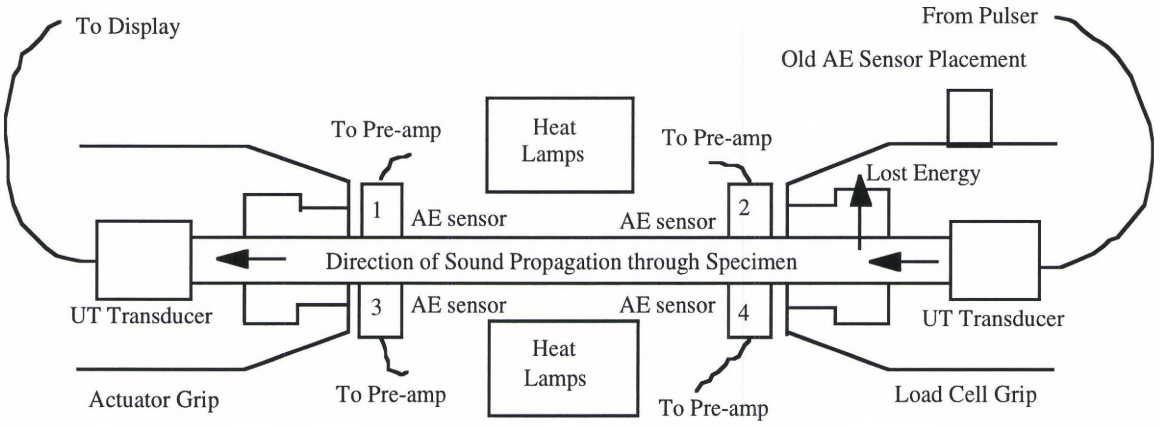

Figure 6. Schematic test set-up showing *in situ* NDE sensor placements in test frame. All sensors are held in place with spring force.

Several formulas to calculate the modulus from ultrasonic longitudinal velocity information have been developed, many of which depend on several other material properties such as density, Poisson's ratio, and the shear wave velocity. The easiest method is by creating a bar wave within the material. Bar waves are the fastest traveling longitudinal (extensional) waves in a material and are produced using sound wavelengths ≥ 10 times the specimen width. The bar wave equation offers the simplest calculation of modulus with the fewest number of unknown variables. The bar wave velocity, c_l, can be directly related to the elastic modulus, E_c, by knowing the density, ρ, of the material using the following equation

$$E_c = \rho c_l^2. \quad (1)$$

The solution can be obtained with the knowledge of the density of the composite. However, there are conditions that must be met for a bar wave to travel through a material. The wavelength must be much larger (about five to ten times greater) than the width and thickness of the bar (specimen). Table 3 lists the material dimensions and transducer specifications to determine bar wave conditions based on the wavelength needing to be ten times larger than the specimen dimensions. Note that the wavelength of sound for 200 kHz is less than half of the value necessary to meet the dimension criteria in the width dimension of the specimens.

Table 3. Calculations for Generation of a Bar Wave in SCS-6/Ti-6Al-4V

Transducer		Material Dimensions	
Frequency	200 kHz	Thickness	1.95 mm
Velocity in TMC	7.3 mm/μs	10 x thickness	19.5 mm
Wavelength in TMC	36.5 mm	Width	7.62 mm
		10 x width	76.2 mm

The exact bar (extensional) wave velocity is not obtained in the material under the conditions given in Table 3 because the specimen dimension to ultrasonic wavelength ratio is too large, but the rod wave velocity can be assumed to be valid for this case from velocity information published by Kolsky [23]. Kolsky researched rod waves, however, Morse [24, 25] was able to demonstrate the similarities in extensional waves traveling though rectangular (bar) cross sections, as is the case with MMC specimens.

One difficulty with using such low frequency signals is that small areas of damage accumulation within the specimen may not be detectable using the low frequency longitudinal bulk wave technique versus using a technique with higher ultrasonic

frequencies. Knowledge of the elastic modulus was, however, more important than detection of localized microcracks in the composite. Therefore, low frequency ultrasound was used, at the expense of detecting localized microcracks in order to correlate damage progression between the two test conditions using ultrasonic modulus analysis. The longitudinal bulk wave technique when used to monitor modulus changes in the material may offer improved accuracy in the tracking of modulus degradation due to damage accumulation.

A 200 kHz contact transducer was custom made for producing the longitudinal bulk wave. Although lower frequency transducer would have been closer to producing a rod wave in the specimen, one could not be constructed within the time constraints of the project. The accuracy of the ultrasonic modulus measurement was assessed by comparing ultrasonic modulus values with those attained from mechanical data.

3.2.2 Acoustic Emission

Acoustic emission is a passive *in situ* NDE technique. AE sensors are excited by acoustic waves produced by the material under load. Therefore, AE can only detect damage as it is occurring, it cannot detect damage that has occurred previously in the material.

Sound disperses rapidly in a thin plate-like material such as metal matrix composite specimens. Therefore, the ideal placement of acoustic sensors would be as close to the acoustic events as possible before the wave has time to deteriorate as it travels through the specimen. Placement on the specimen is not always possible due to material environment, material shape, and number of sensors necessary to keep sensor to

event distance a minimum. The development of modal acoustic emission which is based on plate wave sound propagation, allows acoustic emission waveforms emitted from the specimen to be acquired and analyzed using waveform characteristics such as amplitude, frequency, and extensional and flexural wave mode phase and group velocities.

A brief description of plate mode propagation in materials can be found in [26]. A typical waveform generated by a material under load would consist of the extensional in-plane mode, which travels at the highest velocity through a material. It is followed by the first out-of-plane flexural mode in the waveform. Detailed information on calculation of composite in-plane, bending and coupling stiffness, which is necessary for theoretical calculation of mode velocities in the material, is discussed by Whitney [27]. A more in depth discussion of plate and Lamb wave theory can be found in a paper by Graff [28], and Gorman [29]. The advantage to using classical plate wave theory is that the plate can be finite, with realistic boundaries, which allows for composite analysis [30].

The acoustic signals were analyzed to determine damage mechanisms occurring within the material. Different types of damage accumulation, such as matrix cracking, fiber fracture, and plastic deformation, can be characterized by different waveforms in both amplitude and frequency. The type of damage occurring within the material may be determined by determining the waveform characteristics. The expectation is to distinguish the different AE events as specific types of damage initiation and progression within the composite. The results of the acoustic emission signal waveform analysis will be presented in Chapter 5.

Nicholas [11] has theorized a comparison between IP TMF and sustained load conditions, in which the life prediction models are related by an inefficiency factor. The correlation between IP TMF and sustained load conditions is theorized as

$$t_{IP}(d_i) = k_t\,(t_c(d_i)), \tag{2}$$

where the time (t_{IP}) necessary to accumulate damage (d_i) in an IP TMF test related to sustained load by an inefficiency factor (k_t) of the time necessary to accumulate the same amount of damage (d_i) in an amount of time under sustained load (t_c). For previously investigated TMC material (Timetal®21S), Nicholas [11] has determined an inefficiency factor of approximately 5%. The 5% value was determined by integrating the time over which the IP TMF cycle produces damage within the composite relative to the time-to-failure for sustained load conditions. An attempt will be made to correlate damage within the composite (d_i) to *in situ* NDE parameters such as ultrasonic time of flight, signal amplitude, and acoustic emission signal characteristics and location. Figure 7 gives a graphic depiction of the theorized phenomena based upon ultrasonic amplitude.

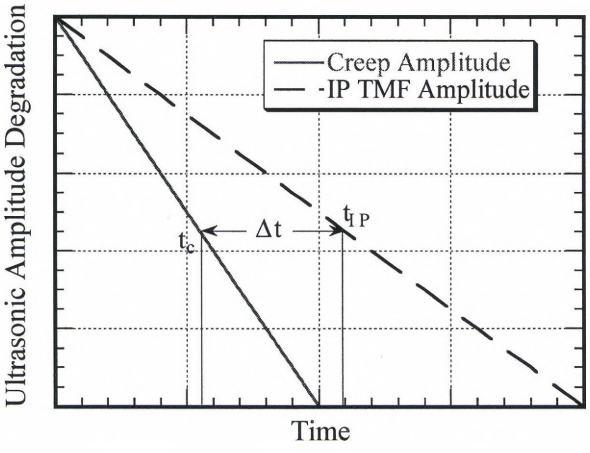

Figure 7. Hypothetical time dependent damage accumulation based on *in situ* ultrasonic bulk wave signal amplitude degradation.

3.4.2 Feasibility of NDE Techniques for Evaluating Damage Correlation

The longitudinal bulk wave (BW) NDE technique was chosen because of its applicability at high temperatures. The transducers are placed within the grip cavity in contact with the ends of the specimen, away from the heat affected zone. The transducers can be maintained at room temperature, while the material is experiencing environmental conditions that conventional transducers could not withstand. Benson's [13] *in situ* longitudinal bulk wave ultrasonic evaluation of a Sigma/Ti-6Al-2Sn-4Zr-2Mo composite sample demonstrated that the *in situ* longitudinal bulk wave ultrasonic technique may be used as a more sensitive measure of composite damage on a composite material (Figure 8). A more detailed study of longitudinal bulk wave ultrasonic evaluation is necessary, however, to support the initial findings of Benson. Longitudinal bulk wave signal amplitude degradation is clearly shown as a more sensitive technique compared to the normalized mechanical modulus measurements in detecting degradation of the composite over its fatigue life. The longitudinal bulk wave technique is applicable to other test conditions (i.e., sustained load and IP TMF at high temperatures) with similar results. A description of the sustained load and IP TMF test conditions is presented in the following chapter.

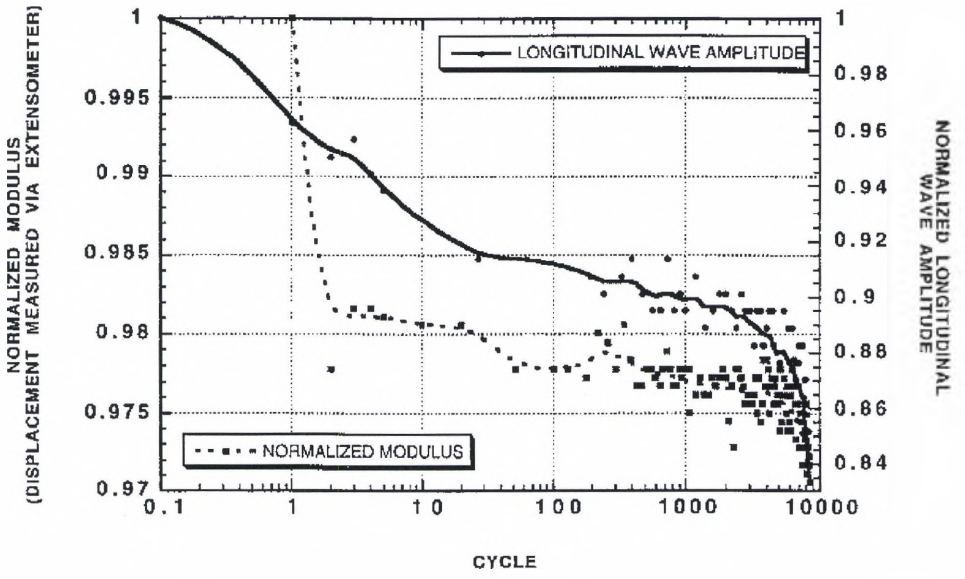

Figure 8. Comparison of normalized modulus degradation to bulk wave signal amplitude degradation vs. fatigue cycles demonstrated by Benson [13].

Acoustic emission was chosen as another NDE *in situ* technique because of its ability to detect and record sound emitted from a material as it undergoes damage. Many researchers have correlated acoustic emissions to damage occurring within the material when a load is applied [22, 48-50]. Current research with MMC has shown that different AE signals are produced by different damage mechanisms occurring within the material [22, 49-51]. A fiber fracture is characterized in the literature by a high energy, large amplitude event [22, 48]. Neu and Roman [22] and Ashbaugh [8] have attempted to correlate the number of high amplitude events (determined by a 98 dB threshold level) with the number of fiber fractures. The resonant type sensors used in previous studies, however, are incapable of resolving close events. Also the amount of information that can be analyzed to correlate AE events to fiber fractures is further reduced in the old AE system by not capturing a full AE waveform.

New broadband sensors and digital waveform AE technology allows signal frequency to be analyzed along with signal amplitude to determine the type of damage occurring, and its location within the composite. The broadband flat frequency response of the AE sensors as well as the A/D recording capabilities provided a more accurate representation of the acoustic waveform to be acquired. Therefore, along with signal amplitude information, signal frequency information and location could be determined; a tremendous breakthrough in AE technology. Figure 9 shows a typical AE waveform that was obtained with the AE sensors located on the test frame grip (refer to Figure 6). The waveform was generated by a titanium composite specimen under load. The sound must propagate from the source, through the specimen, into the grip inserts, then into the grips before the sensor detects the event. Extensive research and development was required to use the system to its fullest potential and obtain more accurate information about acoustic events than was possible with previous technology.

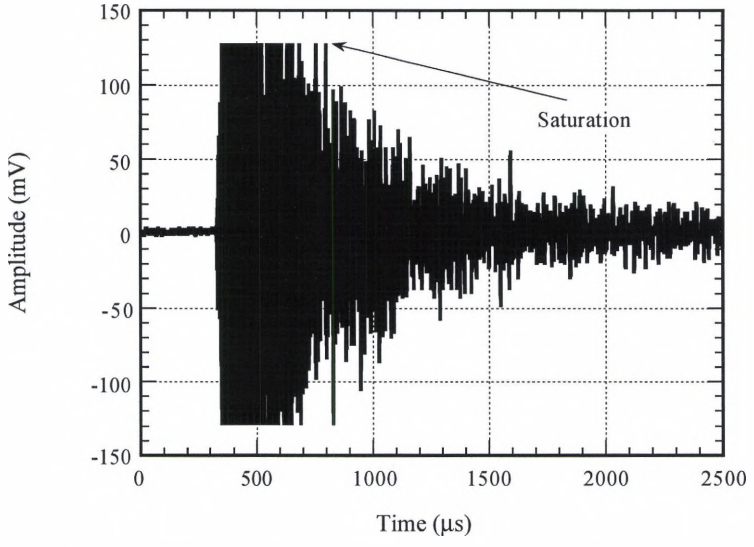

Figure 9. Acoustic Emission signal acquired on the Digital Wave Fracture Wave Detector (FWD) system with the AE sensors located on the test grips.

CHAPTER IV.

MECHANICAL TEST PROCEDURE AND RESULTS

This chapter will briefly discuss the mechanical and thermal test setup. First, the specimen dimensions and test conditions are recorded so that the operator may enter the correct information into the MATE computer program for proper test control. A sample sustained load and IP TMF log sheet is shown in Appendix D for reference. The specimen is aligned in the center of the grips to minimize bending. The specimen is then clamped into place with approximately 70 MPa of pressure applied by the hydraulic cylinder. All other information is exclusive to the test type and is discussed in each section. A brief overview of the results are listed below in Table 4.

4.1 Tensile Tests

The tensile test procedure is the least complex of the loading conditions. Once the specimen is gripped in the test machine, and the desired temperature is achieved, a ramped load is applied to the specimen until failure occurs, at which time the maximum load value is noted for the material. For elevated temperature testing, thermocouples must be welded to the specimen for temperature control and monitoring.

Table 4. Test Matrix Information						
Specimen ID	**Test Type**	**Stress (MPa)**	**Temperature (°C)**	**Modulus (GPa)**	**Failure Time (s)**	**Failure Location**
96-771	Tensile	1329	23	181	N/A	Grip
96-772	Creep	1030	427	217	6228	Interrupt
96-773	Creep	1150	427	235	2880	Gage
96-774	IP TMF	1150	427	201	23000	Gage
96-775	IP TMF	1100	427	211	400	Gage
96-776	Creep	1150	427	211	2412	Gage
96-777	IP TMF	1100	427	202	3200	Gage
96-778	Creep	1100	427	218	572	Gage
96-779	IP TMF	1050	427	201	440700	Out of Gage
96-780	Creep	1050	427	209	177300	Gage
96-781	Creep	1000	427	213	426276	Gage
96-782	IP TMF	1000	427	209	701000	Out of Gage
96-F31	Tensile	960	427	172	N/A	Gage

4.1.1 Baseline Specimens

Several composite panels from the PRDA IV program have been tested to determine the tensile strength of the material (Table 5). A wide range of UTS values in the data were attributed to variations in panel composition such as average fiber bundle strength and fiber volume fraction.

Table 5. Baseline Tensile Results						
Specimen Number	**Panel Location**	**Orientation**	**Strain Rate (s^{-1})**	**Temperature (°C)**	**Modulus (GPa)**	**UTS (MPa)**
95-691	18-1L	0°	10^{-4}	23	211	1598
95-692	18-2L	0°	10^{-4}	427	189	1463
95-693	18-3L	0°	10^{-4}	23	210	1610
95-694	18-4L	0°	10^{-4}	427	194	1450
95-718	24-11L	0°	10^{-3}	427	207	1250
95-731	25-11L	0°	10^{-3}	427	176	1090
95-743	26-10L	0°	10^{-3}	427	188	1210
95-A48	6-2L	0°	10^{-3}	427	188	1075

The experimental tensile data were compared with theoretical calculations of ultimate tensile strength and modulus using the rule of mixtures (ROM) values at room temperature obtained by using the following equations

$$E_c = \nu_f E_f + \nu_m E_m, \quad (3)$$

$$\sigma_c = \nu_f \sigma_f + \nu_m \sigma_m, \quad (4)$$

where the subscripts c, f, and m refer to the composite, fiber, and matrix, and E, σ, and ν refer to the elastic modulus, stress, and Poisson's ratio, respectively. The theoretical calculations of modulus and ultimate tensile strengths were expected to be higher than the experimental values because of low tensile values recorded testing, which are listed in Table 6. Density values are listed from documented literature provided by Textron Specialty Materials (theoretical) and experimentally from density determinations using Archimedes' method.

Table 6. Comparison of RT Experimental and Theoretical Material Properties

Experimental		**Theoretical**	
Density	3.95 g/cc	Density	3.86 g/cc
Modulus	212 GPa	Modulus	214 GPa
UTS	1329 MPa	UTS	1800 MPa

The experimental density is slightly higher than the theoretically calculated density, which indicates that the actual fiber volume fraction may be lower than the value used for calculations (34%). The possible difference in fiber volume fraction helps explain the differences in the other tabulated values.

4.1.2 NDE Specimens

Tensile tests were performed at room temperature and 427°C for panel 9 to ensure accurate values for further testing. The results of the tensile tests are listed in Table 7.

Table 7. Tensile Test Results from Panel 9

Specimen Identification	Modulus (GPa)	Temperature (°C)	UTS (MPa)
96-771	181	23	1329
96-F31	172	427	960

The tensile results were low compared to tests from other panels of the same material, but can be attributed to a slow loading rate of 10^{-5} mm/mm/s, fiber swimming, narrow specimens, and straight-sided specimen geometry. A slow loading rate may have induced creep in the specimen and reduced the tensile properties, however, the slow loading rate allowed for more ultrasonic data to be acquired during the test. UTS values were averaged with tensile results from panels of the same material to lessen the effects of this specific panel and use a more realistic tensile strength. A tensile strength of 1200 MPa was estimated at 427°C from the baseline data and previous tensile results at room and elevated temperature. The tensile strength was used to determine stress levels for the remainder of the specimens under sustained load and IP TMF conditions.

4.2 Sustained Load Tests

Once the specimen is aligned and gripped in the test machine, thermocouples are welded on the specimen for operation at elevated temperature for temperature monitoring and control. Four thermocouples are placed on the top surface of the specimen. Two are

placed 6 mm from center and two are placed 6 mm further out symmetrically about the centerline. PID controllers maintain the temperature at the required levels by adjusting the power output to the quartz lamps, which are set to a distance of approximately 10 mm above and below the horizontally mounted specimen (refer to Figure 6).

An extensometer is spring mounted on the side of the specimen to measure displacement in the gage section. Once the extensometer is in place, a room temperature modulus is obtained to ensure proper placement of the extensometer. The modulus value is obtained by loading the specimen within the elastic region to 100 MPa. The slope of the stress-strain curve is calculated using MATE software. Once the checkout procedure is complete, the sustained load test parameters are entered interactively.

Sustained load tests record creep strain and strain to failure measurements versus time. The data are used to plot results on a Larson-Miller diagram. The time-to-failure and strain accumulation are key conditions for comparison with *in situ* NDE results.

4.2.1 Baseline Specimens

The test results at various stress and temperature levels for the baseline specimens are listed in Table 8. All baseline sustained load tests were under the supervision of Ashbaugh [8]. Apparent panel-to-panel variations exist in the baseline data, which is evident in the scatter shown in Figures 10 and 11. All temperature and stress level effects are taken into account in calculating the Larson-Miller Parameter for each specimen. Specimens that failed during the loading process are not incorporated into the analysis.

Table 8. Baseline Sustained Load Test Results			
ID #	**Stress (MPa)**	**Temperature (°C)**	**Time-to-failure (hrs)**
95-713	1170	427	13.73
95-714	1030	427	Interrupted
95-A05	1030	538	Loading
95-A06	1030	427	Interrupted
95-A13	1170	427	93.18
95-A14	1170	538	0.96
95-A48	1075	427	Loading
95-A49	1170	427	0.21
95-A50	1015	427	Loading
95-A51	827	538	Interrupted
95-A52	1195	427	Loading
95-A53	827	427	112.42

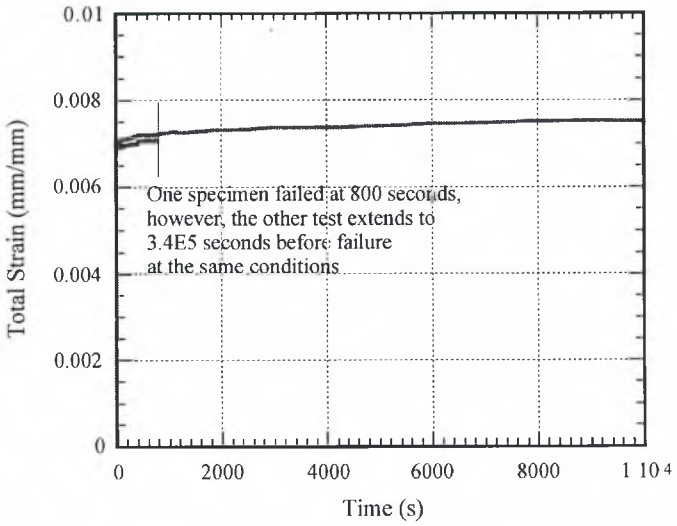

Figure 10. Strain vs. time plot for 96-A49 (short life) and 96-A13 (long life) at the same test conditions.

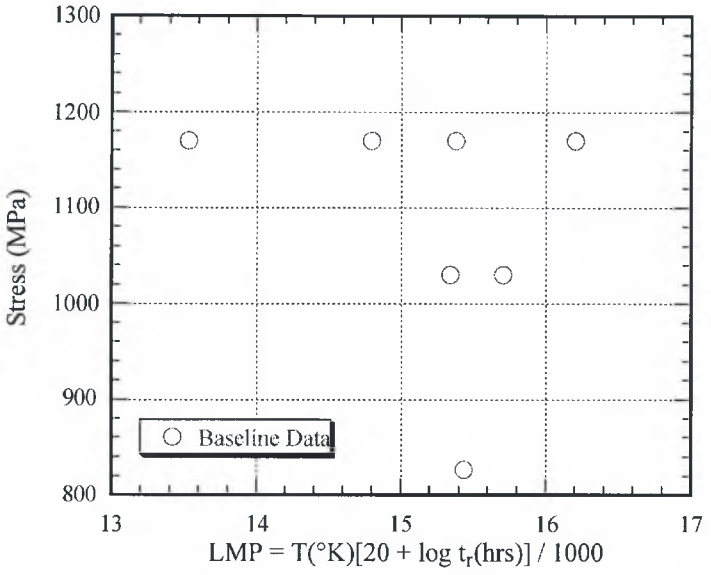

Figure 11. Baseline sustained load test results based on the Larson-Miller Parameter.

4.2.2 NDE Specimens

Five sustained load tests at stresses from 1000 to 1150 MPa were run to specimen failure. A sixth test was performed to compare optically recorded fiber breaks with AE events by interrupting the test before failure and dissolving the matrix. The mechanical data from the sustained load tests are plotted in Figure 12.

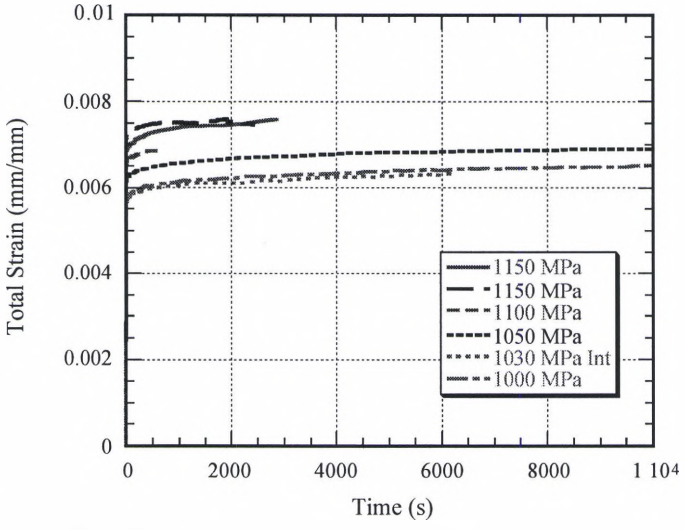

Figure 12. Strain vs. time plot for all NDE samples. The 1030 MPa stress test was interrupted for fiber fracture analysis.

The Larson-Miller Parameter (LMP) was calculated for all sustained load specimens. The test stress level was then plotted vs. the LMP to compare the data with baseline data in Figure 13. The baseline data had a wide scatterband due to panel-to-panel variation, while the data acquired from the panel 9 demonstrated less scatter. The reason for the scatter in the data could not be determined from the mechanical test results. Mechanical test results, however, demonstrated that panel 9 did not exhibit as high a creep resistance as the baseline panels. Other techniques such as NDE *in situ* longitudinal bulk wave and acoustic emission techniques in conjunction with metallography and ultrasonic immersion C-scans were necessary to characterize the material response to mechanical testing.

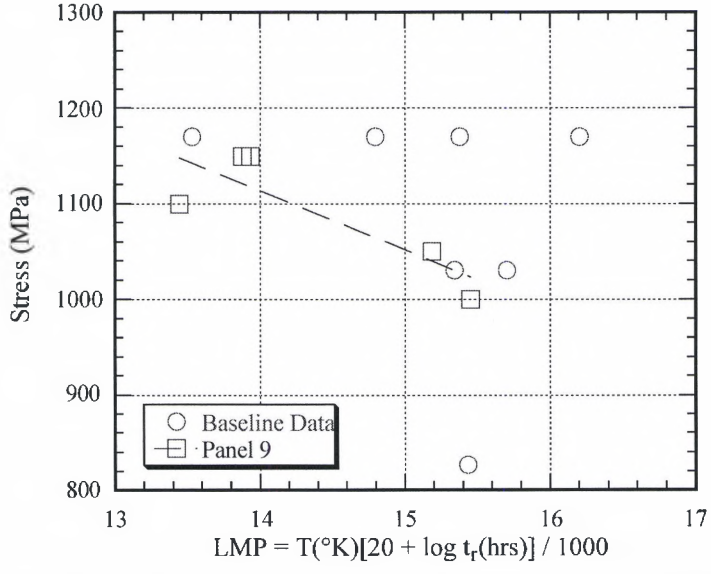

Figure 13. Comparison of baseline data to NDE specimen data using the Larson-Miller Parameter.

4.3 IP TMF Tests

Once the specimen is aligned and gripped in the test machine, four thermocouples are spot welded to the specimen; two at the center of the gage section, one on top and bottom, and two more, each approximately 12 mm to each side of the top center thermocouple. The thermocouples are again used for monitoring and controlling the temperature of the test. The extensometer is then placed in contact with the specimen as described in the sustained load test procedure. Before the test begins, specimen dimensions are measured, and the information is input into the computer. The specimen is then loaded within the elastic region to obtain a room temperature elastic modulus values in the same manner as for the sustained load test using extensometer data acquired during the loading.

The heating portion of the cycle is accomplished through computer control of the quartz lamps. The cooling portion of the test cycle is controlled with the uniform flow of dry gaseous nitrogen regulated by a electropneumatic pressure control valve. The supply line of nitrogen branches into two small diameter tubes that contain small circular openings along the cylinder wall for uniform flow over the surface of the specimen gage section as shown in Figure 14. The pressurized nitrogen of commercial purity is kept at a temperature of -70°C in a chiller bath unit. Several high pressure gaseous nitrogen tanks are necessary to provide a continuous supply of nitrogen over the test period.

The sawtooth waveform control ramps the load and temperature to the maximum level in the first 50 seconds of the cycle, and then ramps the load and temperature to the minimum level in the last 50 seconds of the cycle. The data acquisition (DAC) rate is set

to collect the load-displacement traces at set intervals throughout the test. The interval depends on the length of the test. For short tests, the interval is approximately every 10th cycle, while for longer tests, the interval is approximately every 100th cycle. The final 10 cycles before failure also are stored by the MATE program. The load-displacement traces are used to calculate the elastic modulus during the test. The mechanical strain data is compared with ultrasonic modulus values calculated with the bar wave equation.

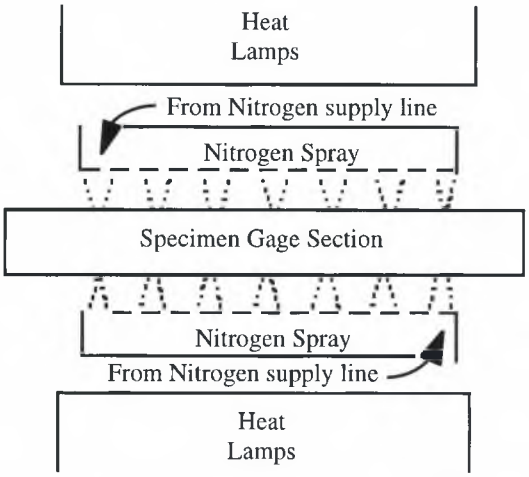

Figure 14. IP TMF nitrogen cooling aperture used in the cooling portion of the thermomechanical cycle.

4.3.1 Baseline Specimens

All baseline IP TMF tests were under the supervision of Rosenberger [9]. The test results are listed in Table 9 and are displayed in Figure 15. The specimens exhibited slightly shorter fatigue life than anticipated, and therefore, the maximum stress chosen for mechanical testing was lowered by 50 MPa to produce longer specimen life.

Table 9. Baseline IP TMF Results		
Specimen ID #	**Stress (MPa)**	**Cycles to Failure**
95A23	1200	3
95A24	1200	5
95A27	1150	6567
95A25	1050	14240

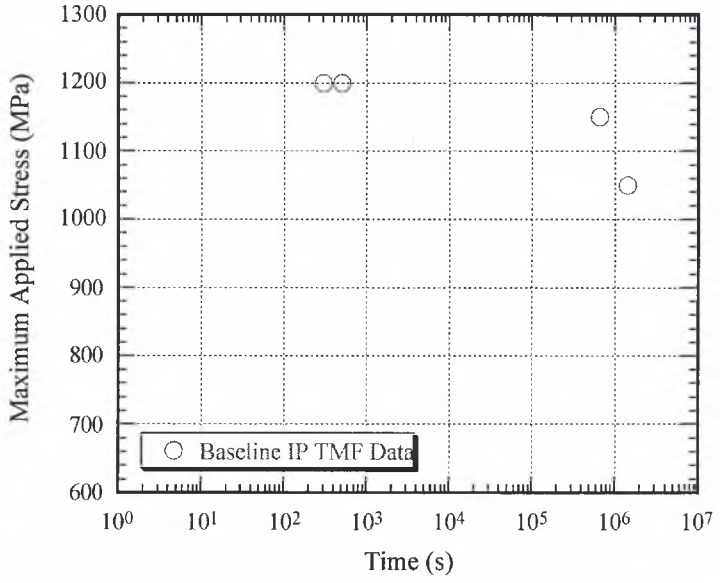

Figure 15. Baseline IP TMF time-to-failure data for the maximum applied stress.

4.3.2 NDE Specimens

Five IP TMF tests were performed at maximum stress levels from 1000 MPa to 1150 MPa. The results of the IP TMF tests were compared with the baseline data and are plotted in Figure 16. The reason for such large data scatter is that all specimens tested at 1100 MPa failed earlier than the specimen tested at 1150 MPa as was seen with the sustained load test results. Fiber volume fraction may be the cause for differences in the results between panels, however, no fiber volume fractions were available for comparison. All other tests exhibited longer life at lower stresses as is shown in Table 4.

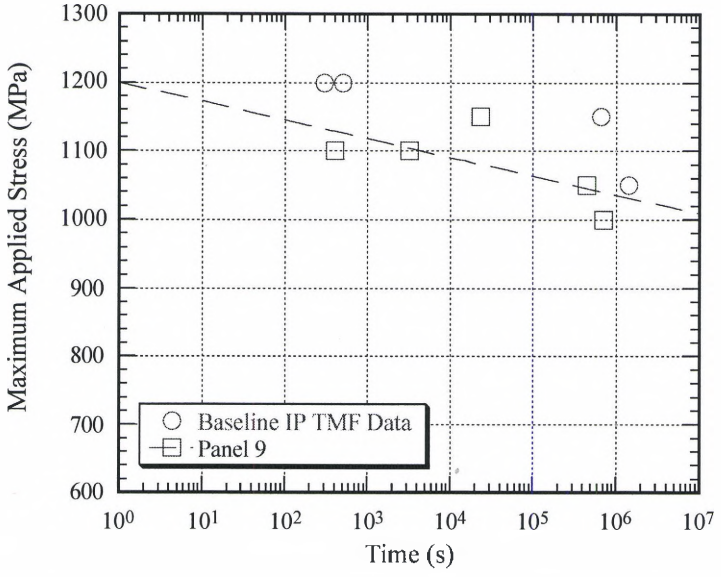

Figure 16. Semi-log plot of IP TMF results for baseline data and NDE study.

Further analysis was performed on the minimum and maximum strain levels acquired at selected cycles during the tests. No change in minimum and maximum strain levels throughout the test indicated that there was little change in the stiffness of the material, and that stiffness measurements were not a good indictor of damage accumulation in the material. All mechanical data were then compared with NDE ultrasonic amplitude and modulus data and AE event data in the following chapter.

CHAPTER V.

COMPOSITE *IN SITU* NDE PROCEDURE AND RESULTS

Chapter 5 will discuss the procedure for acquiring the nondestructive data and the results obtained from the data. Data analysis was performed, and the data were compared to results from mechanical data in the previous chapter. Correlations between the two loading conditions were ascertained using the *in situ* NDE data in conjunction with the mechanical data.

5.1 *In Situ* Testing Procedure

5.1.1 Ultrasonic Longitudinal Bulk Wave

The ultrasonic contact technique is an *in situ* pitch-catch method utilizing longitudinal wave propagation. A 200 kHz compressional wave ultrasonic transducer was placed into the cavity of the grip and put in contact with the end of the specimen. A metal backing with spring loading was placed behind the transducer to maintain solid contact and contact pressure between the specimen and transducer. An identical procedure was used at the other grip. Figure 17 shows how the transducers were placed in contact with the specimen.

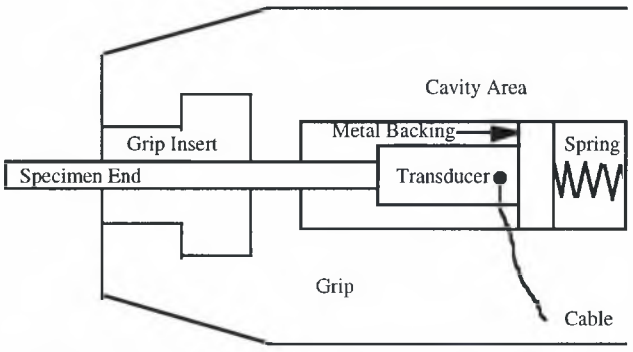

Figure 17. Transducer placement in grip area.

Once the transducers were in place, the signal response was viewed on an oscilloscope. The transducers were shifted around in the cavity to maximize signal amplitude. Once the transducers were in proper position within the grip cavities, the ultrasonic signal was acquired by the DASP500 A/D board.

There was a large amount of ultrasonic signal loss presumably into the grips detected by the AE sensors as noise events when the AE sensors were placed on the grips. As grip pressure was increased, the received ultrasonic signal altered frequency content from 200 kHz to 1 MHz (Figure 18). The apparent change in frequency due to grip pressure did not, however, affect TOF information, the signal at high grip pressure arrived at the same time as the signal at low grip pressure. The characteristic low 200 kHz frequencies were still present yet masked by the high frequency signal. It was assumed that the change in frequency was due to the signal transmission and reflection at the specimen/grip insert interface. The signal was assumed to be the original longitudinal wave modified by grip stress and reflections at the specimen and grip insert interface. If a different grip insert material was used, then the signal should maintain only the low frequency components without high frequency reflections.

The velocity of sound along the fiber axis of the composite was measured before mechanical testing to determine if there was any variation between specimens, which is displayed in Table 10. The density of the composite along with the ultrasonic velocity was used to calculate a room temperature ultrasonic modulus for each specimen. All density, velocity, and modulus values were within acceptable values. The values calculated for the two tensile specimens 96-771 and 96-F31 were lower than other specimens. The lower tensile strength was due to the undulated fibers in the composite that would allow the composite to strain more in the loading axis direction yielding a lower modulus value. The density values compared well with the theoretical density calculations using the rule of mixtures, and ultrasonic modulus calculations compared well with modulus values obtained from mechanical test data.

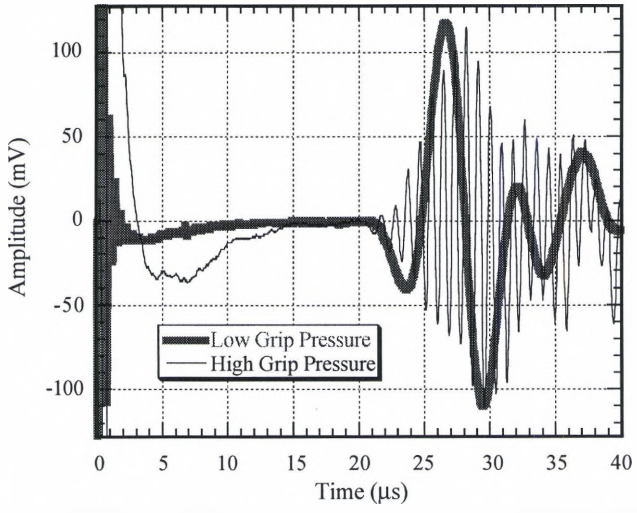

Figure 18. Increase in signal frequency due to increased grip pressure.

Table 10. Specimen Material Properties Calculations					
Specimen ID	Density (g/cc)	Theoretical Density (g/cc)	Velocity (mm/μs)	UT Modulus (GPa)	Mech. Modulus (GPa)
96-771	3.95	3.86	7.07	197	181
96-F31	3.95	3.86	7.07	197	172
96-772	3.93	3.86	7.45	218	217
96-773	3.95	3.86	7.42	217	235
96-774	3.94	3.86	7.40	216	201
96-775	3.95	3.86	7.39	216	211
96-776	3.95	3.86	7.43	218	211
96-777	3.95	3.86	7.36	214	202
96-778	3.96	3.86	7.34	213	218
96-779	3.97	3.86	7.38	216	201
96-780	3.97	3.86	7.44	220	209
96-781	3.96	3.86	7.24	208	213
96-782	3.97	3.86	7.42	219	209
* 96-F31 Mechanical Modulus at 427°C					

5.1.2 Acoustic Emission

The *in situ* acoustic emission analysis was performed on all specimens. The events from each test were analyzed and characterized as either noise, matrix type damage such as cracking and plasticity, or fiber fracture. The characterization was based on location, amplitude, and frequency of the event.

Several improvements were made in the acquisition of acoustic emission waveforms from composites because the system had several advanced signal analysis features. The new features included noise discrimination, source location, FFT analysis, and material characterization. With proper signal acquisition, an AE event could be classified as either noise, fiber fracture, or other material event.

First, sensors were relocated onto the specimen instead of being located on the grips. Sensor relocation allowed for better waveform acquisition and analysis. Four sensors were used on the specimen instead of two on the grip. Two of the sensors had the preamplifiers set on low attenuation (+20 dB gain) to acquire low amplitude events such as matrix events, while two other sensors had the preamplifiers set on high attenuation (+0 dB gain) to acquire high amplitude events such as fiber fracture and final failure.

Second, the data collection time window was reduced to 80 microseconds to eliminate the collection of reflections propagating in the material. The part of the waveform that characterized the waveform as either from matrix event or fiber fracture occurred in the first extensional and flexural wave modes. Additional signal information should not be extracted because that part of the signal manifests due to reflection and material damping characteristics occurring after the first modes. Once the new signal acquisition technique was implemented, source location and frequency analysis could be performed with higher accuracy because more data points could be acquired over a shorter period of time. The new signal acquisition technique provided more clarity in signal composition stored by the AE system.

Finally, the method of signal analysis was modified from a simple amplitude and duration analysis to modal acoustic emission analysis. Modal acoustic emission incorporates all the old measurement methods such as amplitude determination, with new information such as frequency content about the waveform. Information also was acquired about the extensional and flexural wave propagation modes. The first order

extensional and flexural modes are the most important modes because they are pure in form unlike higher modes, which are mixed with reflections. The analysis of the first order modes of propagation allowed for more accurate determination of event source type and location.

The sensor array was defined as the area between the sensors where acoustic events could be located. Noise was determined to be any event occurring outside the sensor array, or any event waveform not demonstrating a high frequency extensional (in-plane) component followed by a lower frequency flexural (out-of-plane) component. Fiber and matrix cracks developing perpendicular to the loading axis produce extensional and flexural waves that propagate through the material. The extensional wave is of a higher frequency and travels faster than a lower frequency flexural wave. Therefore the high to low pattern was searched for in the signal waveform to determine if the signal was a crack or noise.

Noise also was determined by extremely low frequencies below 200 kHz due to mechanical noise, or by extremely high frequencies above 4 MHz due to electronic noise. The ultrasonic signal from the 200 kHz transducers, if received by the AE sensors, was also characterized as noise and eliminated from the analysis. All other events were assumed to be generated in the specimen due to damage accumulation. Noise was eliminated by the operator after the mechanical test using signal analysis. Analysis of the remaining events was performed to distinguish between fiber fracture and other composite events.

Non-fiber fracture events were characterized by a large amplitude signal no greater than ±100 mV with a frequency content centered at approximately 350 kHz that did not saturate the acquisition system, because matrix related events do not generate high energy and amplitude signals [22]. There was also a combination of midrange (200-500 kHz) frequencies in the waveforms due to the dispersion of the wave while traveling through the matrix. The matrix was determined to exhibit damping of the AE signals which reduced the acquired frequency range in the signals. The waveform exhibited a high frequency extensional wavefront followed by a lower frequency flexural wavefront. The AE signals were difficult to characterize due to the difficulty of differentiating the extensional wave and flexural wave modes due to dispersion. The events were located primarily near the fracture surface as expected, with few events occurring at various locations within the gage section. The locations of AE events indicated that though minor damage accumulation was occurring throughout the gage section, damage progression was concentrated in one area of fiber fracture and matrix cracking. An example of a possible matrix crack waveform is displayed in Figure 19.

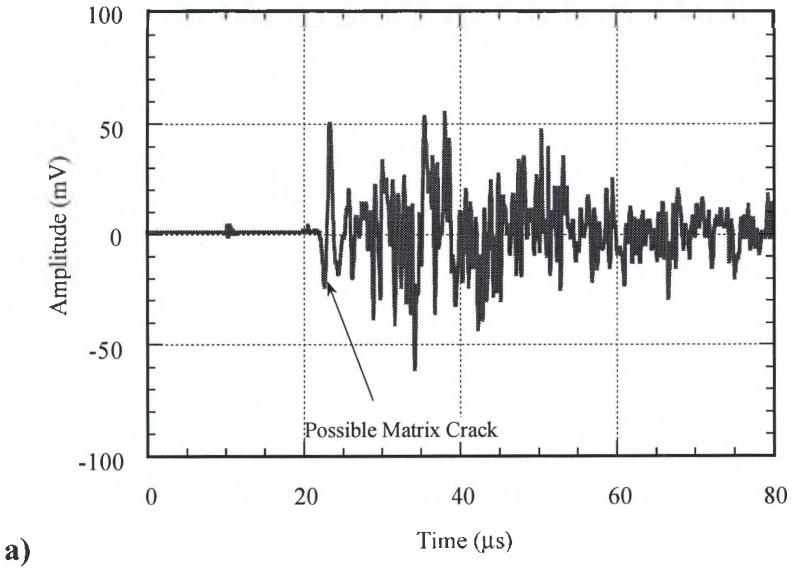

a)

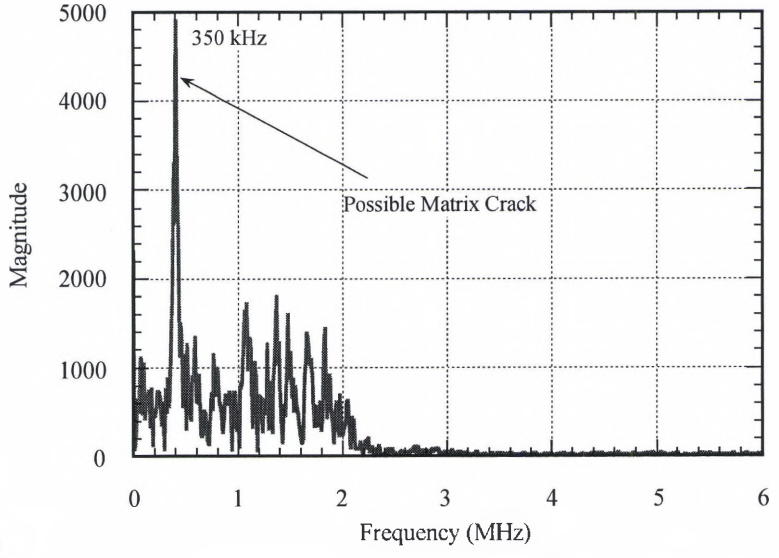

b)

Figure 19. Possible matrix crack waveform from specimen 96-778. a) time domain and b) frequency domain.

Fiber fracture events were determined to be the highest amplitude events observed in the test results shown in Figure 20. The high amplitude events often saturated the signal processor, and clipping of the signal was observed in the pre-amplifier stage of acquisition. Large amounts of attenuation had to be applied to the system to compensate for the saturation.

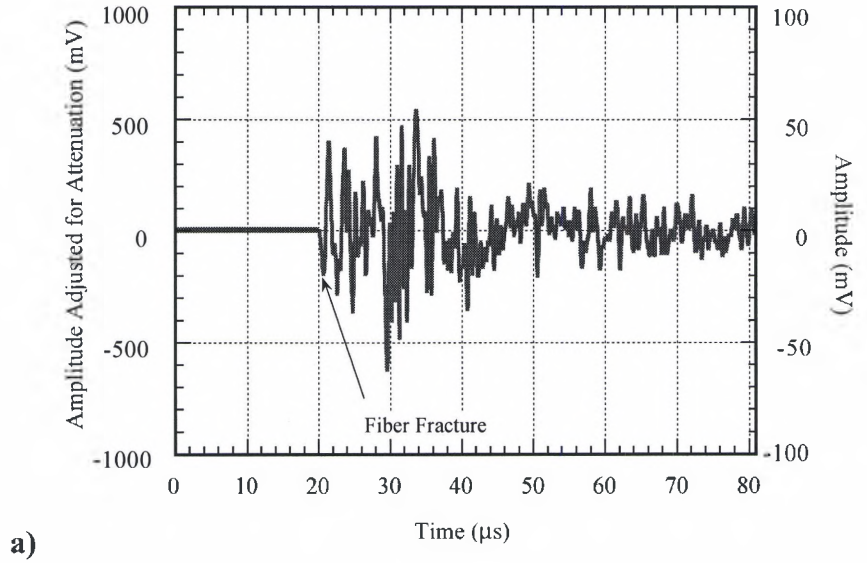

a)

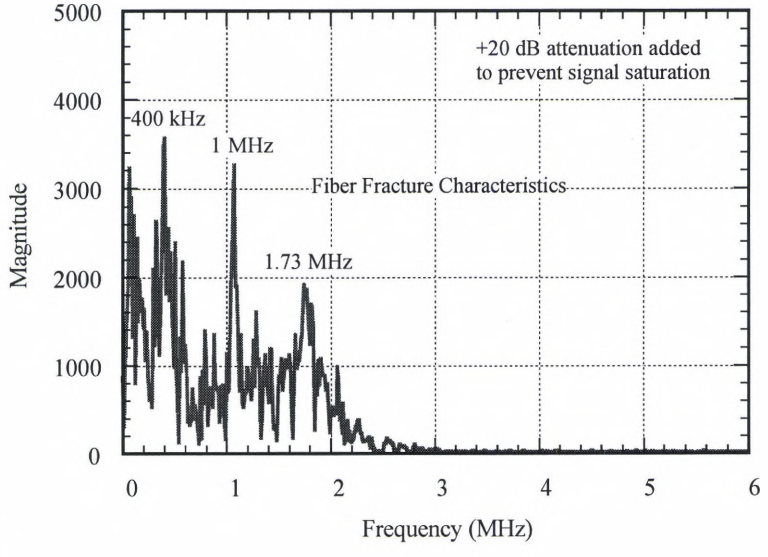

b)

Figure 20. Fiber fracture waveform from specimen 96-778. a) time domain and b) frequency domain.

Fiber fracture was determined to be a higher energy event and gain settings for the fiber sensors were set approximately 20 dB lower than matrix sensor gain settings. The fibers emitted peak voltages larger than 200 mV. Peaks at high frequencies at higher magnitude were predominate in fiber fracture events. Fiber fractures were characterized as high energy, long duration events exhibiting high frequency components, the most

prominent being a characteristic frequency of 400 kHz. The reason for such a dominant low frequency component was that the matrix was damping out higher frequencies as the signal traveled to the AE sensor and filtering in the AE system did not allow for the full energy from higher frequencies to be acquired. With alterations in filtering, higher frequency components should prove to be more dominant.

Fiber fracture frequencies are expected to be high due to the fiber diameter, brittle nature of the fiber, the high tensile strength, and lack of ductility. When compared with the dispersive nature of the matrix to sound propagation, lower tensile strength and increase in ductility at elevated temperature, it is expected that fiber fracture events should be very different in signal composition than matrix events, both in amplitude and frequency.

Not only was there a need for source characterization, but also source location. AE *in situ* location of fiber fractures and matrix events would allow an engineer to determine where a component would break before composite fracture. Location was achieved by determining the time of arrival difference between AE sensors. Distance between the AE sensors was known, as well as time travel difference determined from lead break calibrations performed before testing [52]. Therefore, the location of events inside the sensor array (between the sensors) could be determined.

Once the AE sensors were in place and settings were properly adjusted, lead breaks were performed on the surface of the specimen at the location of each sensor, and at the center of the specimen for gain, threshold, and location calibration purposes. The technique is documented by ASTM and Prosser and Gorman [50, 52, 53]. The signal

response from each sensor was analyzed. If the responses were consistent in amplitude and frequency content and the event location could be confirmed, then the AE system was ready to acquire acoustic events during the mechanical test.

Load was applied to the specimen, and during the life of the specimen, acoustic events were acquired by the system. A Fast Fourier Transform (FFT) was performed on the most recently acquired signal to determine frequency components of the waveform. A continuous updated plot of events vs. time and parametrics (load and strain voltages) vs. time also was available during the test. All other analysis had to be done post test. Post test analysis will be discussed in the results section of this chapter.

5.2 Results

5.2.1 Tensile Specimens

The 200 kHz ultrasonic transducers were not available to perform longitudinal bulk wave analysis at the time the room temperature tensile test was performed. Therefore, no data were acquired using ultrasonics. However, the AE system was available at the time of the tension test. AE data from the first RT test recorded 57 total events, 18 of which were high amplitude and frequency events characterized as fiber fractures. The repeat of the first tensile test recorded 163 total events, 20 events were high amplitude and frequency events characterized as fiber fracture. Most of the signals acquired during the test were eliminated as noise from outside the AE sensor array. The time and stress at which the AE events occurred is displayed in Figure 21. Stress and strain voltages and time were acquired with the acoustic event by the AE system, and is plotted in the following figures.

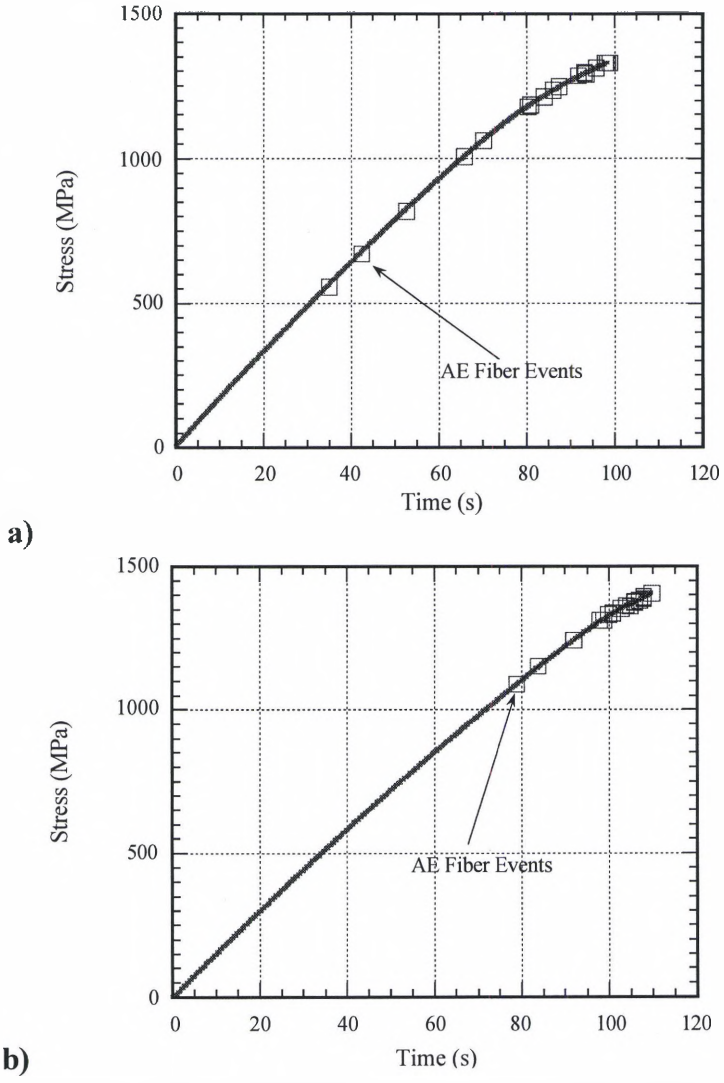

Figure 21. Acoustic emission fiber fracture events recorded during RT tension tests. a) UTS = 1329 MPa b) UTS = 1409 MPa.

The tensile test performed at 427°C (Figure 22) recorded 607 events, only 12 of which were determined to be fiber fracture events from the AE data. Over 500 of the events recorded during the high temperature tensile test were ultrasonic signals leaking into the grips from the bulk wave transducers, which were eliminated as noise. The lower amount of fiber fractures before failure was attributed to the slower strain rate and higher temperature test conditions. A reduction in strength is usually observed when tension

tests are performed at slower strain rates and higher temperatures, and fewer fiber fractures would have to occur before failure of the composite specimen. Note that the parametrics measured by the AE system did not exactly correspond with data from the mechanical test due to software program errors later fixed by the company.

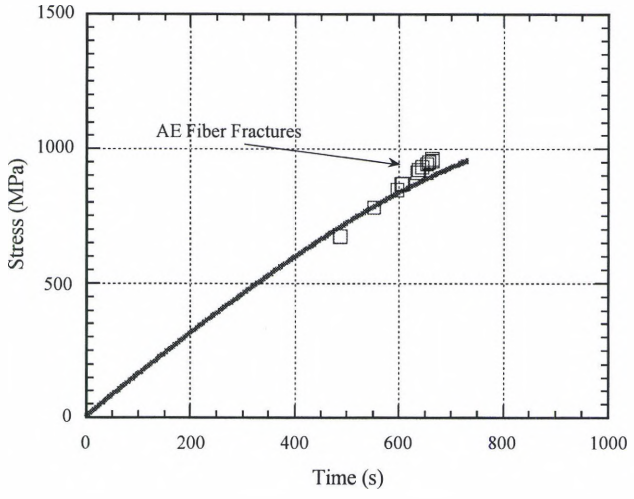

Figure 22. Elevated temperature (427°C) tension test results with acoustic emission fiber fracture data. UTS = 960 MPa.

5.2.2 Sustained Load Specimens

Ultrasonic and acoustic emission data were acquired during all sustained load tests. The ultrasonic signals were analyzed based on arrival time of the signal for modulus calculations, and peak-to-peak amplitude. The ultrasonic modulus values were normalized to the initial value acquired at maximum load and temperature in Figure 23.

As with all the sustained load tests in this study, Figure 23 shows the inability of the *in situ* longitudinal bulk wave method to detect changes in the material based upon ultrasonic modulus values. All ultrasonic data acquired from the mechanical tests can be found in a complete compilation in Appendix H. Due to the inability of the ultrasonic

modulus calculation method to detect damage accumulation, the signal amplitude was analyzed (Figure 24) to determine if damage accumulation could still be monitored using the longitudinal bulk wave technique at low frequency.

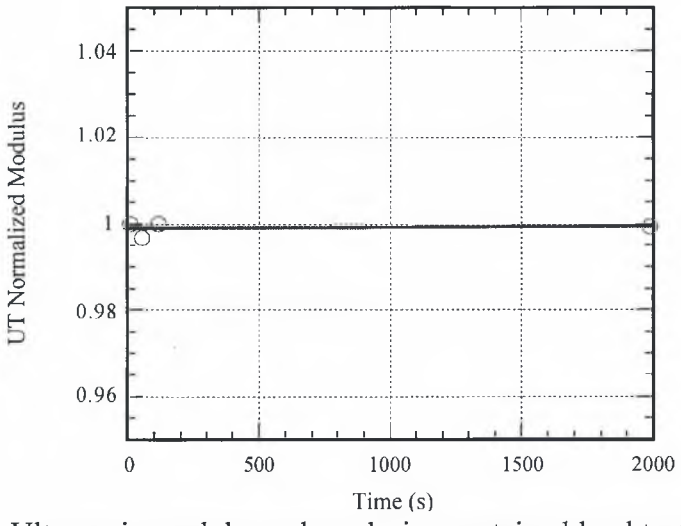

Figure 23. Ultrasonic modulus values during sustained load test at 1150 MPa.

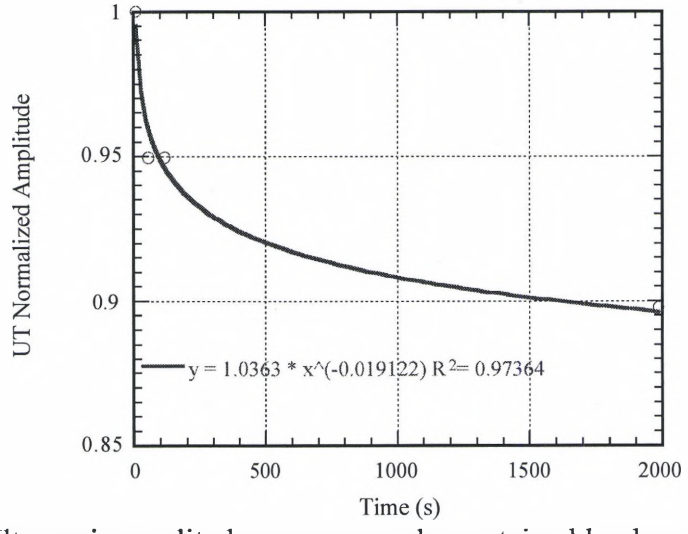

Figure 24. Ultrasonic amplitude response under sustained load conditions for 1150 MPa. Data were fit to power equation displayed in the figure.

The ultrasonic amplitude proved to be sensitive to changes occurring in the material associated with damage accumulation. All amplitude data for each test are compiled in Appendix H. All short life tests demonstrated small changes in amplitude

before failure, while longer life specimens demonstrated a larger decrease in ultrasonic amplitude as shown in Figure 25. Note that irregularities existed in time-to-failure for 1100 MPa test results.

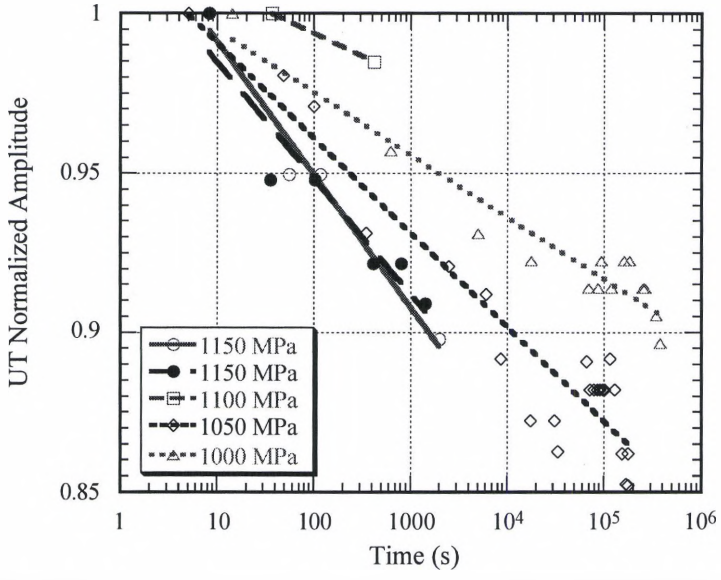

Figure 25. All ultrasonic amplitude data for sustained load tests.

AE signal waveform analysis showed that the number of fiber fracture events prior to failure is not dependent on the stress at which the test is performed as shown in Figure 26a, however the number of fiber fractures prior to composite failure ranged between two to thirty fiber fractures. When analyzing the number of fiber fractures based on time-to-failure (Figure 26b), there is an upward trend indicating that as the time of the test progresses, the number of fiber fractures detected by the AE system increases. Because the AE sensors were placed initially on the grips instead of on the specimen surface as done later, no accurate location and signal characterization could be performed for those specimens. All fiber fracture events collected from the test frame grips were determined from saturation of the AE system. It should be noted that the weak fibers in

the composite may have affected the amplitude and frequency characteristics of the fiber fractures and may not have met the criterion for fiber fracture, yielding an inaccurate value for fiber fractures prior to failure. Figure 26c shows the damage accumulation on the fracture surface of each failed specimen as a function of the applied stress. Damage accumulation transitioned from internal crack growth to surface connected as the applied stress was decreased.

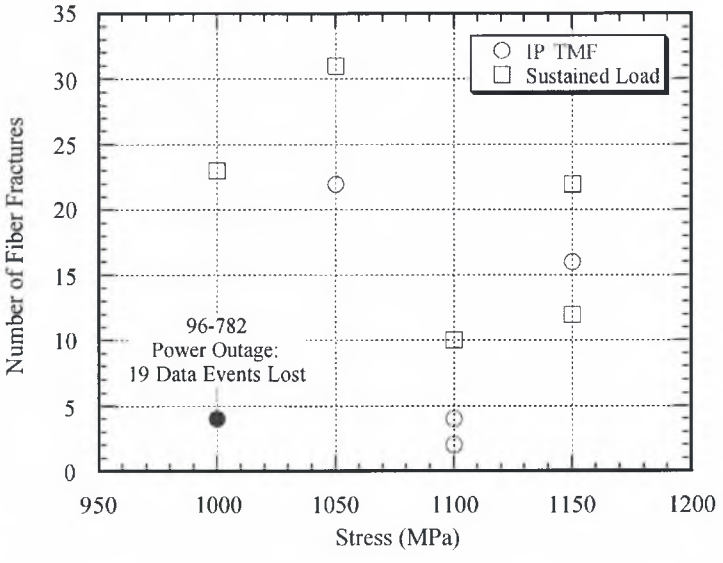

a)

Figure 26. Fiber fractures determined by AE analysis as a function of a) stress level and b) time-to-failure in comparison to c) matrix crack growth size on the fracture surfaces.

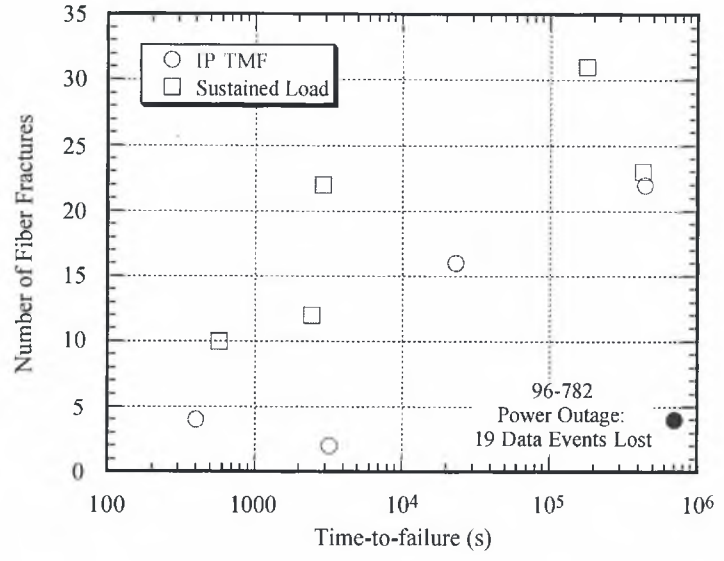

b)

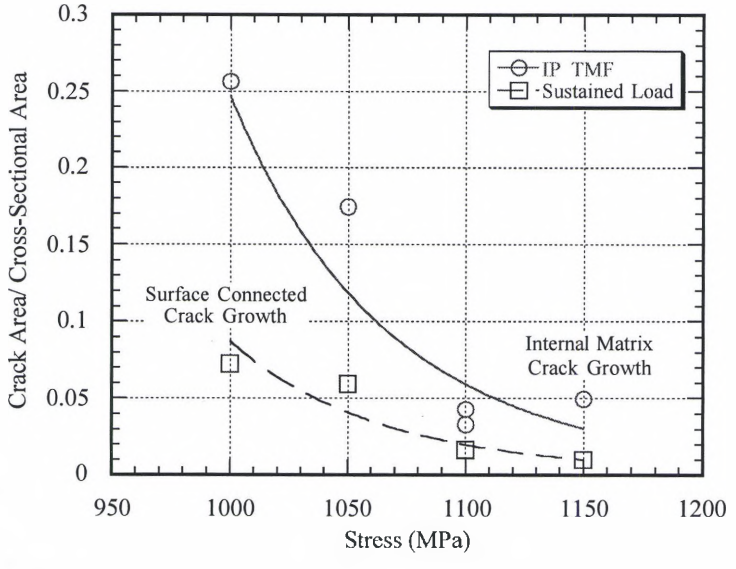

c)

AE data from specimen 96-778, which was tested with the sensors on the specimen, corresponds well with measurement of the fracture surface location. The fracture surface plane was not perpendicular to the loading axis and therefore length was difficult to measure, however, the approximate length was measured to be at the centerline of the specimen. AE data recorded large energy fiber fracture events just before failure at

1.3, 0.7 and 1.0 mm towards the actuator from the centerline of the specimen, which correlates well with the mechanical measurement as shown in Figure 27. AE, therefore, has the capability of detecting failure location.

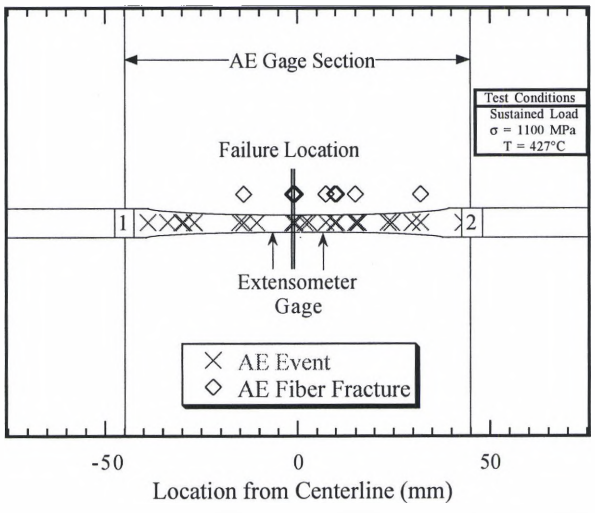

Figure 27. AE events corresponding to failure location of specimen 96-778.

Figure 28 (a-e) shows the sequential order in which the events occurred. The total number of events is broken down into four equal segments of time during the total test period of 600 seconds. AE events were initially scattered along the AE sensor array, however, the events bgan to concentrate near the fracture surface as time progressed. Of all the fiber fracture events, only one was outside the heated test section of the specimen.

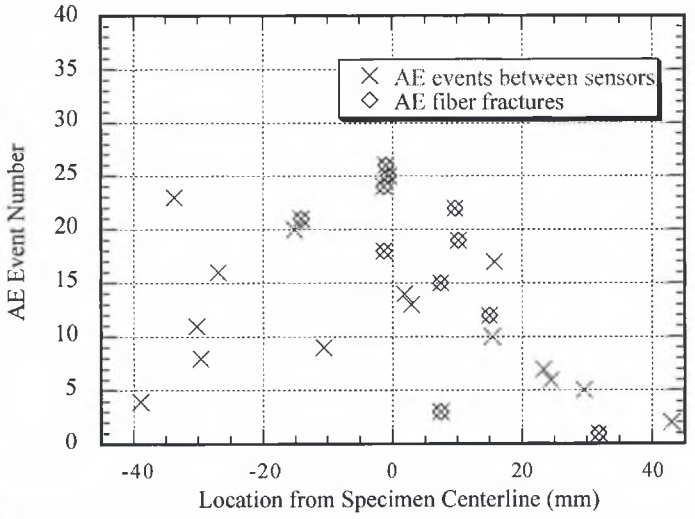

a)

Figure 28. AE event and location from specimen centerline for specimen 96-778, a) total events, b) events during 0-150s, c) events during 150-300s, d) events during 300-450s, and e) events during 450-600s (failure).

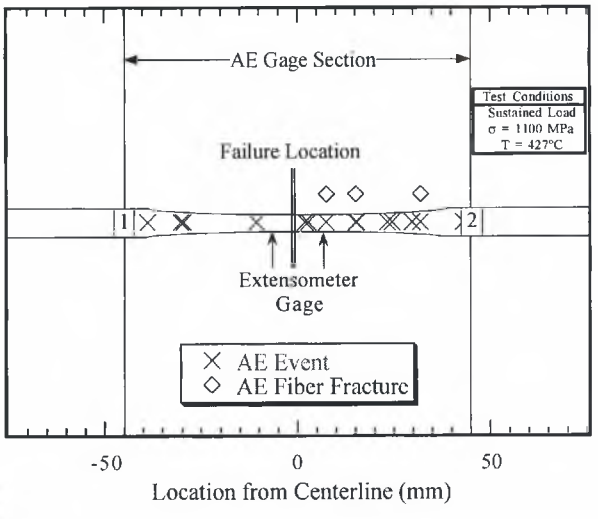

b)

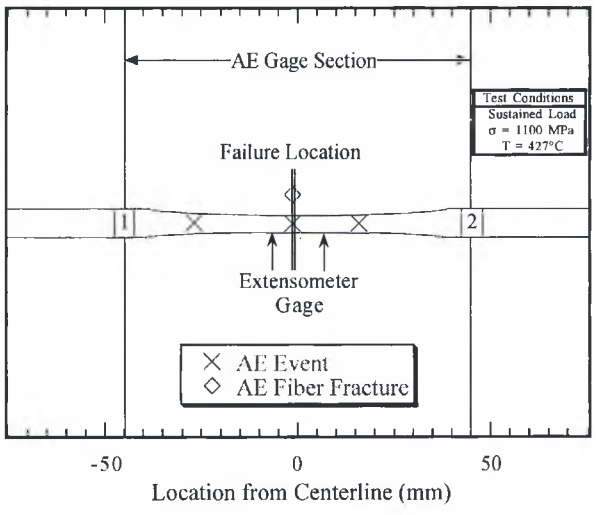
AE Gage Section
Test Conditions
Sustained Load
σ = 1100 MPa
T = 427°C
Failure Location
1
2
Extensometer
Gage
AE Event
AE Fiber Fracture
-50
0
50
Location from Centerline (mm)

c)

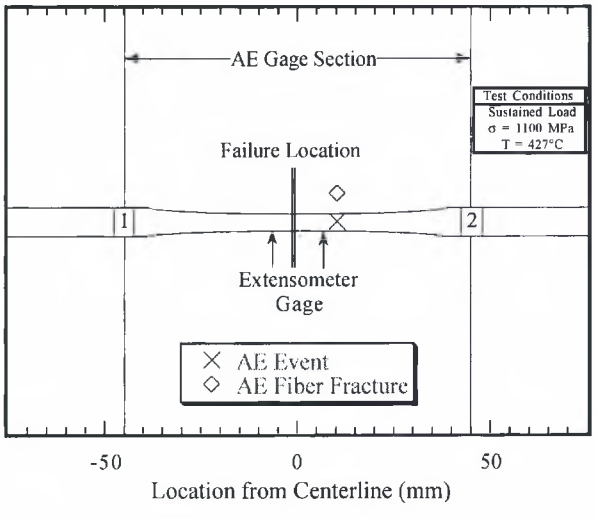
AE Gage Section
Test Conditions
Sustained Load
σ = 1100 MPa
T = 427°C
Failure Location
1
2
Extensometer
Gage
AE Event
AE Fiber Fracture
-50
0
50
Location from Centerline (mm)

d)

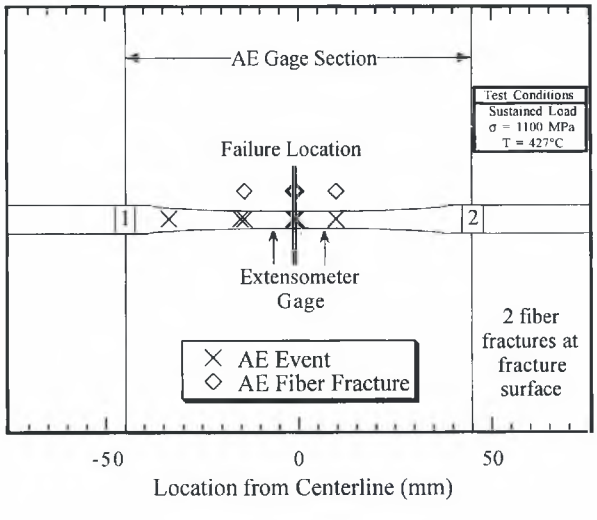
AE Gage Section
Test Conditions
Sustained Load
σ = 1100 MPa
T = 427°C
Failure Location
1
2
Extensometer
Gage
AE Event
AE Fiber Fracture
2 fiber
fractures at
fracture
surface
-50
0
50
Location from Centerline (mm)

e)

Optical verification of fiber fractures from the data of the interrupted sustained load specimen, 96-772, also demonstrated the ability for AE to locate and characterize fiber fracture events when the sensors were placed on the specimen surface. There were 107 total events during the test, 44 of which were eliminated as noise, and 11 which were characterized as fiber fracture signals from AE analysis. All of the 11 AE events were verified by optical inspection of broken fiber lengths. Optical inspection of broken fiber lengths from matrix dissolution has proven that the location capabilities of the AE system are accurate to approximately a millimeter as shown in Table 11. Figures 29 (a and b) and 30 (a and b) show the capabilities of the AE system to determine fiber fractures based on distance calculation, and amplitude.

Table 11. Fiber Fracture Locations Referenced to Specimen Centerline			
Event #	**AE Calculated Distance (mm)**	**Measured Distance (mm)**	**Optical Verification (mm)**
2	12	12.84	12.31
3	-9.2	-9.51	-11.32
4	-9.1	-9.51	-11.32
6	7.2	7.5	6.0
10	-0.5	0.1	-0.1
17	11.6	11.3	12.3
43	20.5	19.5	20.7
46	8.5	9.0	6.2
50	27.7	28.8	29.3
55	-5.9	-5.4	-5.0
64	18.2	19.2	17.6
66	27.7	27.3	25.5
71	-38.5	-39.0	Edge
75	17.9	17.4	17.4
76	35.6	36.7	36.7
82	-3.7	-4.4	-5.0
83	31.2	30.9	32.1
84	31.3	30.9	31.4
86	-33.8	-33.4	Edge
94	-3.4	-3.4	-2.4
(-): Actuator end (+): Load Cell end Events 71 and 86 were near the tab area			

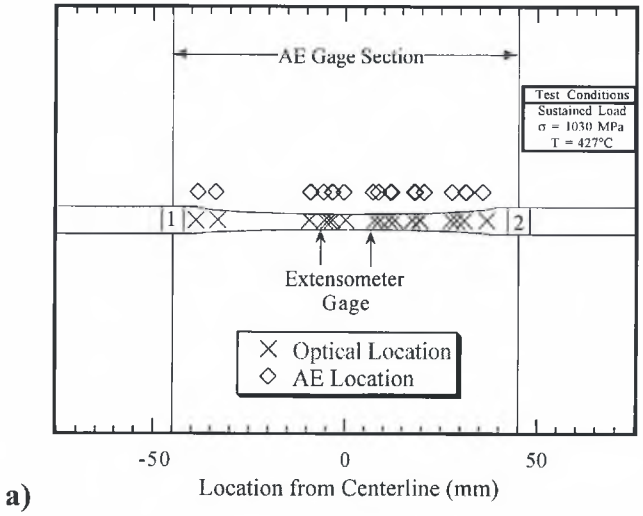

a)

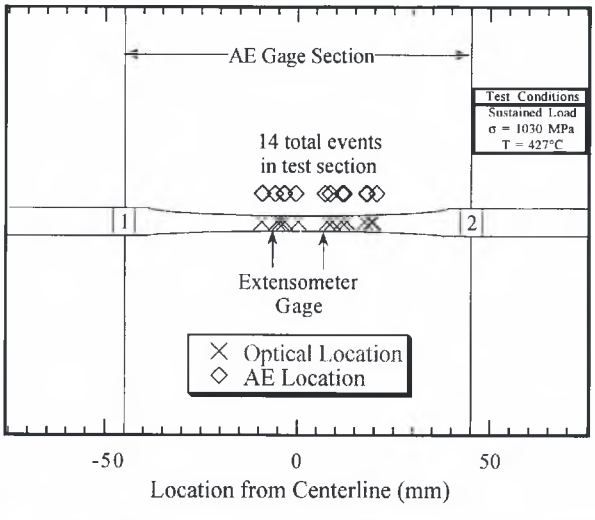

b)

Figure 29. Comparison of location of AE events based on location to optical measurements a) in total AE gage section, and b) in heated test section.

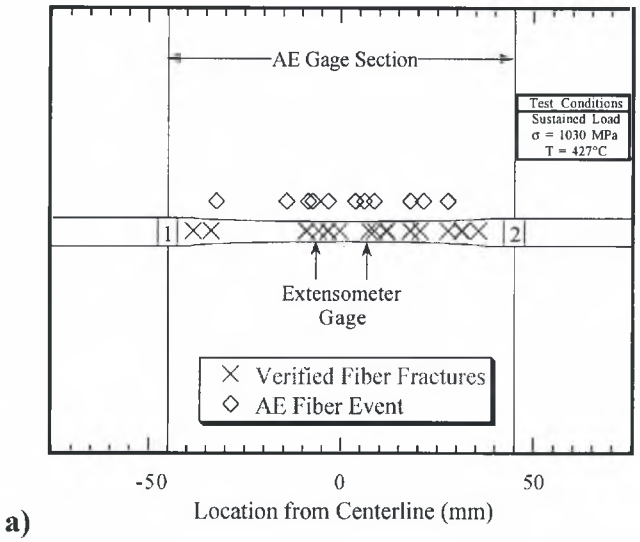

a)

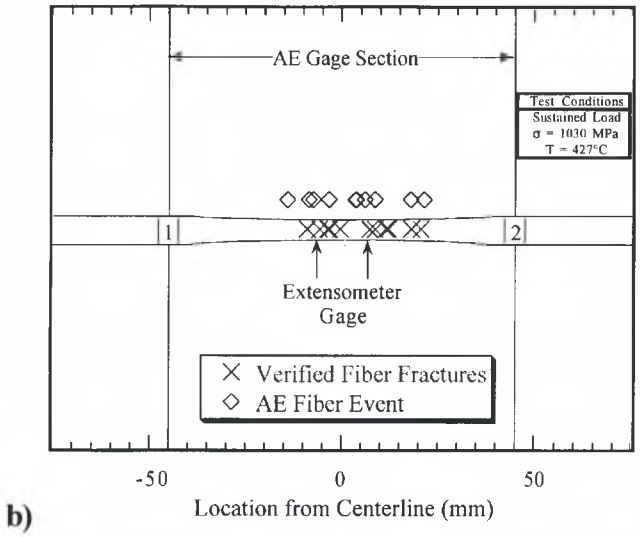

b)

Figure 30. Comparison of location of AE fiber fracture events based on amplitude to verified optical measurements a) in total AE gage section, and b) in heated test section.

The acoustic emission data was then compared to strain accumulation data as shown in Figure 31. Fiber fractures were determined to occur at random intervals during the test, with consistent fiber fractures at the end of each test. There were several fiber fractures that occurred during the loading of the specimen, and fibers continued to fracture until the total failure of the specimen. Individual test data are compiled in Appendix H.

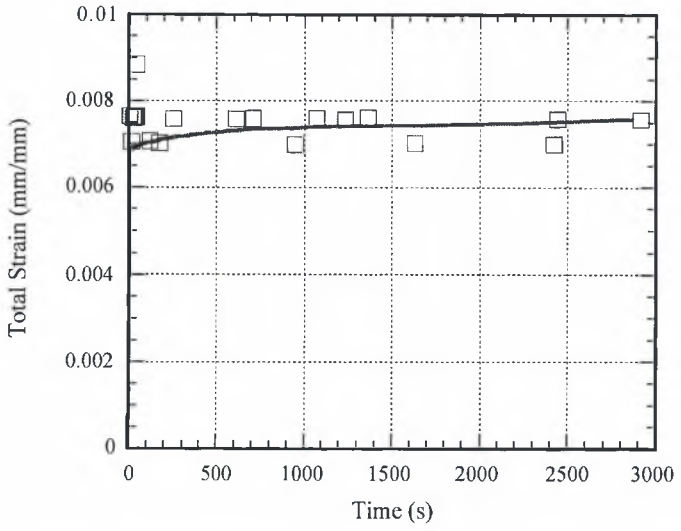

Figure 31. AE fiber fractures compared to mechanical sustained load data for 1150 MPa.

5.2.3 IP TMF Specimens

Ultrasonic and acoustic emission data were acquired during all IP TMF tests. The ultrasonic signals were analyzed based on arrival time of the signal for modulus calculations, and peak-to-peak amplitude. Figure 32 shows the ultrasonic modulus values acquired during one of the tests. The ultrasonic modulus values were normalized to the initial value acquired at maximum load and temperature. All subsequent acquisitions were at maximum load and temperature conditions.

As was the case with the sustained load tests, Figure 32 demonstrates the inability of the *in situ* longitudinal bulk wave method to detect changes in the material based on ultrasonic modulus values. All ultrasonic data from other IP TMF tests can be found in a complete compilation in Appendix H. Due to the inability of the ultrasonic modulus method to detect damage accumulation, the signal amplitude was analyzed to determine if damage accumulation could still be monitored using the longitudinal bulk wave technique. The results are plotted in Figure 33.

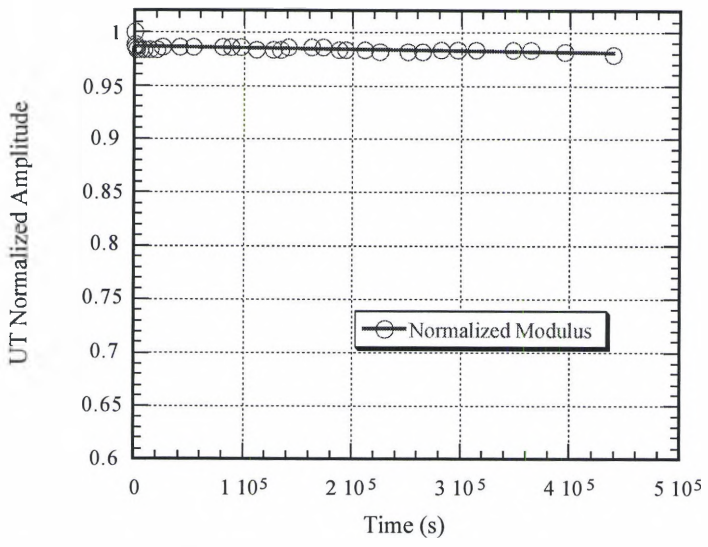

Figure 32. Ultrasonic modulus values acquired during IP TMF test for 1050 MPa.

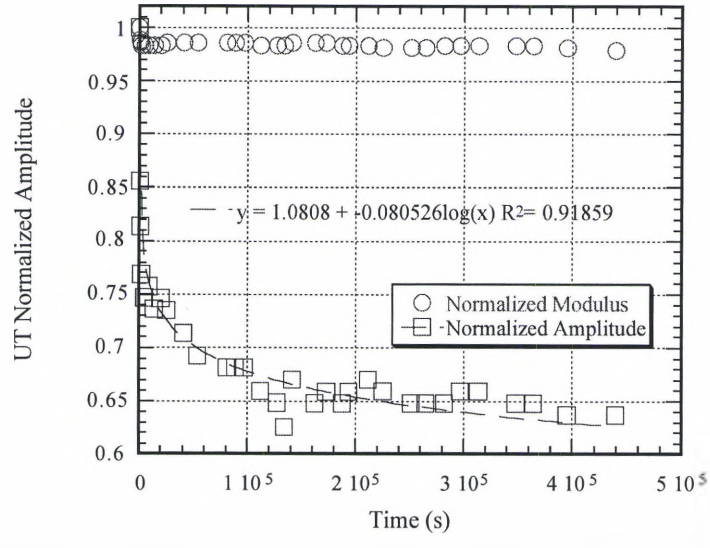

Figure 33. Ultrasonic amplitude response under IP TMF conditions for 1050 MPa test compared to ultrasonic modulus.

The ultrasonic amplitude proved to be sensitive to changes occurring in the material associated with damage accumulation. All amplitude data for each IP TMF test are compiled in Appendix H. The percentage decrease in amplitude was not directly

comparable to material life as was seen in the sustained load specimens, however, each test demonstrated a reduction in ultrasonic amplitude before failure. Typical tests showed a large initial decrease, and then a more gradual decrease until failure. Two of the tests showed an increase in amplitude over time, as can be seen in Appendix H. The data showing increase in amplitude were not used in the fit of the overall data set. All short life tests demonstrated small changes in amplitude before failure, while longer life specimens demonstrated a larger decrease in ultrasonic amplitude as shown in Figure 34.

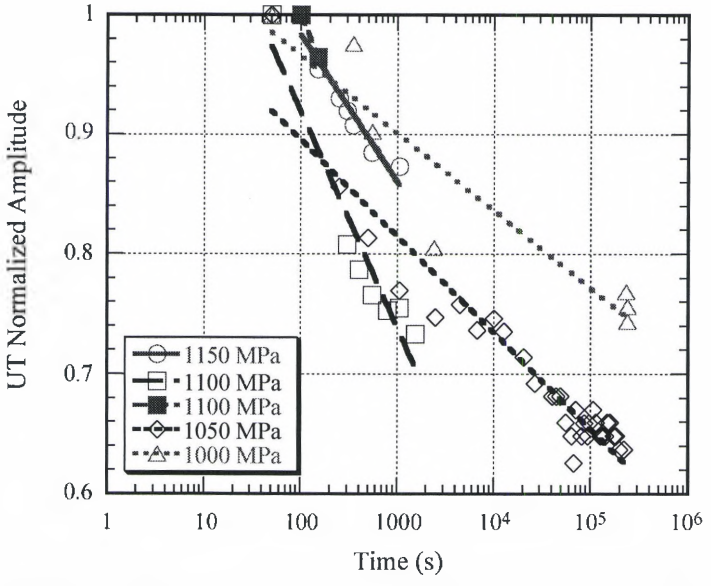

Figure 34. All IP TMF ultrasonic amplitude data. Slopes generally decreased with decreasing stress except for irregularities at 1100 MPa.

Note that irregularities in time-to-failure exist for 1100 MPa tests similar to the sustained load tests. The slope of the amplitude decrease appeared to be stress dependent. A smaller slope was observed in both sustained load and IP TMF at lower stress levels.

Comparisons were then performed between mechanical test data and *in situ* NDE data. The small changes in ultrasonic modulus corresponded well with the small amounts of stain accumulation seen in mechanical results. Neither the mechanical nor the UT modulus data demonstrated the ability to detect material changes prior to failure. Neither technique, therefore, appeared to be a good indicator of the onset of failure as seen in Figure 35.

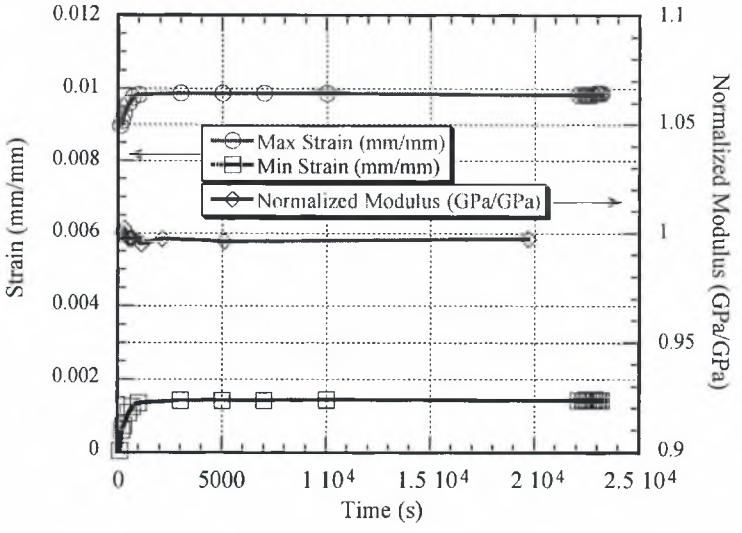

Figure 35. Comparison of mechanical strain sensitivity to UT modulus sensitivity for 1150 MPa IP TMF test.

The acoustic emission data was compared to mechanical strain accumulation data as shown in Figure 36. Fiber fractures occurred in groupings during the test. Several fractures occurred during the initial loading of the specimen, and fibers continued to fracture until the total failure of the specimen. All fiber fractures occurred during maximum load and temperature conditions for each test. Individual test data are compiled in Appendix H.

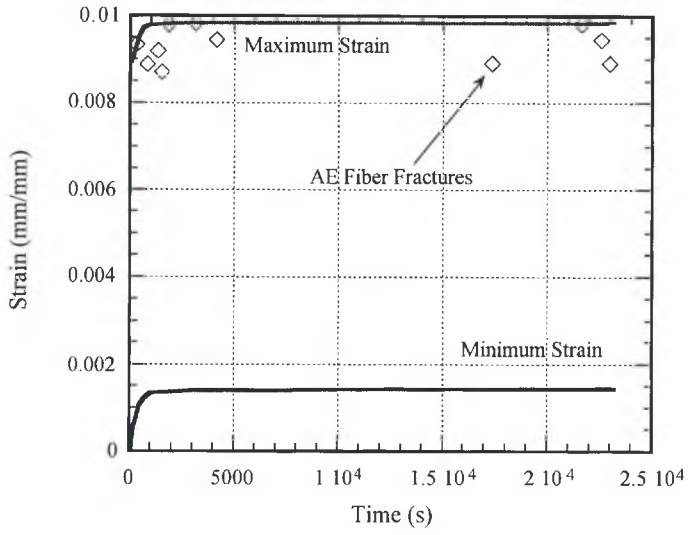

Figure 36. AE fiber fractures compared to mechanical data for 1150 MPa IP TMF test.

5.3 Post Mechanical Test NDE Support of *In Situ* NDE Data

Post mechanical test NDE techniques were used to verify the information obtained from *in situ* data. X-ray radiography was unable to locate internal cracking or individual fiber fractures characteristic of the failure of the SCS-6/Ti-6Al-4V composite material. Ultrasonic immersion techniques were also unable to locate any damage in specimens caused by mechanical test conditions. One backscatter shear wave C-scan, however did show the possibility of cracking in the material, but the detection of matrix crack growth could not be confirmed because the specimen was designated for matrix dissolution and fiber testing, not sectioning and SEM analysis. Figure 37 shows the high amplitude (blue and white) areas where cracking may have been occurring within the material. The high amplitude areas appear in the center and on the edges of the specimen. Figure 38 shows the fracture surface of another sustained load test at 1000 MPa with internal cracks which propagate to the surface, and helps support ultrasonic backscatter

shear wave C-scans images. Ultrasonic immersion backscatter shear wave C-scans may be able to detect cracks in the material before failure. However, the data are inconclusive due to lack of supportive evidence. Further C-scans and metallographic support will be necessary for proof that internal cracks are detected.

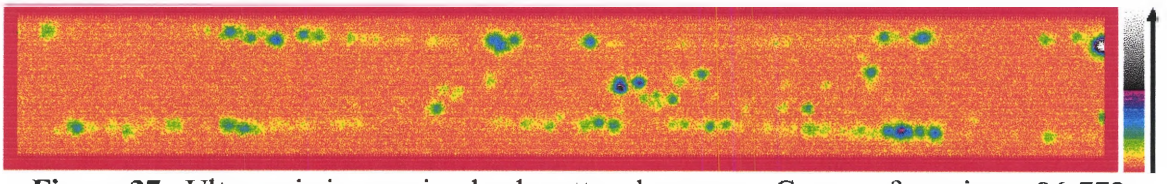

Figure 37. Ultrasonic immersion backscatter shear wave C-scan of specimen 96-772. Test interrupted after 1.73 hrs based on AE fiber information. Internal cracking is believed to be shown in the areas of higher amplitude.

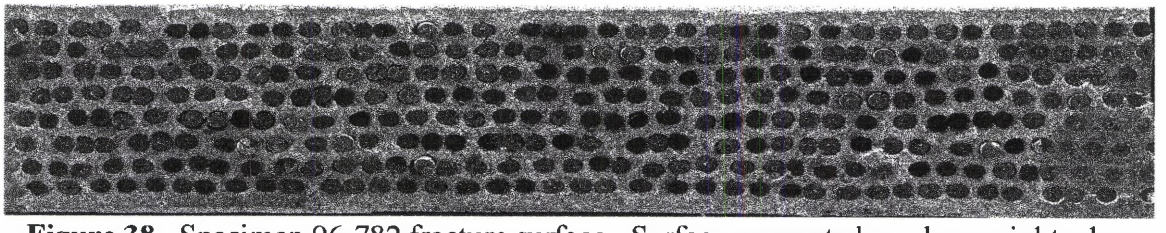

Figure 38. Specimen 96-782 fracture surface. Surface connected cracks on right edge.

A tensile load was applied to specimen 96-772 to open any cracks that may have closed due to compressive stresses within the material. A stress of approximately 500 MPa was applied to ensure no compressive stresses existed within the composite and that most of the internal cracks would be open to some degree without propagating them further and causing more damage to the specimen. Two scans were performed under the load conditions, the results of which are shown below. The first scan of the gage section of specimen 96-772 was performed at a resolution of 100 microns. A higher resolution of 25 microns was used to inspect anomalies located in the initial scan. The two small central areas correspond with those seen in Figure 37. Figure 39 shows the results of

loading the specimen while scanning. The overall scanning area for Figure 39 is smaller due to the increased resolution. Figure 39c. is of the highest resolution and therefore encompasses the smallest scanning area. The large high amplitude region on the right end corresponds with several fiber fractures near the actuator end of the specimen determined by acoustic emission location results.

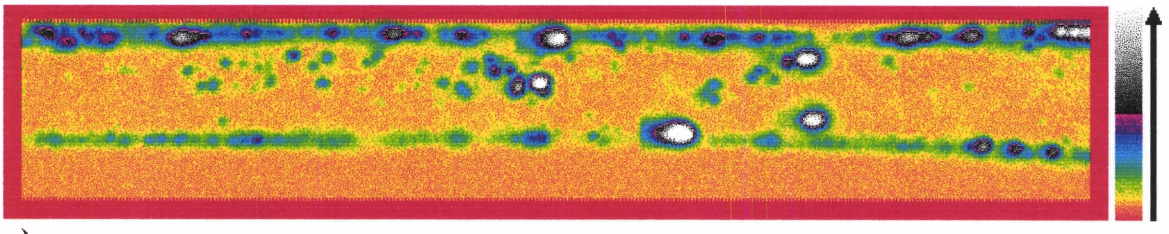

a)

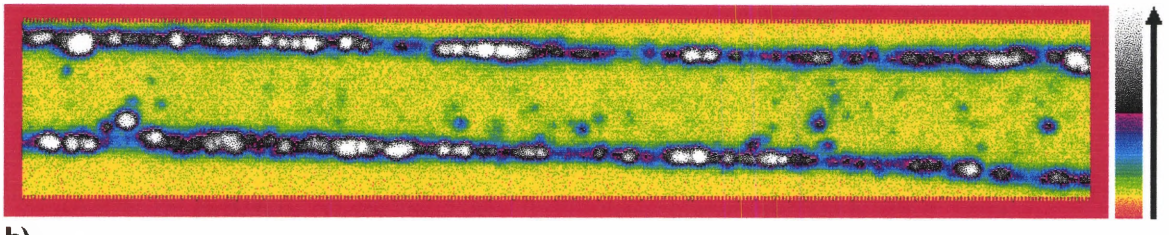

b)

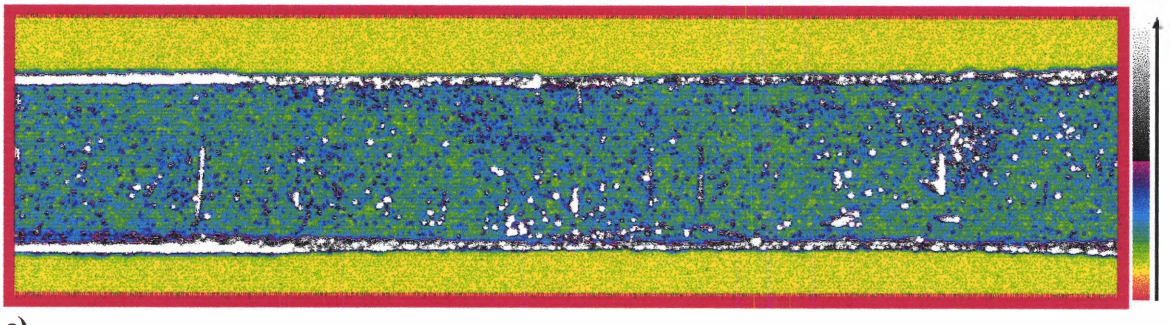

c)

Figure 39. Ultrasonic immersion backscatter shear wave C-scans performed under tensile load. a) frontside of specimen in Figure 37 showing thermocouple weld markings in center of specimen. b) backside of same specimen area. c) backside of specimen at higher resolution: cracking is possible at the wide vertical lines at each end.

Ultrasonic backscatter shear wave C-scan results provided some indication that the internal cracks seen on the composite fracture surface may be detected before failure using the backscatter shear wave C-scan technique. However, a load should be applied to the specimen to ensure that the cracks are open and more visible when using the technique. No measurement of crack length could be compared to any visual inspection because the specimen could not be sectioned and analyzed, however, the C-scans indicate the crack lengths to be approximately two to three millimeters long. Cracks of three to four millimeters were observed on the fracture surface of test specimens at similar loads using SEM inspection techniques.

SEM inspection yielded information on the size of internal cracks visible on the fracture surface that were propagating in the material, and the number of fibers that fractured in the crack zone. The SEM technique was able to support *in situ* NDE data by showing the existence of internal cracks that would impede the propagation of longitudinal waves and cause a decrease in ultrasonic amplitude. SEM analysis also supported AE data by showing broken fibers and matrix crack growth that produced sound waves detectable by the AE sensors. Most AE fiber fracture events were located at or near the fracture location of the specimen.

The following chapter will compare all data acquired in an attempt to correlate sustained load and IP TMF test conditions based on time-to-failure. Information on fracture surface analysis will be presented in detail to demonstrate similarities in specimen response regardless of test condition.

CHAPTER VI.

CORRELATION BETWEEN SUSTAINED LOAD AND IP TMF

6.1 Mechanical Data

All sustained load and IP TMF test specimens failed faster than baseline samples at all comparable stress levels, and both sustained load and IP TMF test conditions produced failure in a shorter period at 1100 MPa than at 1150 Mpa because of the differences in the material from one specimen to another. Mechanical data from neither sustained load nor IP TMF tests provided any indication as to impending failure. Very small amounts of strain accumulated before failure, so small that strain could not be used as an accurate indication to failure. Sustained load and IP TMF results were compared on a time-to-failure basis at a given stress level. By analyzing several different inefficiency factors, it was determined that approximately 15% of the TMF cycle was equivalent to sustained load conditions for high stress level conditions. The UTS value had to be incorporated as a data point for the data to be fit properly since all 1100 MPa tests failed earlier than 1150 MPa tests. The other 85% of the TMF cycle was time not spent in damage progression since the specimen is not held at constant maximum load and temperature. Figure 40 (a and b) shows the total time-to-failure results based on a 15% inefficiency factor. The empirical fit, however, does not correspond with findings by Nicholas [11] which states an inefficiency factor of 5%. Concentric circle cylinder stress

analysis [20] for this study documented in Appendix G also predicts a 5% inefficiency factor based on comparison of the time necessary to produce equal fiber stresses under both sustained load and IP TMF. The inconsistency is attributable to material quality and damage progression characteristics. In comparing the results for SCS-6/Ti-6Al-4V with the SCS-6/Timetal®21S material studied by Nicholas, the SCS-6/Ti-6Al-4V composite appears to be both fiber dominated from stress applied at temperature over time, and matrix dominated from fatigue in the matrix, each contributing in similar quantities to failure prediction. The matrix dominance in composite failure appears to increase as test stress level is decreased, both for sustained load and IP TMF test conditions. A major difference between the two composite materials is the maximum temperature at which they have been studied. The SCS-6/Ti-6Al-4V composite has been studied at 427°C while the SCS-6/Timetal®21S composite has been evaluated primarily at 650°C. Based on micromechanical computations by Nicholas [10], higher temperature will produce lower stresses in the matrix and higher stresses in the fiber for a given applied maximum stress because of the thermal stress contribution to the overall behavior. Stated otherwise, with a decrease in maximum temperature (e.g., from 650°C to 427°C) the matrix develops tension, and the fiber develops compression. Therefore, matrix fatigue would be more prevalent at the lower temperature. The SEM fracture analysis of the SCS-6/Ti-6Al-4V composite appears to confirm the observation that fatigue under IP TMF involves both fiber fracture and matrix fatigue crack growth, as shown in the figures under section 6.4.

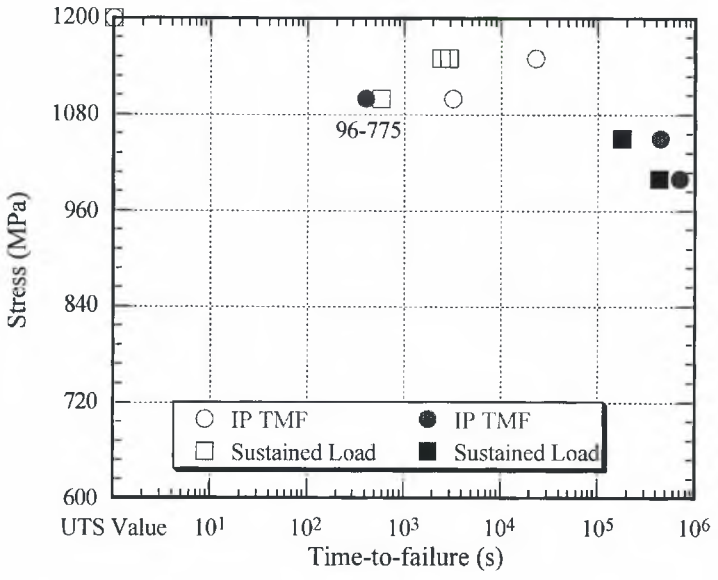

a)

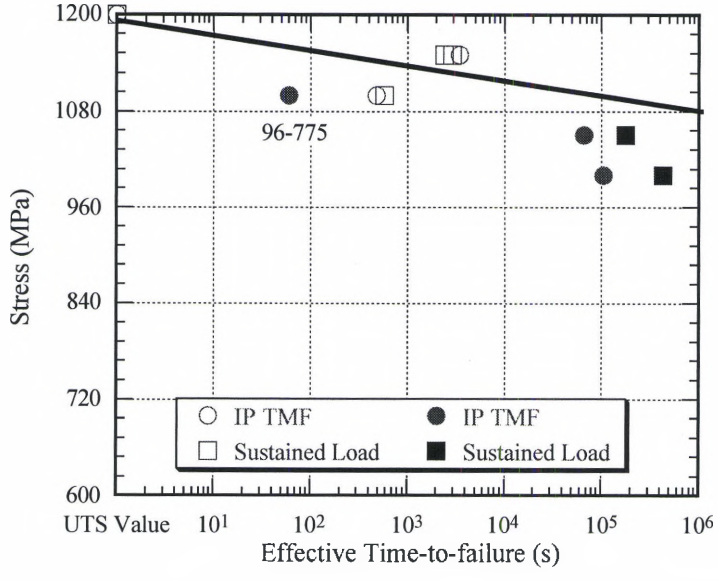

b)

Figure 40. Comparison of IP TMF data to sustained load data at high and low stress ranges a) total time and b) 15% inefficiency time. Specimen 96-775 not included in fit due to number of uncoated fibers in visible in cross section from SEM analysis.

The data were affected by the presence of uncoated fibers in the composite specimens. All specimens exhibited a number of uncoated fibers to some degree. Specimen 96-775 demonstrated an order of magnitude more uncoated fibers than any

other specimen; approximately 20% of the total number of fibers in the cross section from an SEM image were uncoated. Specimen 96-775 displayed an extremely low fatigue life, and therefore, was not included in the fit of the data.

6.2 Ultrasonic Analysis

Ultrasonic modulus data support mechanical strain accumulation and modulus measurements in the inability to show any indication in the change in modulus of the material before failure. Because the two techniques showed no indication of change in stiffness of the composite, it was assumed that the stiff fibers fracture and the composite fails before strain accumulation can occur from matrix plasticity in the composite. Therefore, composite failure was assumed to be fiber dominated. The inconsistency with the inefficiency factor value when compared with that from Nicholas appears to be due to the matrix crack growth observed on the fracture surface. The matrix crack growth was an unexpected failure mechanism in the damage progression of the composite material. The failure mechanism was fiber dominated, and matrix crack growth occurred due to the form of fiber fracture.

Ultrasonic amplitude data demonstrate the ability to track damage progression in either sustained load or IP TMF test condition, and to interrupt a test before failure of the composite. The large initial decrease in amplitude appears to be representative of the damage a specimen accumulates in the first several minutes of the test as documented by MacLellan [12]. The leveling off of the curve would seem to indicate that the composite has reached a point of stability that appears to exist until failure. From SEM analysis of the fracture surface, it was determined that some weak fibers were failing early in

specimen life (near vertical portion of power curve), and that matrix cracks were propagating in the plane of those fiber fractures (near horizontal portion of power curve) until failure. Data from specimens exhibiting a very short life demonstrated sharp decrease in amplitude from beginning to end of each test. However, specimens with longer life spans demonstrated a more gradual rate of amplitude degradation before failure. IP TMF test results showed an overall larger decrease in amplitude than sustained load tests at the same maximum stress and temperature conditions.

6.3 Acoustic Emission Analysis

Acoustic emission data provided information on source characterization and source location for specimens with AE sensors placed on the specimen surface. Only amplitude information existed for specimens tested with the AE sensors on the grips. The AE technique allowed for the determination of composite fracture location before failure by determining the location of the most fiber fracture and matrix crack growth locations. The ability for the operator to use amplitude, location and frequency information to discern between a matrix events and fiber fracture allowed for the two test conditions to be compared. Fiber fractures were found to occur at initial loading, and in groupings until near failure where large groups of fibers failed before composite failure. All fiber fractures occurred at maximum load except for initial loading fractures. AE results indicate fiber dominated damage in both types of loading conditions, supporting the correlation between sustained load and IP TMF conditions.

6.4 Fracture Surface and Composite Analysis

Microscopic analysis of the composite was performed using metallographic techniques. A section of the panel was mounted and polished for SEM inspection. The typical cross section is shown in Figure 41. There were approximately 5 fibers per millimeter in the 8-layer composite. The number of fibers in the gage section of each dogbone shaped specimen, therefore, was approximately 300. No anomalies were visible in the cross-section of the composite panel, except for varying spacing between fibers that has been seen with many other fiber reinforced metal matrix composites [12, 13].

However, examination of specimen 96-775 containing the ultrasonic anomalies was performed after testing to determine the source of ultrasonic attenuation. Other anomalies were discovered in the composite after specimen testing and SEM analysis of several cross sections. Fracture analysis was performed to determine the reason for lower mechanical performance in the material than expected from baseline results. Fracture surface analysis provided reasons for early failure in the composite and compared the damage progression and failure mechanisms in both the sustained load and IP TMF test conditions as will be discussed in the next several paragraphs. Fracture analysis determined the stress range over which the inefficiency factor is valid for the SCS-6/Ti-6Al-4V composite material at 427°C.

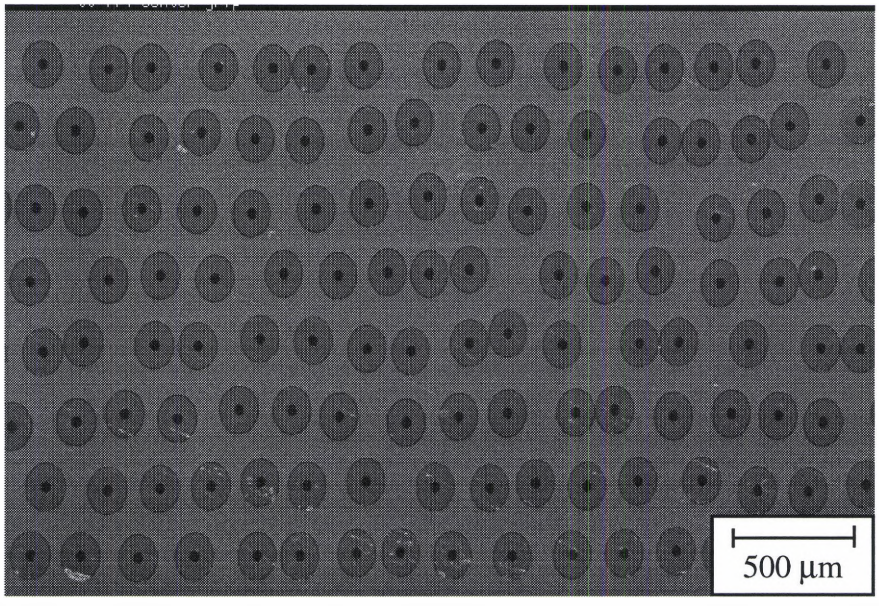

Figure 41. Typical cross section of SCS-6/Ti-6Al-4V composite specimen.

The fracture surfaces were analyzed at magnifications as high as 7000X using an SEM. Figure 42 shows the fracture surface typical of all specimens in panel 9. The surface showed irregularities in fiber and matrix damage progression that was assumed be due to processing methods used by Textron. Groups of fibers were fracturing along one plane, and intergrannular matrix crack growth emanated from the fiber fracture locations.

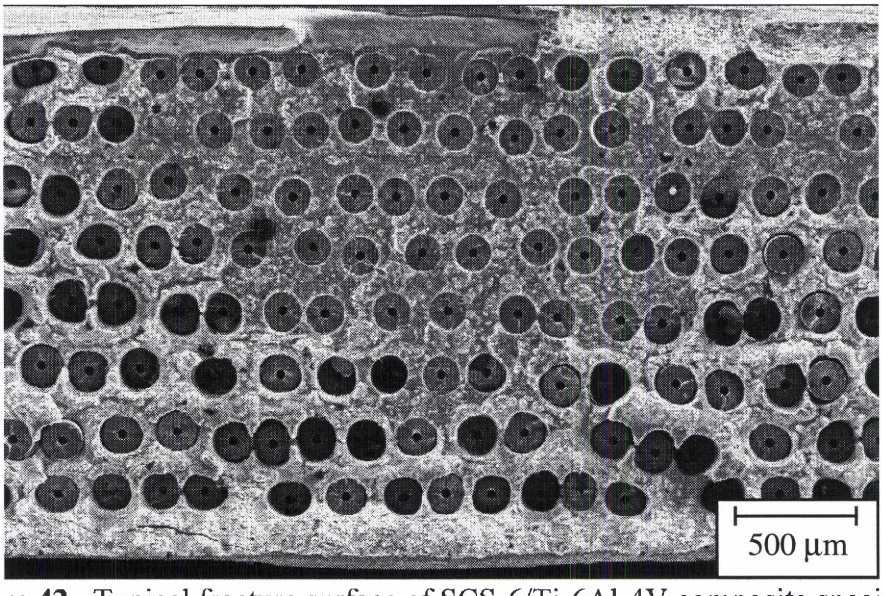

Figure 42. Typical fracture surface of SCS-6/Ti-6Al-4V composite specimen.

A close examination of the fracture surface, shown in Figure 43, demonstrates that the fibers did not all fail in consistent manners. Normally, when a fiber breaks, there is a debond length between the fiber and matrix. Load is redistributed to the rest of the composite. However, as seen in Figure 43 and the previous figure, there are fibers that are not debonding from the matrix after fracture. When a fiber fractures, there is a large concentration of strain at the fiber fracture surface that must be dissipated, usually as fiber/matrix debonding.

If the fiber is unable to debond from the matrix, which is the case for fibers with no coating that have strong interfacial bonds, then the matrix must yield to release the strain. The yielding process occurs in a rapid fashion, and the matrix cracks at a microscopic level. Due to the load applied to the specimen, over time the matrix begins to yield along the grain boundaries as shown in Figures 43 and 44. The fiber fracture, lack of debond, and matrix crack growth was evident on all fracture surfaces for sustained load and IP TMF specimens. Because the fracture surfaces were similar under both test conditions, it was determined that the damage mechanisms were similar at high stress levels near the UTS value of the material.

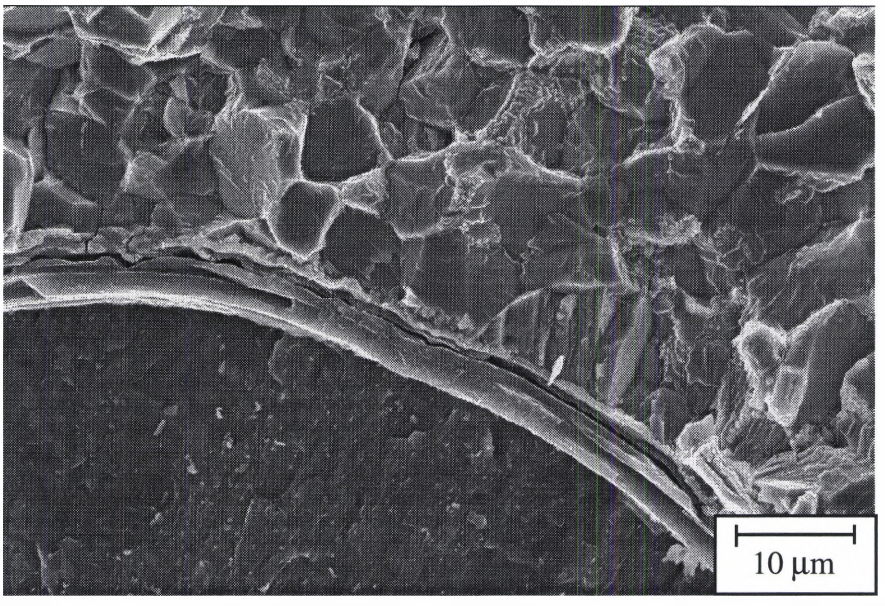

Figure 43. Close examination of fiber failure. Fiber appears to lack coating layer, causing intergrannular matrix crack growth to begin at the fiber/matrix interface.

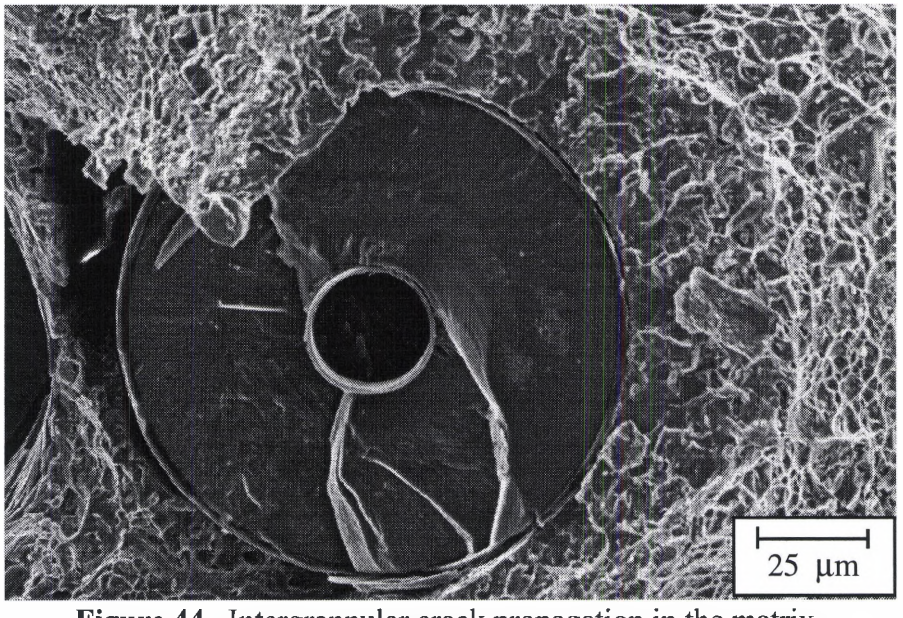

Figure 44. Intergrannular crack propagation in the matrix.

The matrix crack growth was evident before final fracture as shown by Figures 45 and 46. The crack propagates in both intergrannular and transgrannular modes through the matrix. The intergrannular crack growth indicates a time dependence of crack growth.

The time dependence indicates that the matrix cracks exist before final fracture of the composite, and that the cracks may be detected by immersion backscatter shear wave C-scan techniques during interruptions in the test. The specimen may have to be loaded to reduce compressive stresses and open closed cracks. No conclusive evidence has shown the matrix cracks to be detectable using ultrasonic immersion scanning techniques.

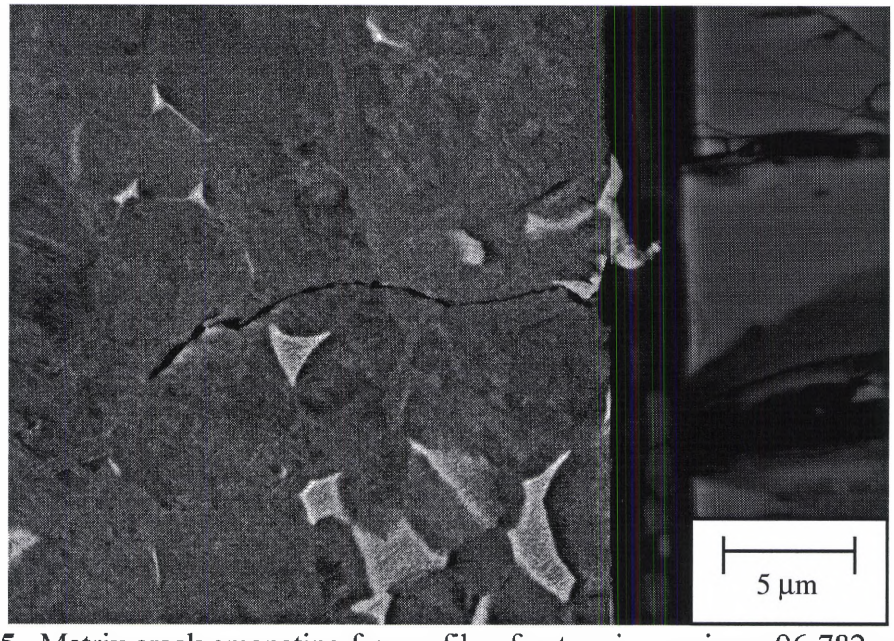

Figure 45. Matrix crack emanating from a fiber fracture in specimen 96-782 away from the fracture surface. There is no debond between the fiber and matrix.

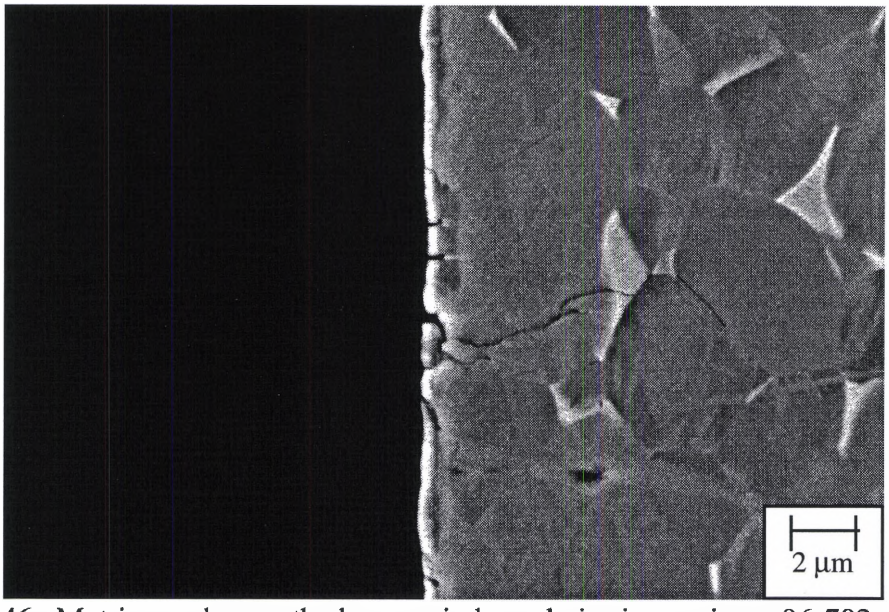

Figure 46. Matrix crack growth along grain boundaries in specimen 96-782. Matrix crack is approximately 11μm in length.

Some of the fibers are remaining bound to the matrix due to the lack of carbon coating. The carbon coating, if present, creates a weak interfacial bond that allows the fiber and matrix to debond and redistribute stresses uniformly. However, if the carbon coating is not present, SiC bonds tightly with titanium and a strong interfacial bond exists, stresses are not uniformly redistributed, and stress concentrations exist near the fiber fracture. The reason for some fibers having no carbon coating within the matrix is unknown, and assumed to be processing error. The carbon coating also protects the SiC from matrix attack of the fibers. If the coating is nonexistent, the SiC may dissolve in the matrix due to a chemical reaction between the two components at processing temperatures, which explains the pieces swimming in the matrix. Microhardness testing of the matrix near uncoated fibers revealed that the SiC may be bonding with the Ti alloy creating a harder matrix near the uncoated fiber as shown in figure 47.

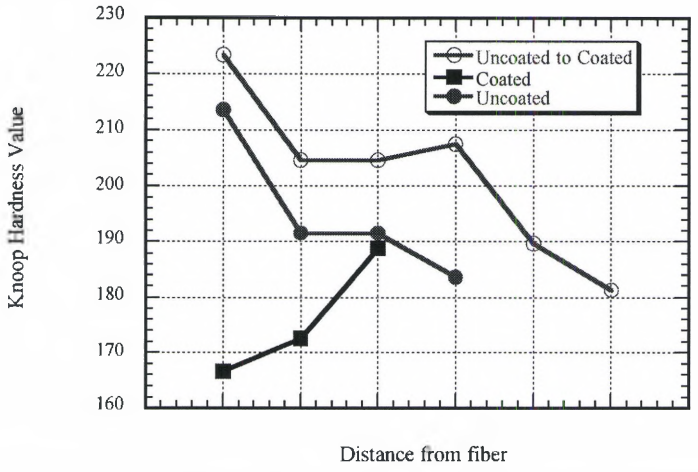

Figure 47. Knoop hardness values for matrix from fibers of various coatings.

Some fibers were determined to have been damaged in processing of the composite. An example of fiber damage is shown in Figure 48. The fiber was crushed during processing, and the matrix consolidated around the broken pieces. Intergrannular matrix fracture was found at crushed fiber locations.

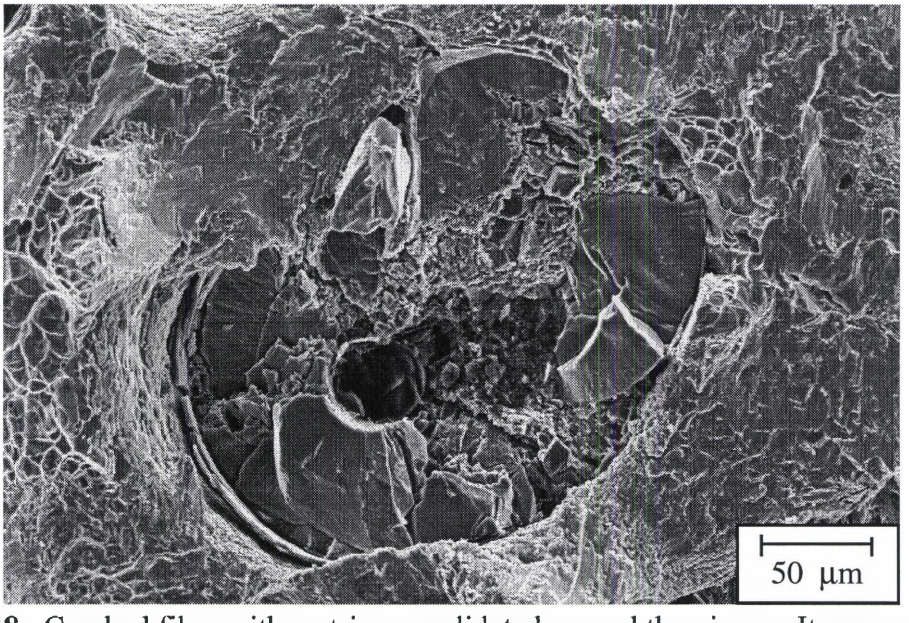

Figure 48. Crushed fiber with matrix consolidated around the pieces. It was concluded that the fibers were broken prior to matrix consolidation in processing.

Further metallographic analysis of the composite cross section yielded critical information regarding the failure of the composite. Analysis of the individual fibers as shown in Figure 49 shows that the outer carbon coating thickness was not constant on all fibers. The coating layer differentiates the SCS-6 fiber from other SiC SCS designated fibers.

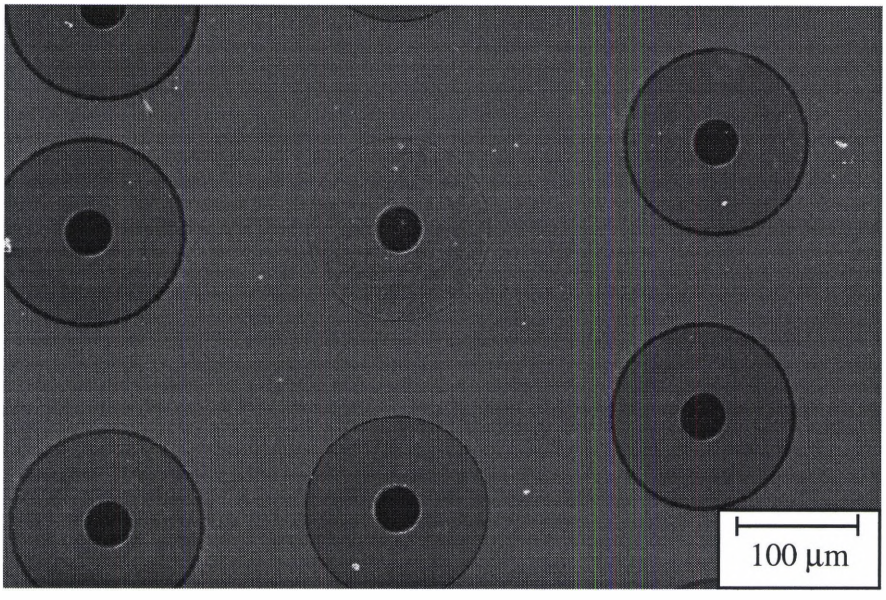

Figure 49. Magnification of 96-775 cross section. Central fiber has no outer carbon coating layer.

Testing revealed fibers without coating have entirely different mechanical properties than fibers with coating after extraction from the matrix through the matrix dissolution technique as discovered by Gambone [54]. Figure 50 (a and b) demonstrates the large difference in fiber strength. Uncoated fibers fail at less than half the stress of coated fibers. No difference in modulus was determined from the fiber tensile tests. The SCS-0 is different from the SCS-6 fiber, only in coating, and the fiber strength of SCS-0

fibers is less than the maximum stresses applied to the fibers for some test stress levels under sustained load and IP TMF conditions, which was determined from FIDEP2 results (Appendix G).

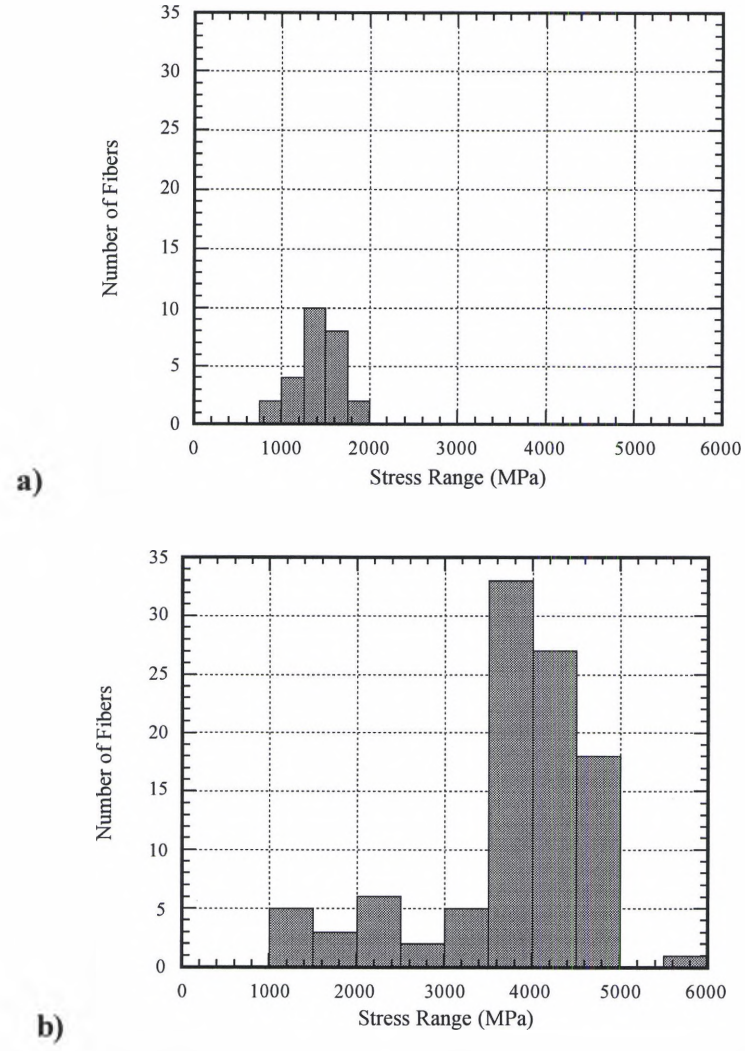

Figure 50. Fiber strengths based on coating determined by Gambone [54]. a) uncoated fibers b) coated fibers.

Studies of the interfacial bond strength of SCS fibers in titanium matrices by Majumdar et al. and others [55-58] have shown that fibers without coating have a higher bond strength than fibers with coating. It is necessary for the fiber to have a weak

interface so that the fiber debonds from the matrix and sheds the load to other fibers instead of matrix cracking occurring due to a high concentration of strain at the fiber fracture site. The coating, which allows for debond from the matrix, is the reason the SCS-6 fiber is used in processing MMC. Tightly interfacial bonded SCS-0 fiber composites appear not to perform as well as SCS-6 fiber embedded metal matrix composites.

Other sections of the composite were examined in the SEM to determine the cause of the dark regions seen on the ultrasonic reflector plate C-scans. A compilation of figures demonstrating the manufacturing defects in the test samples can be found in Appendix I. Certain anomalies include crushed fibers during processing, fiber pieces, missing fiber coating, and incomplete consolidation.

The anomalies present in the specimens appeared to have a direct effect on the performance of the composite. Six to ten uncoated fibers were present in most specimens, causing exceptionally short times to failure. Specimen 96-775 had the most number of uncoated fibers (60) and shortest life of all specimens at any stress level. No differences were noted between sustained load and IP TMF failure that would indicate different failure mechanisms based on fracture surface analysis. Matrix crack growth examined on the fracture surface was very consistent between the sustained load and IP TMF tests. The number of matrix crack growth zones and number of bonded fibers to the matrix at the failure location increased from one or two to five or six zones with decreasing stress for both test conditions. The increase in crack zone size and number of crack growth zones indicates that matrix crack propagation was the large portion of

specimen life, and crack initiation at the fractured fiber locations was a small portion of total specimen life. The total time the composite spent in either initiation or propagation was determined by the number of weak, uncoated, fibers fracturing before the test, or early in the test. The more weak fibers in a particular cross-section, the faster matrix crack initiation took place in the composite, and the sooner the specimen entered the crack propagation stage of life.

As the stress level is decreased, however, different mechanisms appear to influence failure. At 1050 and 1000 MPa, matrix crack growth begins to propagate towards the surface of the specimens. The matrix and fiber is exposed to the environment under sustained load, and matrix embrittlement takes place. Matrix embrittlement weakens the composite, and causes the material to fail earlier than a specimen without surface connected cracking. Therefore, at lower stress levels, different mechanisms cause the 15% inefficiency factor to not be reliable. The inefficiency factor only appears to apply for the SCS-6/Ti-6Al-4V composite in a 100 MPa stress range near the UTS at 427°C. Conclusions will be made in the following chapter as to the ability of the *in situ* NDE techniques to determine a correlation between the sustained load and IP TMF test conditions.

CHAPTER VII.

CONCLUSIONS

7.1 Summary

In situ ultrasonic longitudinal bulk wave and acoustic emission NDE techniques can be used to assess damage progression in an SCS-6/Ti-6Al-4V composite under sustained load and IP TMF conditions. The ultrasonically determined modulus is not sensitive to damage accumulation, which corresponds to the measurements of minimum and maximum strain and small levels of creep strain displayed in the mechanical results. Ultrasonic amplitude monitoring, however, provides information on damage progression within the composite. AE allows for the location and characterization of composite damage to be determined due to new waveform analysis.

Of the two *in situ* techniques, the modal AE technique appears to offer more information about composite damage characterization and location. Knowledge of location, and type of damage as it is happening is key to predicting failure. By correlating acoustic emission events with the time and load at which they occurred, comparisons between different loading conditions can be achieved.

Metallographic and fracture surface analysis supported NDE information on damage accumulation and characterization. Metallographic analysis provided vital information about fracture mechanisms and defects, such as uncoated fibers and fibers

broken in processing, to determine a failure scenario and the stress range over which it is applicable. Poor material properties such as tensile strength, creep and fatigue life were associated with manufacturing anomalies in causing consistently rapid failure in the composite specimens. Fracture surface features such as tightly bonded fibers, crushed fibers, and matrix crack growth existed in samples tested under both the sustained load and IP TMF test conditions. At high stress levels, the damage mechanisms were consistent. As the stress was reduced, cracks propagated to the surface, and the environment affected material performance.

The specimen with the largest number of uncoated fibers demonstrated the shortest life, leading to the belief that fiber coating played a significant role in the time-to-failure in each specimen. More matrix crack growth regions of substantial area were present in specimens tested at lower stresses. Therefore, crack growth represented a large portion of the life of the material. Crack initiation at the fiber/matrix interface was a short period of the overall life of the material.

NDE and metallography, in conjunction with mechanical test data were used to compare sustained load specimen failure to IP TMF specimen failure. Failure mechanisms were concluded to be fiber dominated in both test conditions. The IP TMF test is a longer test than sustained load, however, by taking 15% of IP TMF time to be equal to sustained load time, the data compares well between the two test types at a stress range of 100 MPa below the UTS value. In comparing the results for SCS-6/Ti-6Al-4V with the SCS-6/Timetal®21S material studied by Nicholas, the SCS-6/Ti-6Al-4V composite appears to be both fiber dominated from stress applied at temperature over

time, and matrix dominated from fatigue in the matrix. The SEM fracture analysis of the SCS-6/Ti-6Al-4V composite appears to confirm the observation that fatigue under IP TMF involves both fiber fracture and matrix fatigue crack growth. The matrix dominance in composite failure appears to increase as test stress level is decreased, both for sustained load and IP TMF test conditions. A major difference between the two composite materials is the maximum temperature at which they have been studied. The Ti-6-4 alloy appears to exhibit different strain ranges in thermomechanical fatigue. The increase in the strain range causes matrix crack growth to occur when initiation sites at fiber locations are present. The inefficiency factor appears to differ between matrix alloys, primarily because no matrix fatigue is observed in the Timetal composite, which is tested at a higher temperature

7.2 Recommendations

All recommendations stem from work performed in this study:

1) High resolution C-scanning techniques should be incorporated into material screening prior to mechanical testing of the specimens if the detection of defects is crucial to test results.

2) Acoustic emission sensors should be placed on the specimen to obtain specimen waveforms. Sensors placed arbitrarily on the test frame yield acoustic information on the specimen as it passed through other medium such as a grip, which complicates the waveform analysis.

3) If the sensors cannot be placed on the specimen, then waveguides must be used to propagate the sound from specimen to sensor. A complete understanding of wave propagation through the waveguide material is necessary for its usage.

4) Broader bandwidth AE equipment should be tested to determine if fiber fractures emit frequencies in the 2-20 MHz region.

5) Acoustic emission data should be analyzed using modal acoustic emission theory. The most important part of the event is located in the front of the waveform, being the first extensional and flexural mode. The modal response needs to be analyzed, not the multiple reflections, which is what the old technology analyzes.

6) New methods of placing thermocouples on specimens should be developed so that weld marks are not present on the specimen surface during ultrasonic C-scan analysis. A type of high temperature adhesive may be necessary to use.

7) Higher frequency longitudinal bulk wave signals should be used for possible detection of internal matrix cracking and damage progression.

8) Current AE methods should be expanded to 2D location from the 1D technique currently used. Then fiber fractures may be located with better spatial resolution and can be better confirmed with optical inspection.

9) Single fiber specimens should be processed and tested using AE techniques to acquire fiber fracture waveforms.

10) Further study should be performed on the amount of ultrasonic energy leaking into the grip from the low frequency compressional wave transducers. New grip inserts may have to be used that would minimize the loss of sound into the grip area.

11) Further study should be performed on the change in frequency composition of the longitudinal bulk wave obtained *in situ.* The signal needs to be characterized to determine why exactly the high frequency components are present at high grip stress.

12) All *in situ* techniques should be automated by incorporating their control into the MATE test controller. Automation will allow for *in situ* data to be monitored automatically, and any *in situ* data outside set parameters can cause automatic shutdown of the test before failure, as is currently done with load, strain and displacement limits.

13) Residual strength tests should be performed to determine if strengths are comparable based on the correlation between time-to-failure discussed here.

14) Further ultrasonic immersion C-scans should be performed at load on tested specimens to determine crack growth accumulation within a composite material.

15) Finally, the composite processing may cause different failure mechanisms and unpredictable material behavior as discovered with the SCS-6/Ti-6Al-4V composite. The processing technique should be controlled throughout the procedure, to eliminate any variables that may enter the system.

Appendix A

Panel and Specimen NDE Information

X-ray Radiography

X-ray radiography detects variations in the density of material. A MMC is composed of a high density matrix surrounding a lower density fiber. The variations in density are visible as different shades of gray due to non-uniformity of the composite as shown in Figure 51. The variations in density are mainly attributable to inconsistencies in fiber condition. There can be fiber fractures, missing fibers or gaps, fiber groupings, and undulated fibers, as shown in the figure. For clarity, the inset image shows the fractured specimen 96-F31 cut from the panel at the location of the undulated fibers. The uniformity of the fibers will affect the mechanical behavior of the composite. Undulated fibers have been determined to be detrimental to composite strength by Stubbs et al. [46]. Textron Specialty Materials provided an X-ray radiograph of all panels manufactured by their company. Individual specimen X-ray information showed that the undulated fibers were confined to the area of the panel of which the tensile specimens and excess panel material were obtained. No undulated fibers were detected in any of the specimens used for the sustained load or IP TMF testing.

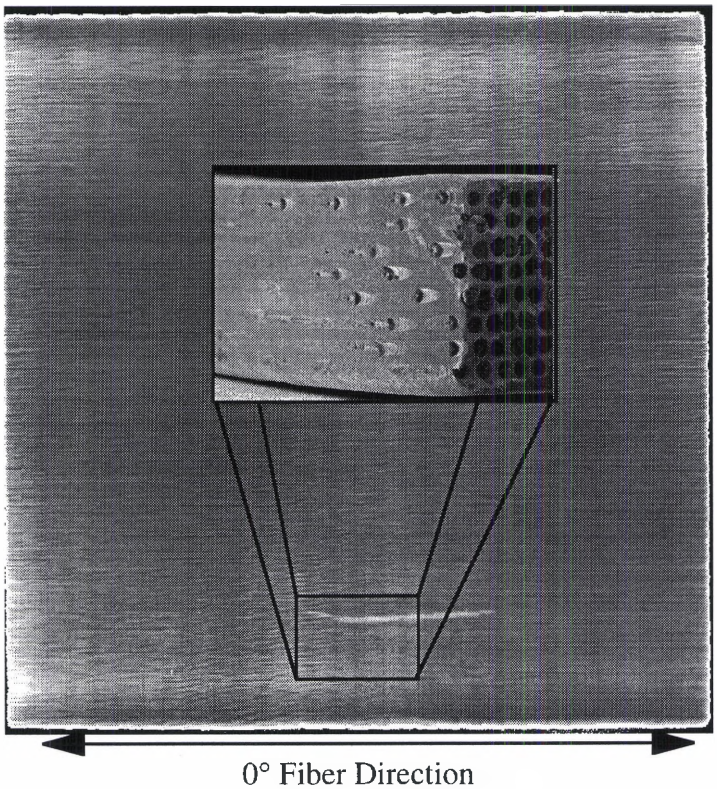

Figure 51. X-ray radiograph of composite panel used in study. Marked region indicates fiber swimming. SEM image from region shows fibers swimming out of loading axis.

Ultrasonic Immersion C-Scans

Ultrasonic immersion C-scans measure signal characteristics from the material such as peak-to-peak amplitude of the reflected ultrasonic signal. There are a variety of ultrasonic scans that can be performed on a material to assess its quality. The reflector plate C-scan is an initial screening technique used to determine consolidation problems such as the existence of undulated fibers, voids, and inclusions that are apparent in the plane of the loading axis. The reflector plate C-scan technique can help in the explanation of poor material causing inexplicable data scatter in theoretical life-prediction modeling of the composite. The reflector plate C-scan is performed using a 10 MHz 76.2 mm focus transducer with a spot size of approximately 900 microns on the surface of the composite. The scan is calibrated using a technique developed by Stubbs and Clemons [59, 60]. Figure 52 shows how ultrasound is sent through the material and acquired for analysis. Figures 53 thru 56 show the reflector plate C-scan results.

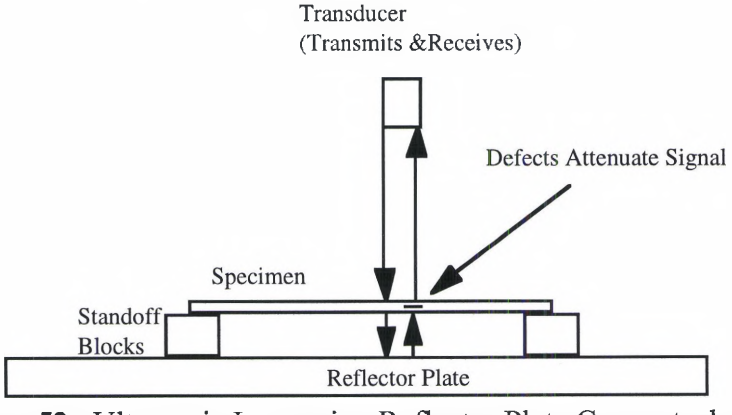

Figure 52. Ultrasonic Immersion Reflector Plate C-scan technique.

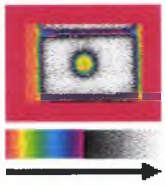

Figure 53. Calibration standard for spatial resolution and scanning repeatability for reflector plate C-scans [60].

Figure 54. Reflector plate C-scan of the 152 mm square composite panel.

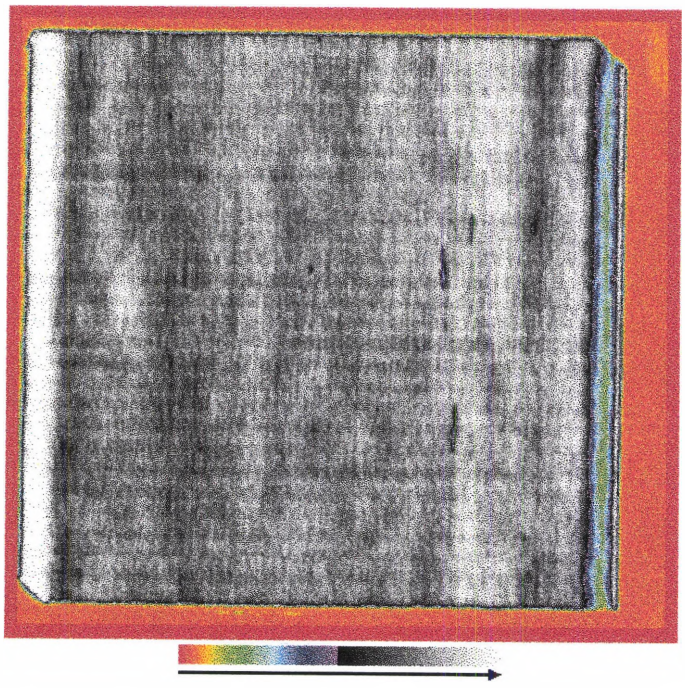

Figure 55. High resolution reflector plate C-scan. Areas of high attenuation are more prominently displayed here than in the previous figure.

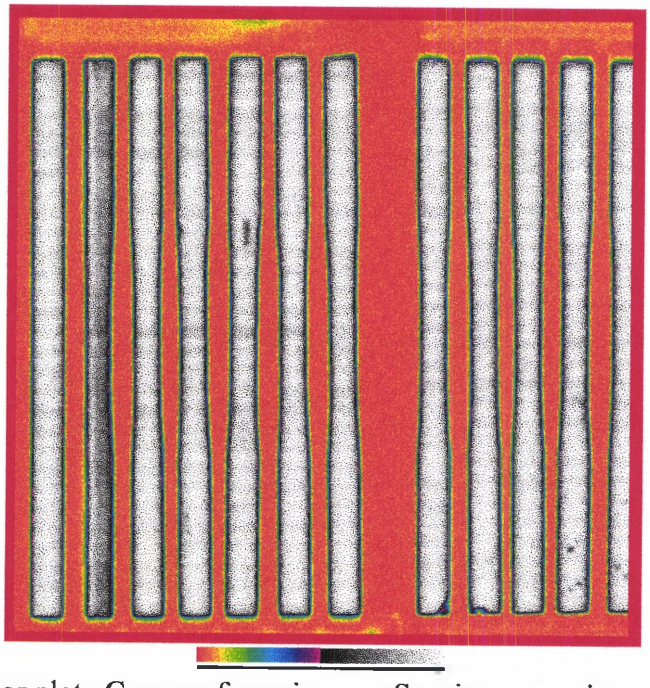

Figure 56. Reflector plate C-scan of specimens. Specimens are in sequential order from left to right. Straight-sided specimen placed at left end.

The next scan that can be performed is the surface wave C-scan which detects any surface and subsurface defects such as matrix cracks or scratches. Figure 57 demonstrates the wave propagation and sensitivity of the surface wave C-scan to surface and subsurface defects. However, not all defects lie near the surface of the material. Figures 58 and 59 show the results of front and backside surface wave C-scans using a 25 MHz, 0.5 inch focus, 0.25 inch diameter transducer.

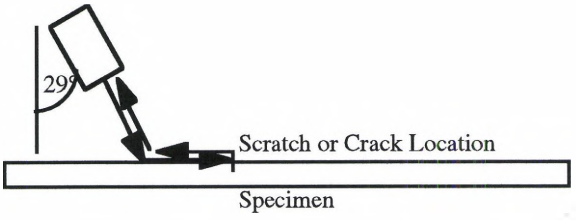

Figure 57. Immersion Surface Wave C-scan technique. Sound propagates along the surface of the specimen. Depth of penetration is dependent on the transducer frequency.

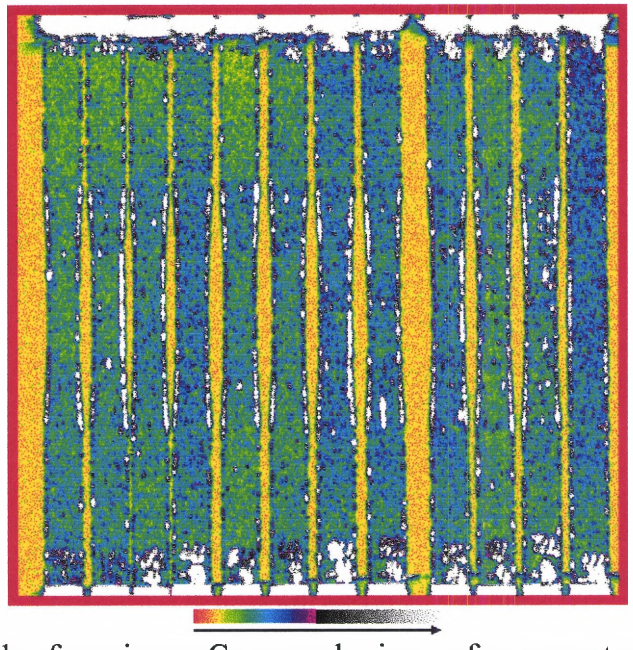

Figure 58. Frontside of specimens C-scanned using surface wave technique. Specimens in sequential order from left to right. Straight-sided specimen placed at right end.

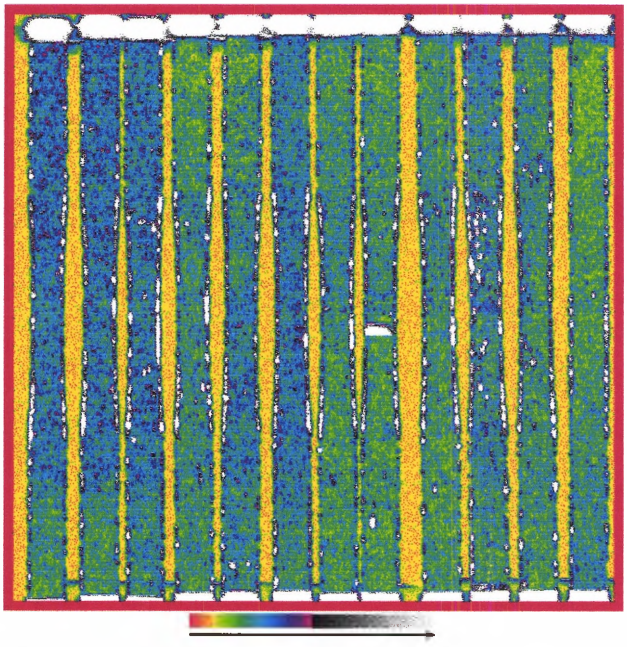

Figure 59. Backside of specimens C-scanned using surface wave technique. Specimens in sequential order from left to right. Straight-sided specimen placed at right end.

The backscatter shear wave C-scan detects internal voids and inclusions that are apparent in the plane perpendicular to the loading axis. Types of defects include fiber and matrix cracks. Figure 60 shows a schematic of the backscatter shear wave C-scan technique and how it detects such anomalies. Figures 61 thru 63 show the results of the backscatter shear wave C-scan technique using a 25 MHz, 0.5 inch focus, 0.25 inch diameter transducer.

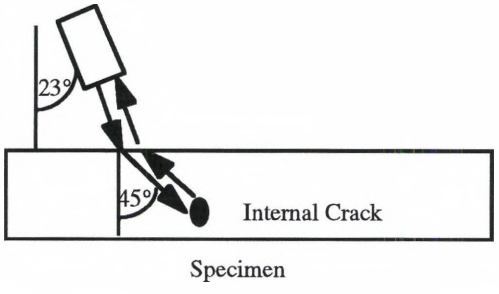

Figure 60. Backscatter shear wave immersion C-scan technique. Sound enters specimen at 45° angle, and reflects off internal cracks.

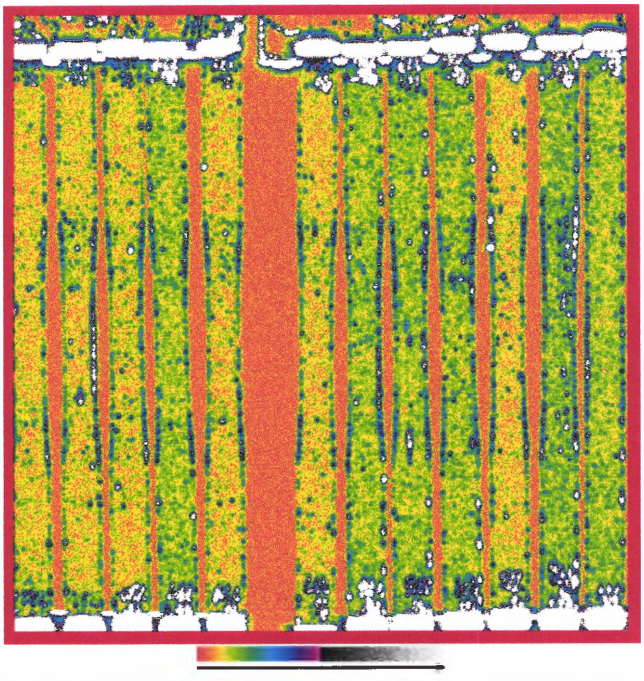

Figure 61. Frontside of specimens C-scanned using backscatter shear wave technique. Specimens in sequential order from left to right. Straight-sided specimen at right end.

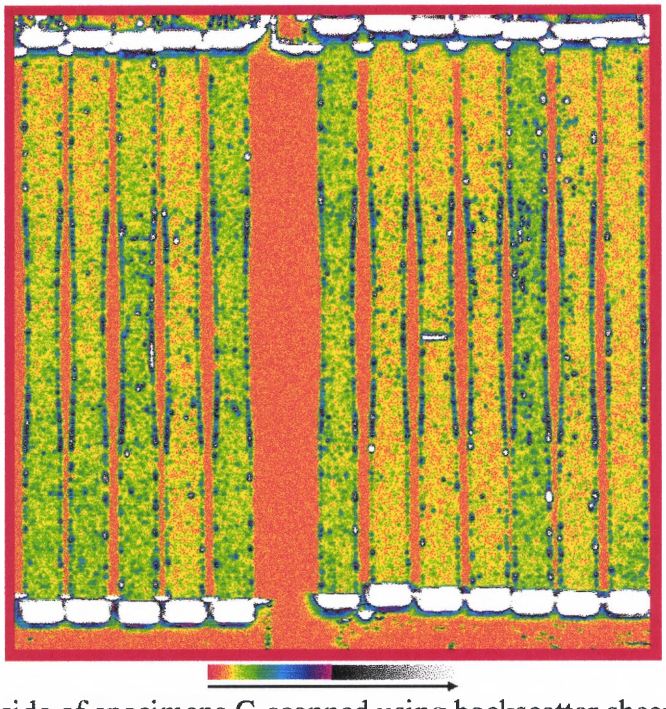

Figure 62. Backside of specimens C-scanned using backscatter shear wave technique. Specimens in sequential order from left to right. Straight-sided specimen at right end.

Appendix B

Test Equipment

Mechanical Test Equipment

The mechanical test machines were designed by the University of Dayton Research Institute (UDRI) for Wright Laboratory, Materials Directorate [61]. The equipment consisted of several major components that offer a multitude of testing conditions. The main components are: the test frame, the controller unit, the personal computer (PC), and the endocal ULT-80 low temperature bath circulator by NESLAB (IP TMF only).

All tests were performed on a horizontal test frame using an MTS servohydraulic load actuator and servo control model 458.20 microconsole. The horizontal test frame was designed to eliminate uneven heating of the specimen through the length of the heated zone in a vertical test frame known as the chimney effect. The test frame assembly was equipped with a 25 kN load cell and actuator that were monitored by the PC and controlled in a feedback control loop system.

Hydraulic friction grips held the specimen in place while under load and temperature (Figure 64). Nickel-base superalloy inserts of various thickness were placed in the grips to allow for variation in specimen thickness. Bending moments applied to the specimen by the load train were minimized in the system through rigorous grip alignment

in the transverse and radial directions of the load train. Alignment tests produced less than 0.5% bending for a 100 MPa stress applied to a stainless steel calibration specimen. Alignment of the test frame ensured proper loading of the specimen without inducing any bending into the system.

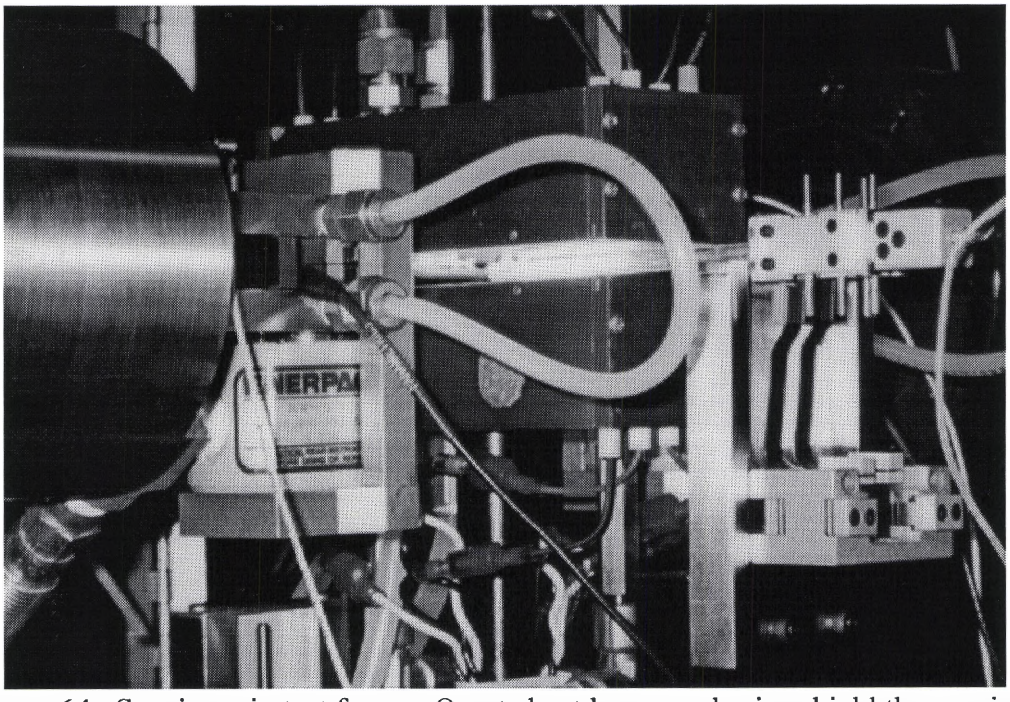

Figure 64. Specimen in test frame. Quartz heat lamps and grips shield the specimen from view.

All UDRI test equipment was automated by MATE (MAterials Testing and Environment) software designed by George Hartman of UDRI [62]. A test can be run in load, strain, or stroke control depending on the control module selected. Test safety limits were set on the MTS controller to halt the test if testing conditions fell outside the set parameters.

The MATE software allows for a multitude of testing conditions to be applied to a specimen. The test conditions include high cycle and low cycle fatigue, tension and compression tests, and sustained load testing. Each test condition is designated a control module that applies and monitors the test conditions input by the operator (a sample of the test conditions are available in Appendix D). The following section will discuss the *in situ* NDE equipment used in conjunction with the mechanical test equipment.

In Situ NDE Equipment

Nondestructive data acquisition was not performed by the automated MATE acquisition program. Two separate computer systems are necessary for incorporating ultrasonic (UT) and acoustic emission (AE) data collection into the mechanical test. Neither *in situ* system is fully automated, but rather each system stands alone and is not controlled by the MATE system, but manually operated. Ultrasonic data acquisition is performed manually, and although AE data acquisition is automatic, data analysis of individual signals could only be performed at the time of acquisition. As more signals are acquired, the previous signals could not be reviewed until the test was completed. Therefore, although the data is acquired *in situ*, data analysis is not performed in real time and cannot be efficiently performed during the test.

The ultrasonic system consisted of a pulser-receiver with a pair of longitudinal unfocused 200 kHz contact transducers used to generate a pulse through the specimen and receive the transmitted signal. A special grip design by Buchanan [14] was necessary to incorporate the transducers into the test frame as shown in Appendix E. The acquired signal was sent to an oscilloscope where a real-time waveform display was monitored.

That signal was then sent to an acquisition board with a 500 MHz A/D 8-bit resolution for signal digitization. Further information on the ultrasonic *in situ* equipment can be found in the literature [12].

The AE system consists of broadband acoustic sensors, preamplifiers, an A/D converter box and a PC that controls the system. The sensors display a flat frequency response roughly bounded by filters from 0.2 to 1.5 MHz. More information on broadband and other types of AE sensors can be found in Appendix F. The sensors are connected to a set of preamplifiers that allow the operator to apply various levels of gain or attenuation to avoid clipping of the signal. The preamplifier is connected to an A/D converter box, which converts the analog signal to a digital waveform. Parametrics such as load and strain also are input into the converter for correlation between AE event and mechanical state of the specimen. The A/D box allows for a multitude of signal manipulations such as threshold, gain, time delay, and filtering. The final output is sent to a third PC and the captured waveform is displayed on screen. Signal analysis is performed on the PC after data acquisition is complete. The signals must be characterized using modal acoustic emission techniques and location of the event must be determined from time of flight (TOF) data and velocity measurements acquired during lead break calibration.

Both NDE techniques require the use of contact transducers for signal clarity in acquisition. The couplant used in the ultrasonic longitudinal bulk wave testing was a Panametrics high viscosity SWC high refined honey couplant for RT operation, the conditions of which could be met in the grip cavity. The high viscosity of the couplant

was necessary to ensure no significant evaporation during testing due to changes in the humidity levels in the laboratory. The couplant was tested for changes in amplitude over time, and for a testing period of 12 days, the peak-to-peak amplitude remained constant to within 1% of the nominal value. The couplant used for the AE equipment was Dow Corning High Vacuum Grease with an operating temperature up to 150°C used by Digital Wave Corporation.

Appendix C

Composite Constituent Information

Ti-6Al-4V Alloy

The Ti-6Al-4V is a titanium based alloy with a nominal composition of 6% aluminum and 4% vanadium by weight. The Ti-6Al-4V alloy has a density of 4.44 g/cc, a melting range of 1600°C to 1670°C and a room temperature (RT) modulus of elasticity of approximately 113.8 GPa. The aluminum acts as an alpha phase stabilizer and accounts for the Ti-6Al-4V alloy's excellent properties at elevated temperatures. The purpose of the vanadium is to stabilize the beta phase, making it possible to strengthen the alloy by heat treatment. Ti-6Al-4V is of a duplex nature, exhibiting a fine grain structure that is good for fatigue crack initiation resistance, but poor for fatigue crack propagation resistance. The information presented in this section along with tensile and compression data are available from RMI Titanium Company [63].

SCS-6 Fiber

The SCS-6 silicon carbide (SiC) fibers are produced by chemical vapor deposition (CVD) processing at Textron Specialty Materials Division. Hydrogen reacts with a mixture of chlorinated alkyl salines at the surface of the heated substrate monofilament. The SiC deposit consists of poly crystals of ß-SiC. The carbon monofilament (CMF) is originally spun from a pitch-based material, and then heat treated to form the final

substrate. The 142 μm diameter fiber consists of a 33 micron carbon core with a layer of silicon carbide on the core. Two different grades of thin carbon coatings totaling 3μm in thickness are then applied for fiber protection in the interfacial bonding with the matrix [64]. The thin carbon coatings also serve to maintain the fiber strength at high composite stress levels as well as provide matrix compatibility [65].

Extensive research has been performed on the SiC fibers. Casey and Geller [66] performed an Auger evaluation of a standard SCS-6 fiber with the following results. The surface coating is approximately 90 at. % C and 10 at. % Si. The Si/C ratio is 1:1 from the inner edge of the surface coating into the mid-range point. The mid-range point is located at approximately half the radius of the fiber and is characterized by a slightly darker shade of gray due to the increase in carbon content. At the mid-range point there is a transition from rough to fine grain SiC. From the mid-range point to the CMF, the SiC becomes gradually more carbon rich, consisting of 55-60 at. % C and 40-45 at. % Si adjacent to the substrate. Approximately 1 micron of pyrolytic carbon exists between the SiC and the CMF.

Data from high temperature fiber tests show that at least 90% of the fiber strength is retained up to 870°C, and about 80% strength up to 1090°C. Above 1090°C, a substantial decrease in strength is observed. Therefore, the SCS-6 fiber is capable of providing substantial reinforcement to composites at elevated temperatures [65].

SCS-6/Ti-6Al-4V Composite

The SCS-6/Ti-6Al-4V composite was fabricated under contract by Textron Specialty Materials. The composite forming process began with chemically etched and subsequently rolled Ti-6Al-4V foil layers exhibiting a nominal thickness of 0.114 ± 0.012 mm. The woven preform consisted of SCS-6 fibers (5 fiber ends per millimeter) and Ti-6Al-4V cross weave wire 0.048 - 0.051 mm in diameter.

The composite panel was unidirectional with 8 layers of fiber mat and 9 layers of Ti-6Al-4V foil plus an extra layer of the metal alloy on top and bottom for a total of 11 layers. All Ti-6Al-4V foils were lightly acid etched to remove any oxides. Each composite panel was individually bagged utilizing AISI 310 stainless steel. A 0.127 mm molybdenum foil was placed on each panel surface to prevent panels from adhering to one another. No binders, glue, or release agents were utilized for the lay-up procedure.

All welding was performed in an inert atmosphere or under a 13 milliPascal vacuum pressure. Before final electron beam welding, each bag was off gassed at 480°C for 1 hour at 13 milliPascals, and subsequently helium leak checked. The panels were subjected to 7 MPa of He for 2 hours. The panels were then subjected to hot isostatic pressing (HIP), the details of which can be found under contract No. F33601-95-C-0029. The stainless steel bags and molybdenum foils were removed chemically with a solution of nitric acid and water.

Appendix D

Test Log Sheets

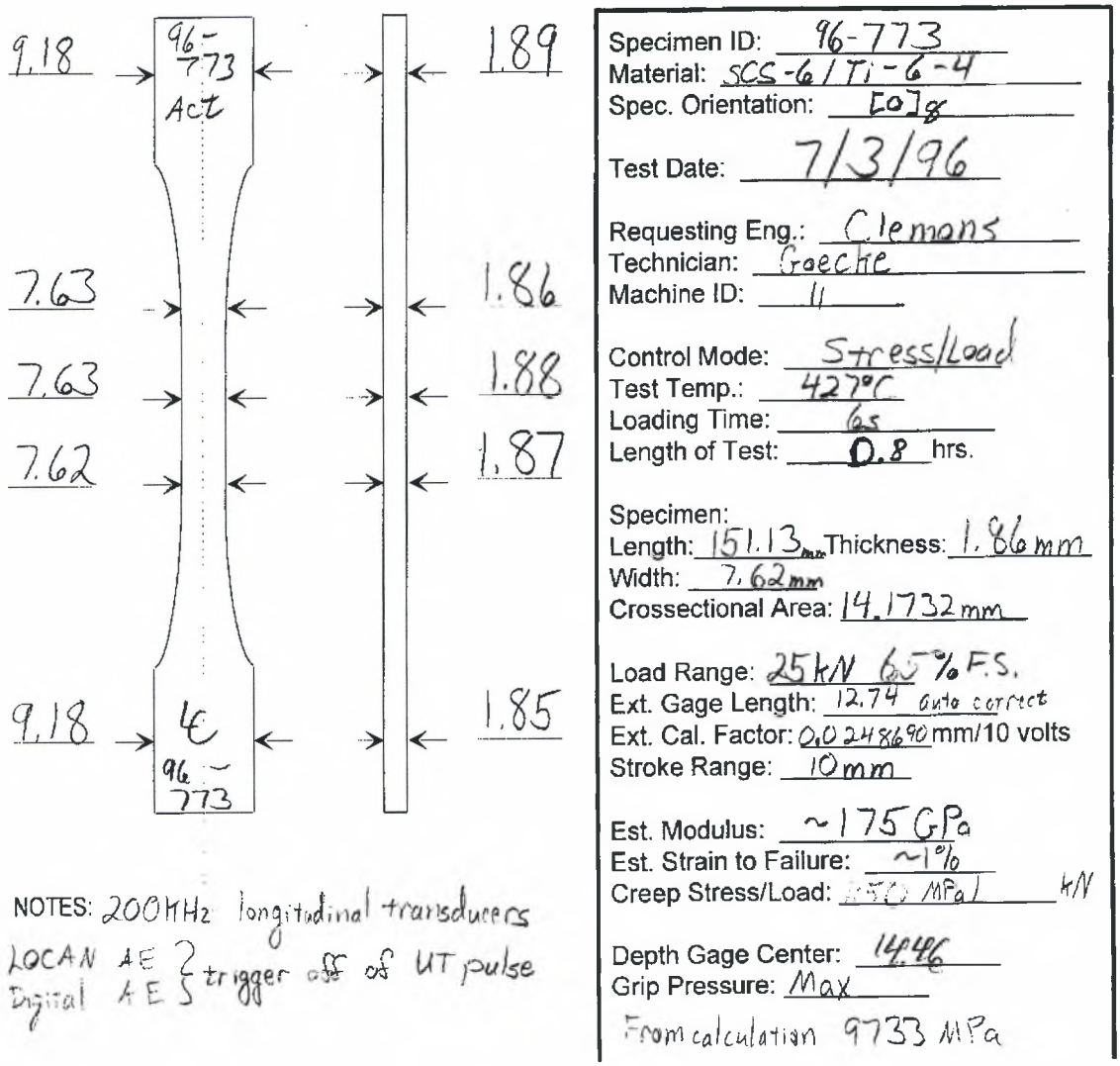

Figure 65. Dogbone creep specimen log sheet. Information for performing test.

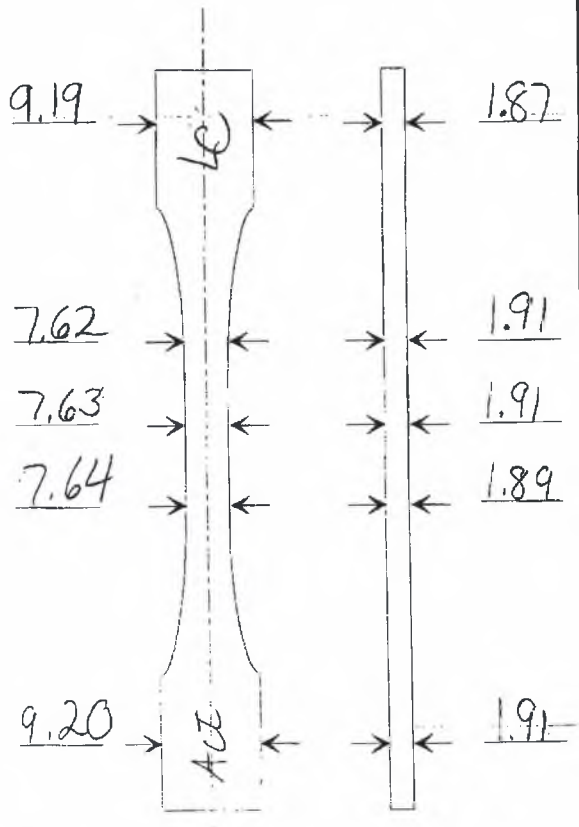

Specimen ID: 96-774
Material: SCS-6/Ti-6-4
Spec. Orientation: [0]8
Test Date: 7/11/96
Requesting Eng.: Clemons
Technician: Goecke
Machine ID: 11
Control Mode: Load
Ramp Rate: 50 s
Test Temp.: max. 427 min. 23
Specimen Length: 151.12mm
Avg. Spec. Thickness: 1.89mm
Avg. Spec. Width: 7.62mm
Ext. Gage Length: 12.375
Test Stress: max. 1150 min. 57.5
Test Phase: In-Phase
Est. Strain to Failure: ~1%
Depth Gage Center: 14.45mm

Notes: 1150 MPa Max grip pressure
XA = 14.40 mm²
RT Modulus = 211 GPa
UT Filter changed .1 MHz → .03 MHz

Figure 66. Dogbone TMF specimen log sheet. Information for performing test.

Appendix E

Ultrasonic Grip Drawing

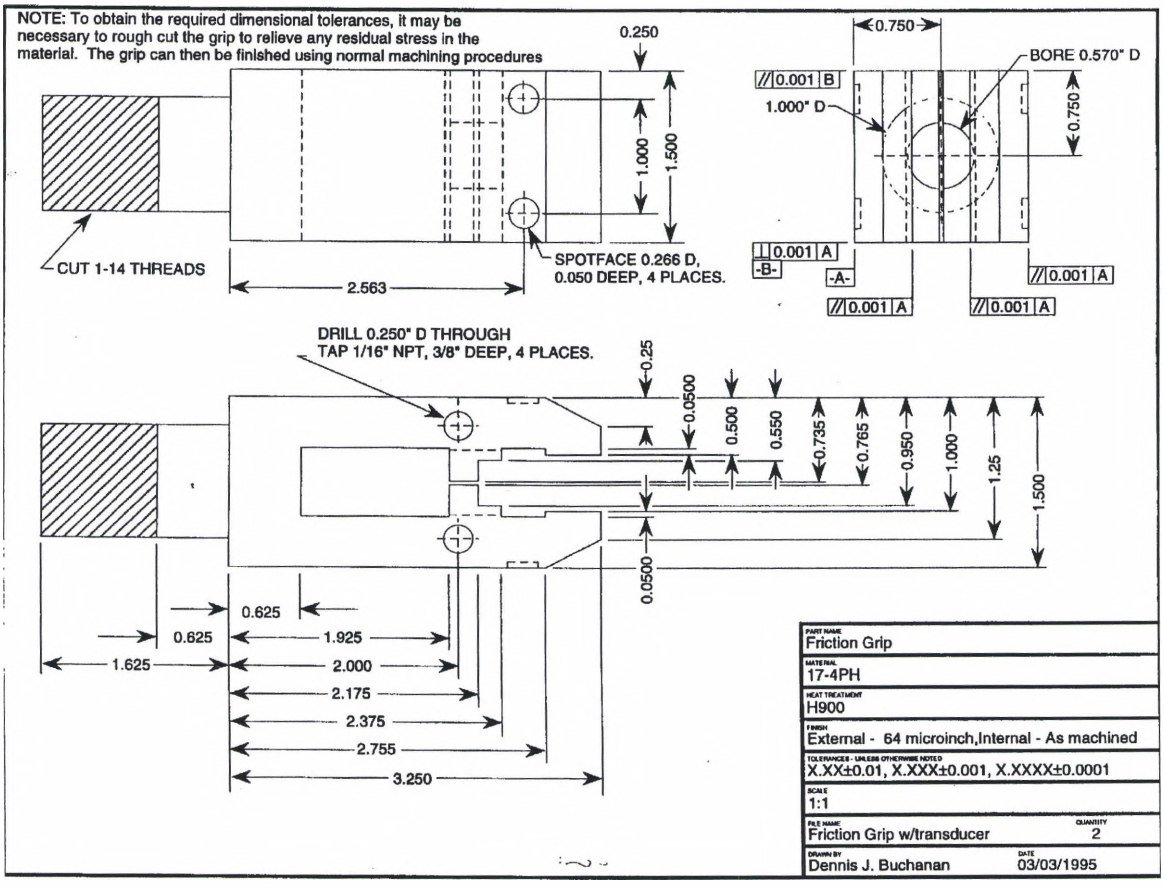

Figure 67. Grip design by Buchanan [14] used to allow transducer contact with end of specimen to propagate longitudinal waves through the length of the test specimen.

Appendix F

AE Sensor Characteristics

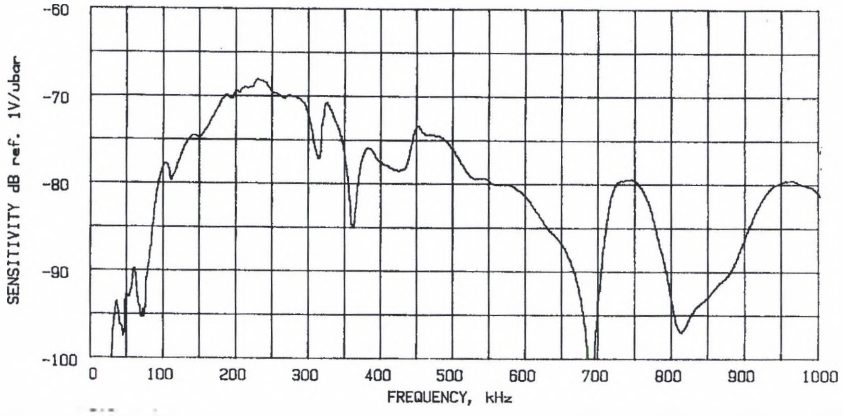

Figure 68. Example of a resonant sensor response (PAC Micro 30 by Physical Acoustics) to a broadband frequency input. Note there are areas of high sensitivity, but also areas of no sensitivity as seen at 700 kHz.

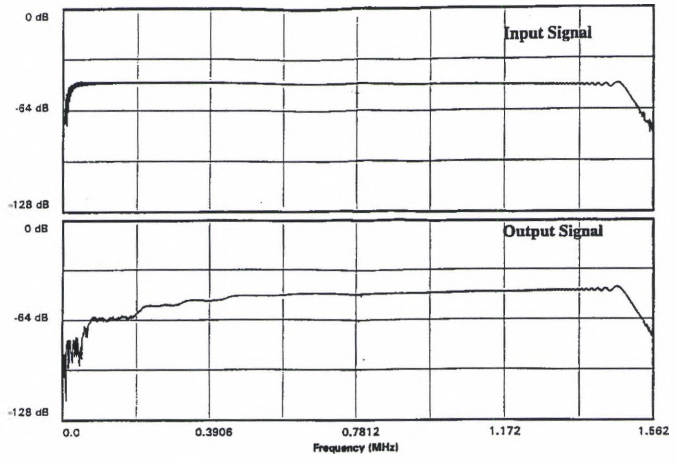

Figure 69. Broadband acoustic emission sensor response (B1025 AE sensor by Digital Wave) to a broad frequency range, the flat frequency response allows the broadband acoustic sensor to capture a wider frequency spectrum from acoustic emission events.

Appendix G

FIDEP2 Results for Test Stress Levels

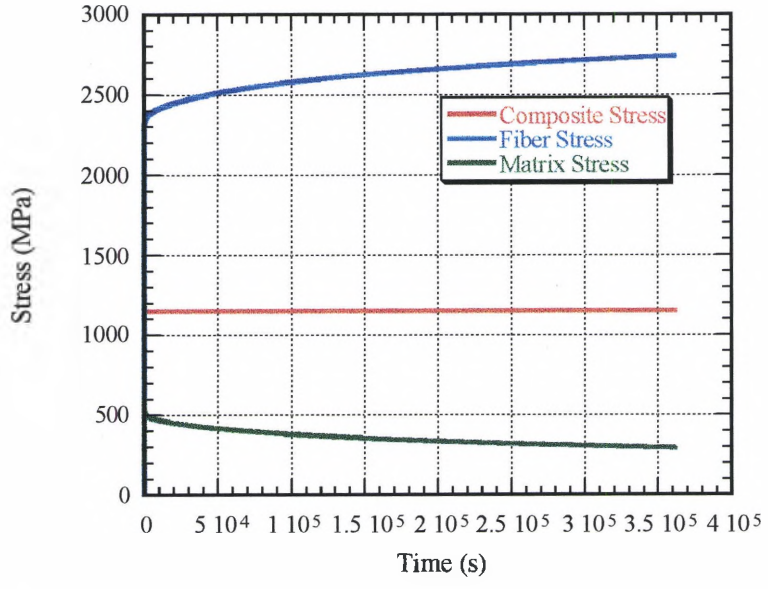

a)

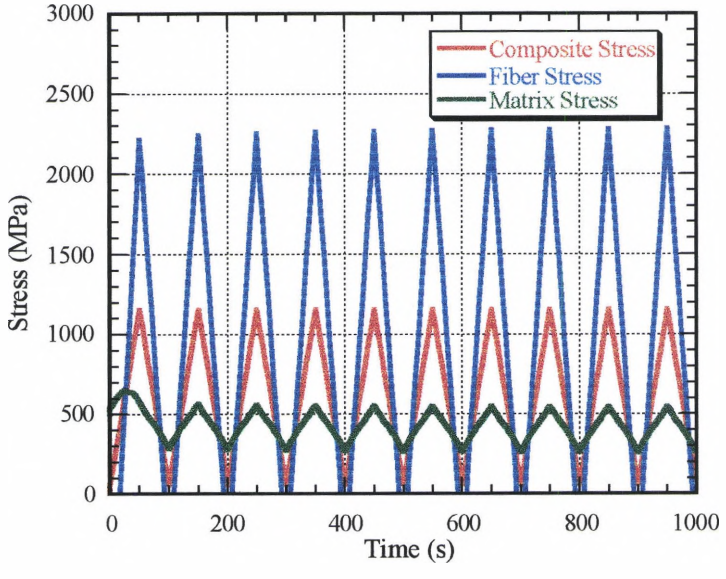

b)

Figure 70. Composite stresses at 1150 MPa for a) Sustained Load and b) IP TMF. The time scale chosen demonstrates the change in stresses as the test time progresses.

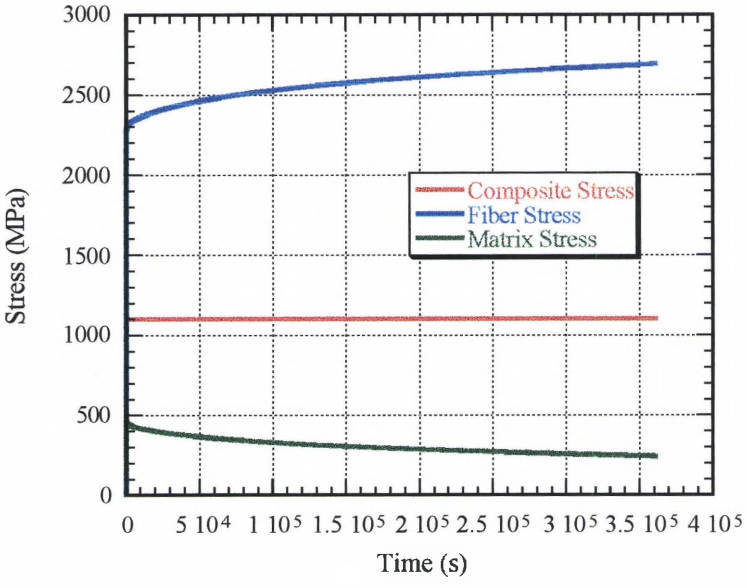

a)

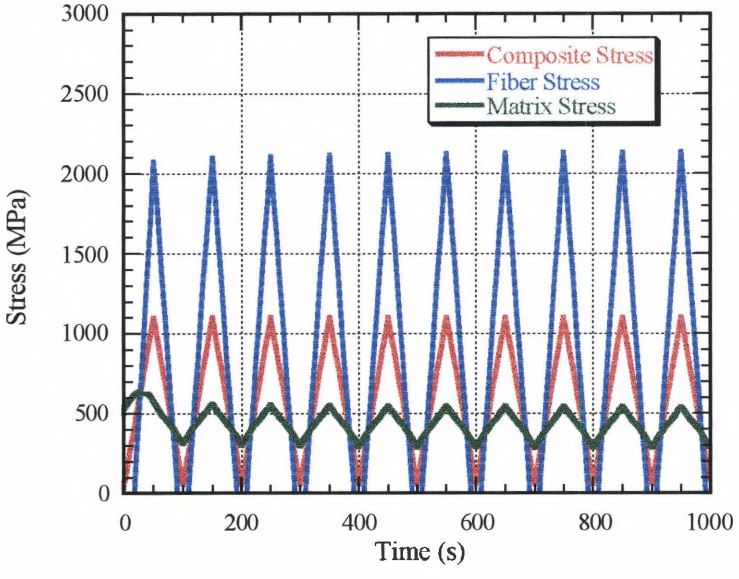

b)

Figure 71. Composite stresses at 1100 MPa for a) Sustained Load and b) IP TMF.

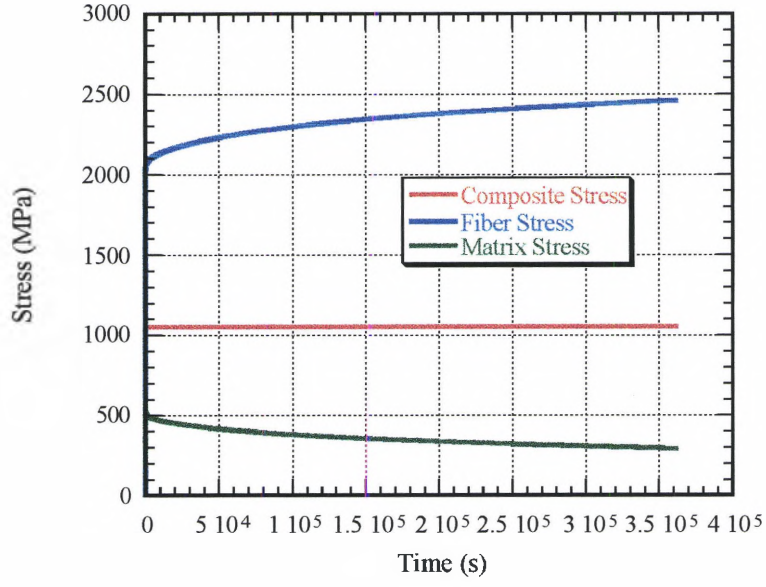

a)

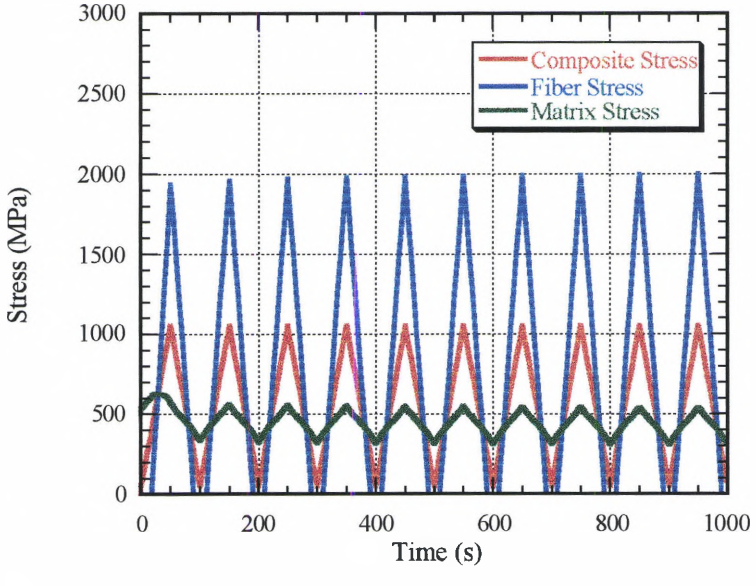

b)

Figure 72. Composite stresses at 1050 MPa for a) Sustained Load and b) IP TMF.

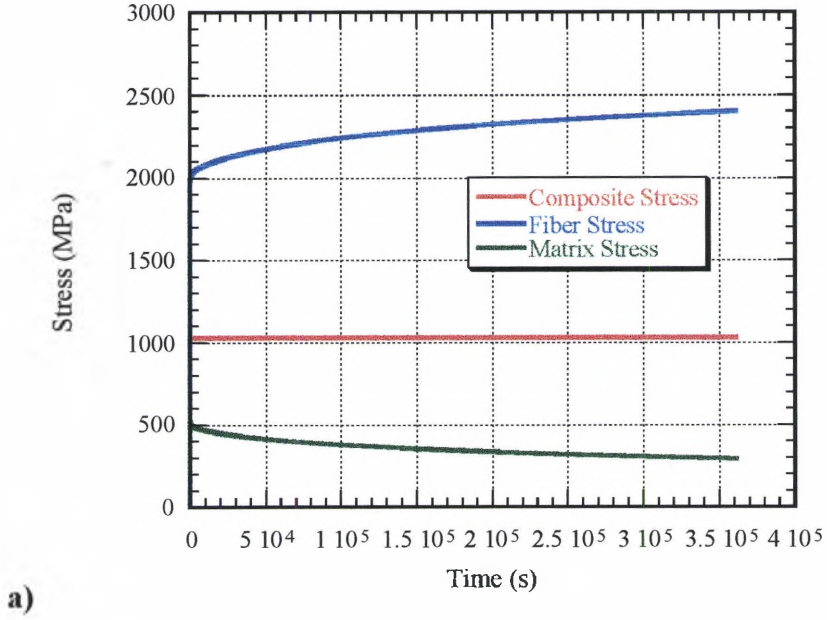

a)

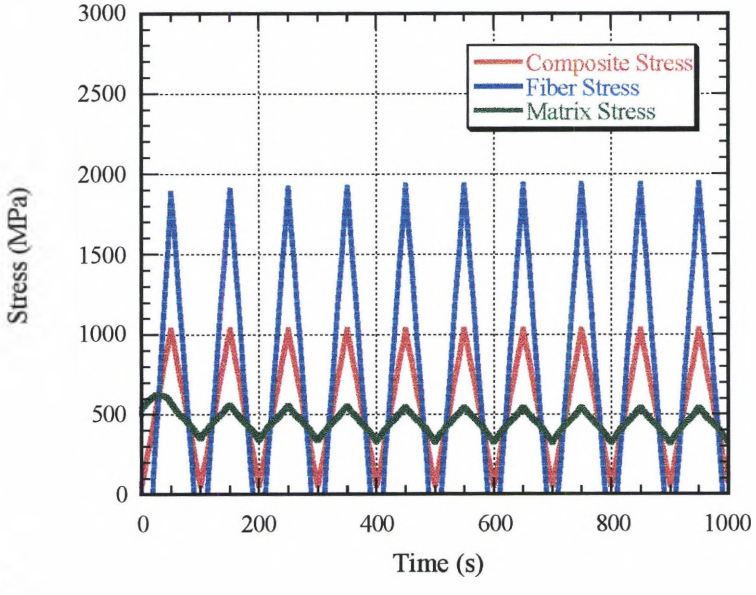

b)

Figure 73. Composite stresses at 1030 MPa for a) Sustained Load and b) IP TMF.

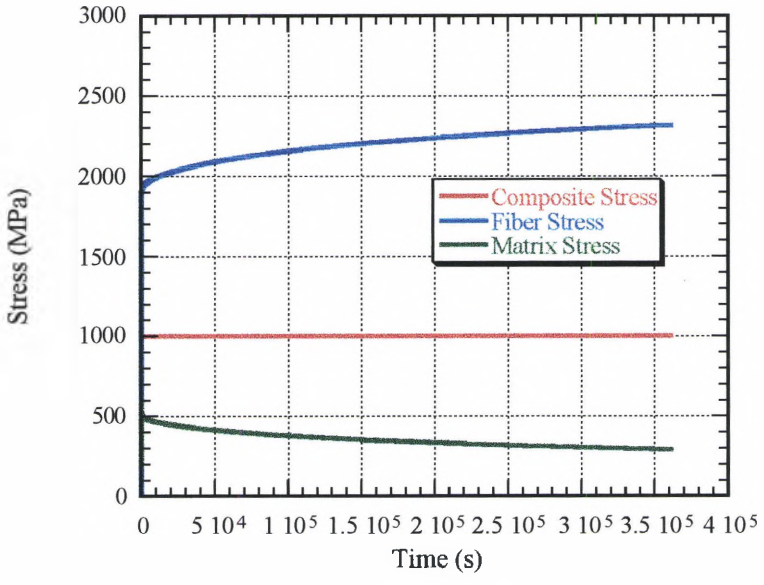

a)

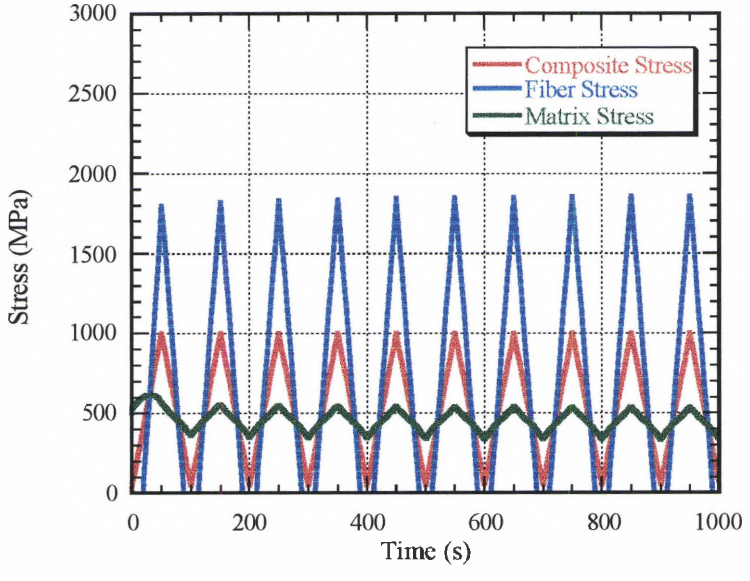

b)

Figure 74. Composite stresses at 1000 MPa for a) Sustained Load and b) IP TMF.

Appendix H

Individual Specimen UT/AE and Mechanical Data Comparisons

96-771: Tensile at RT

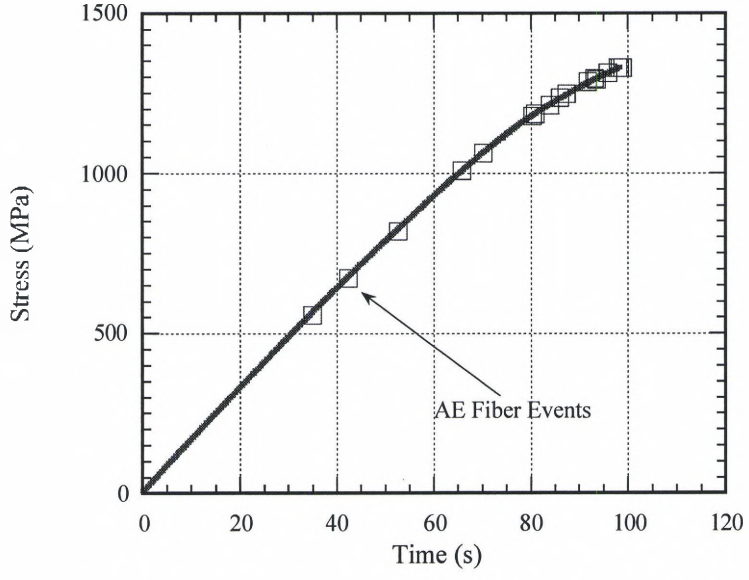

Figure 75. AE Data collected during tensile test.

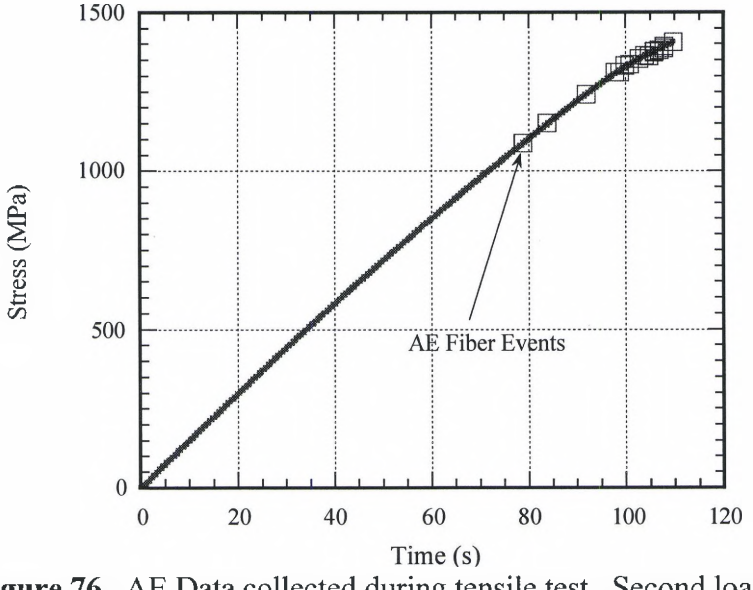

Figure 76. AE Data collected during tensile test. Second loading.

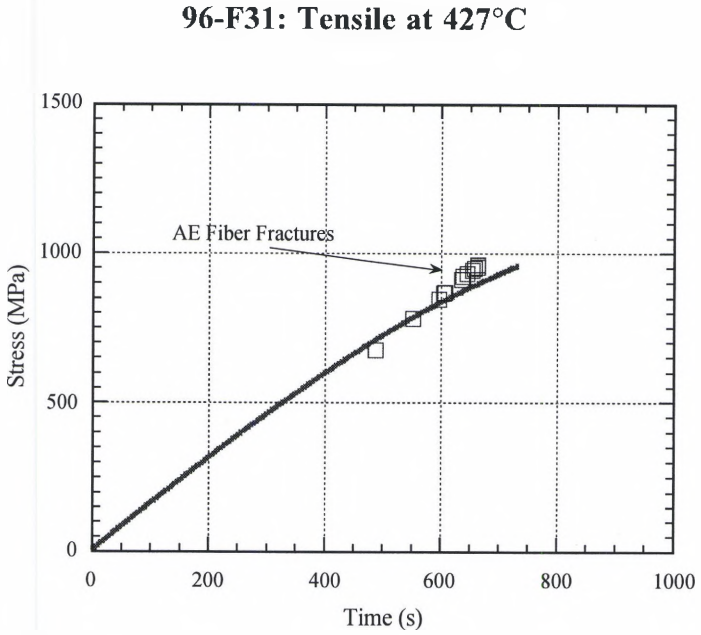

Figure 77. AE data collected during high temperature tensile test. AE stress measurements did not exactly match measurements recorded by the MATE software due to errors in the AE software.

96-772: Sustained Load at 1030 MPa (Interrupted test)

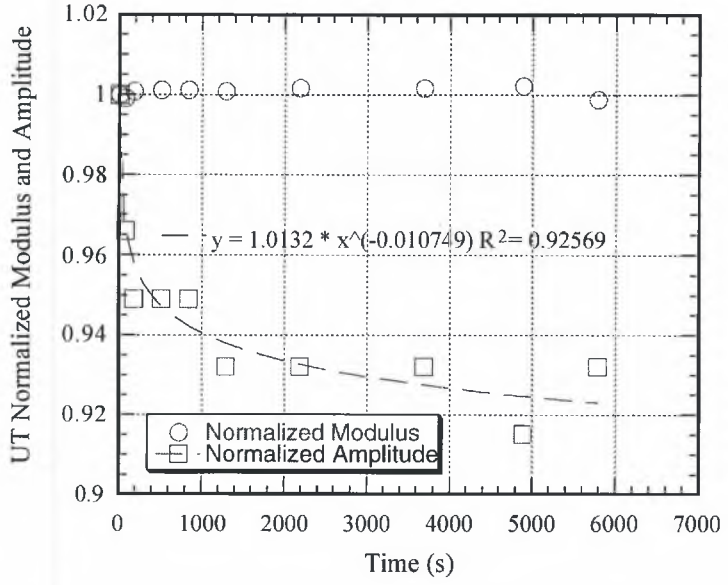

Figure 78. Modulus and amplitude data. Amplitude is fit to power equation.

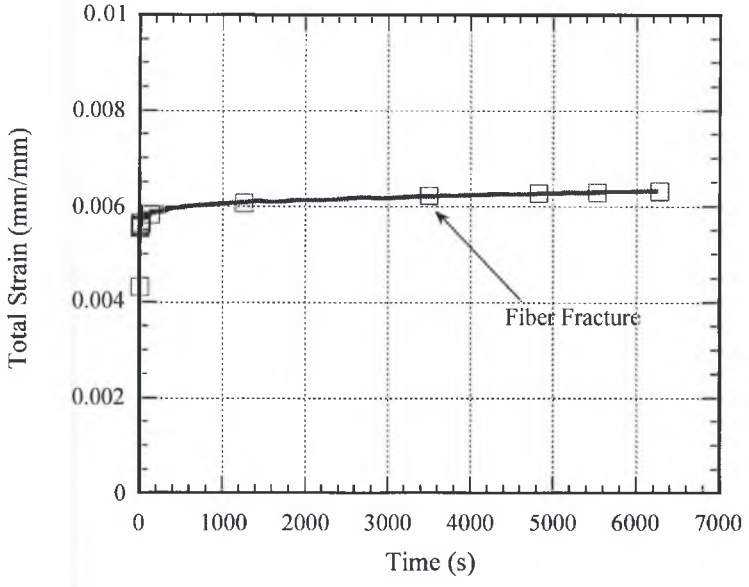

Figure 79. AE data overlaying mechanical strain data.

96-773: Sustained Load at 1150 MPa

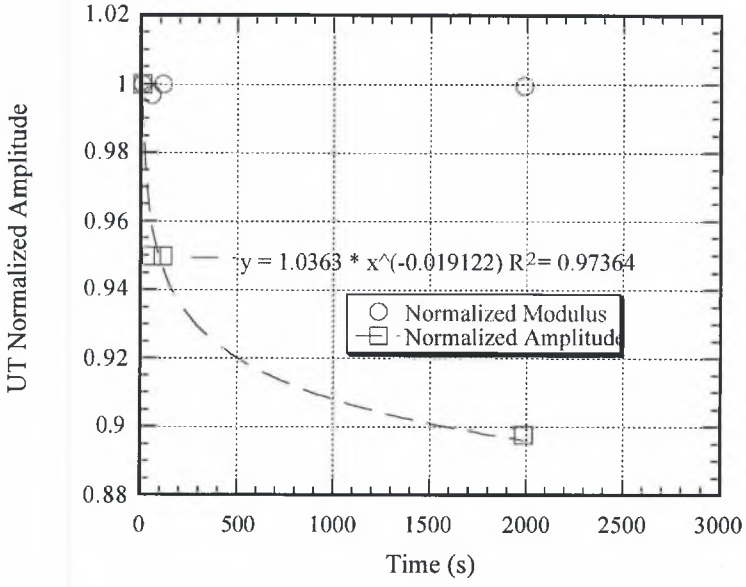

Figure 80. Modulus and amplitude data.

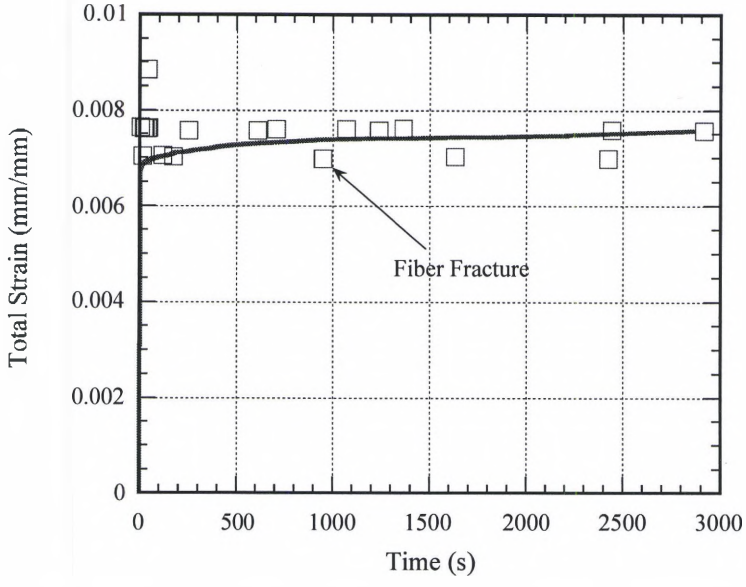

Figure 81. AE data overlaying mechanical strain data.

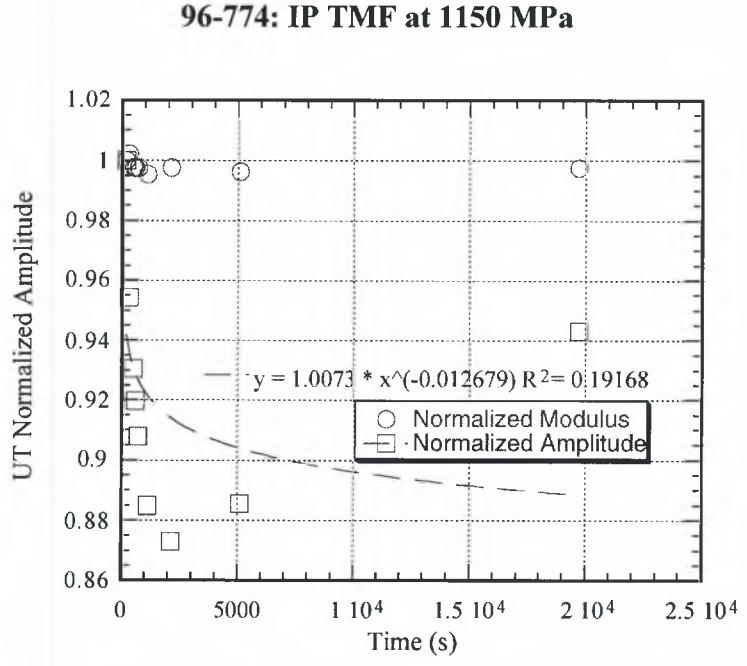

Figure 82. Modulus and amplitude data.

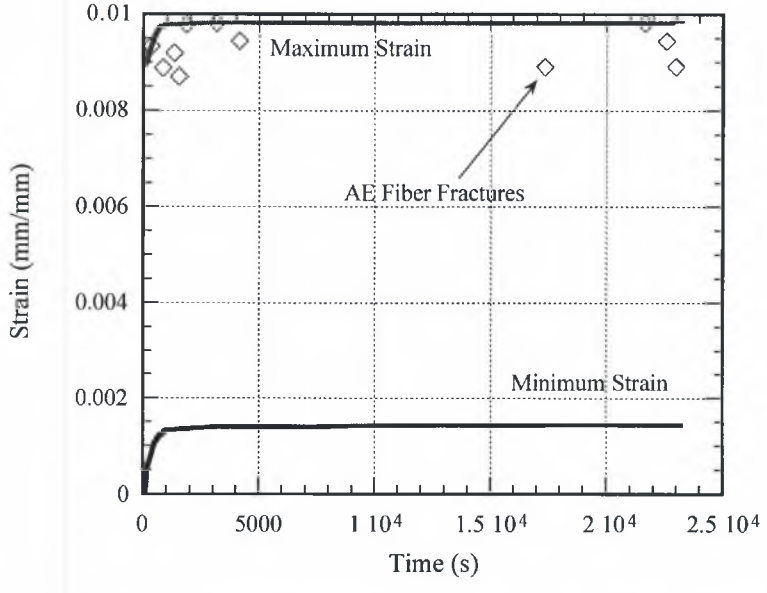

Figure 83. AE data overlaying mechanical strain data. Events deviating from the maximum strain line are due to scatter and events occurring near maximum load.

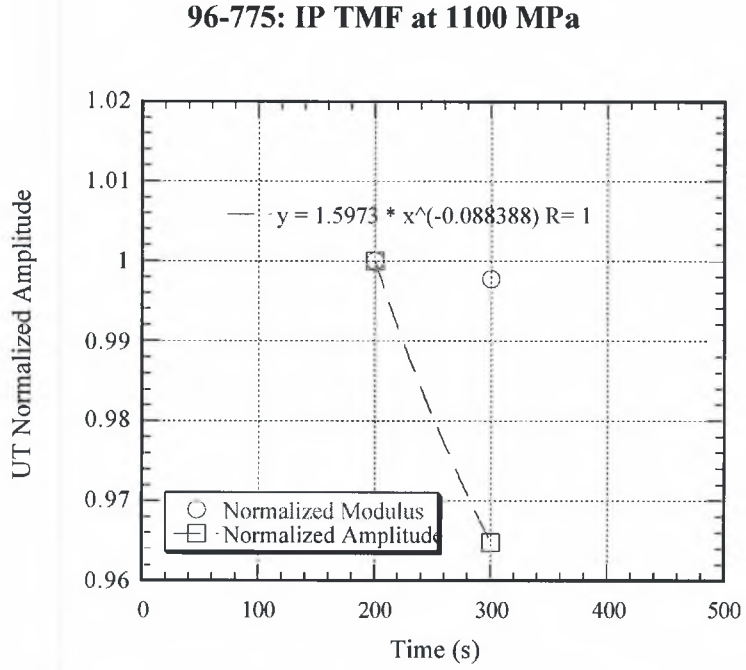

Figure 84. Modulus and amplitude data. Data was not acquired on the first cycle.

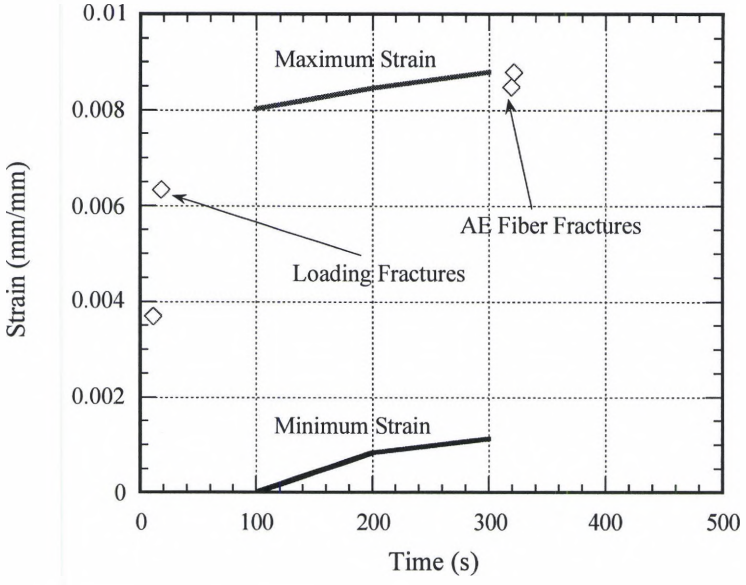

Figure 85. AE data overlaying mechanical strain data. Fiber fractures occurred on loading and at composite fracture.

96-776: Sustained Load at 1150 MPa

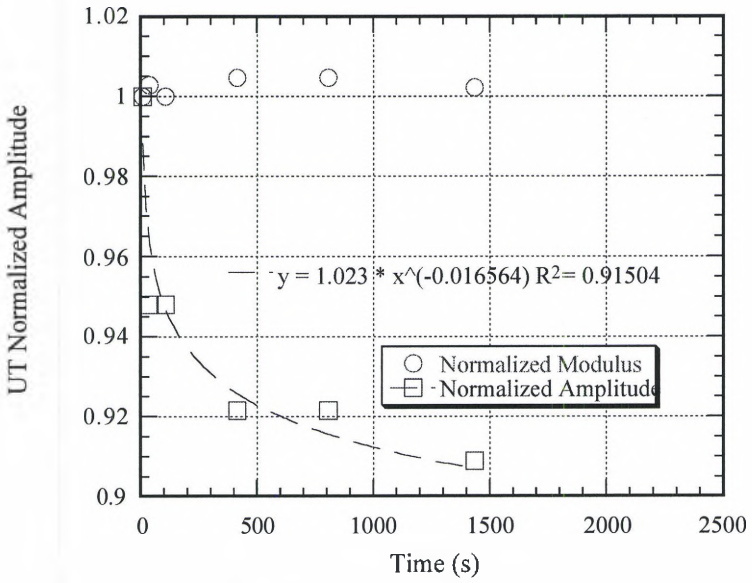

Figure 86. Modulus and amplitude data.

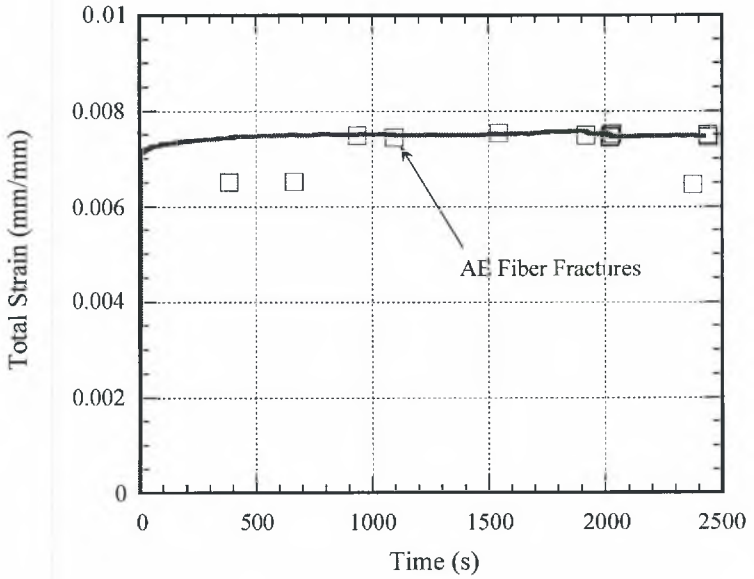

Figure 87. AE data overlaying mechanical strain data. Events deviating from the strain curve are due to error in strain recording by AE system.

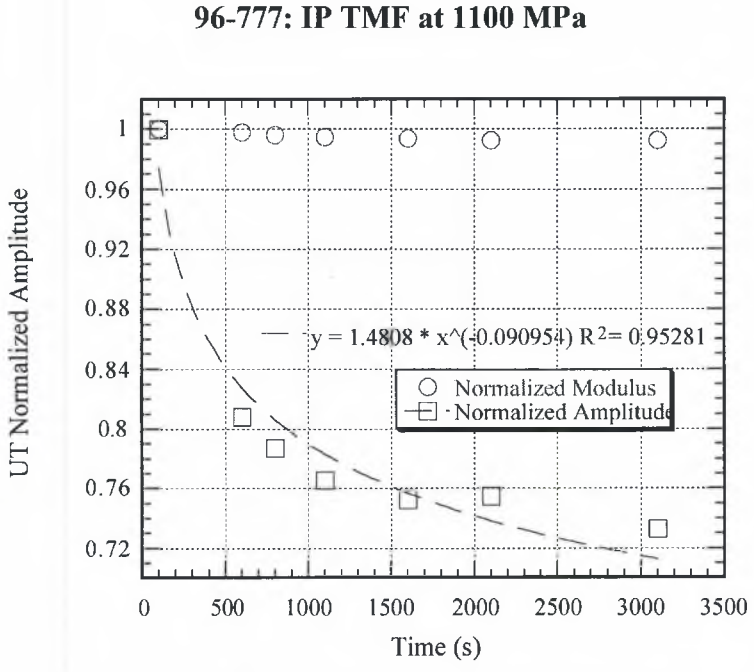

Figure 88. Modulus and amplitude data.

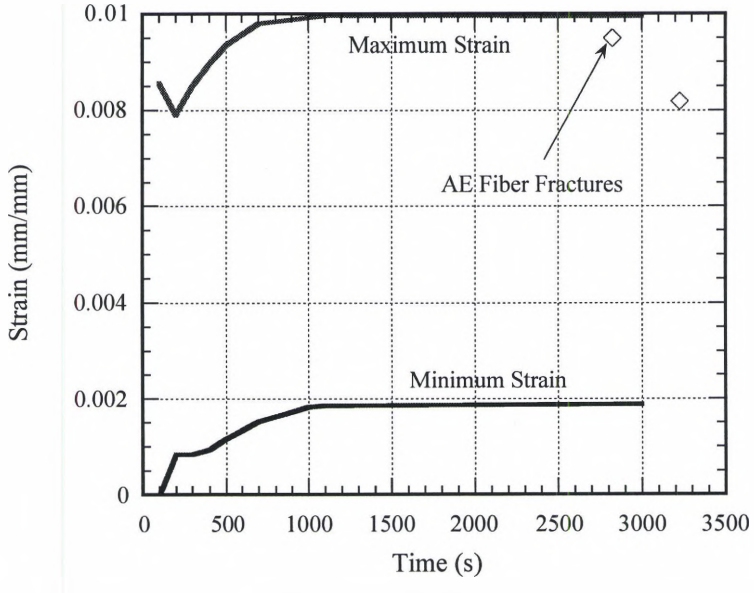

Figure 89. AE data overlaying mechanical strain data. Decrease in strain levels on AE events is due to inaccurate measurements and total specimen fracture.

96-778: Sustained Load at 1100 MPa

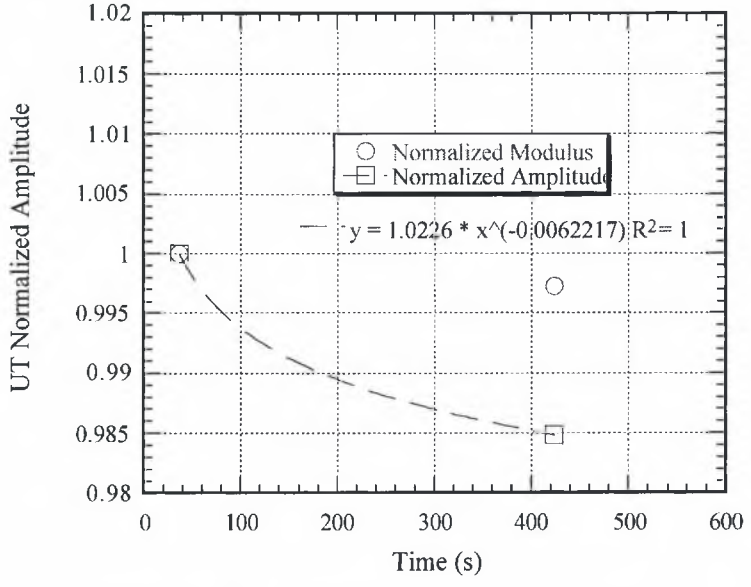

Figure 90. Modulus and amplitude data.

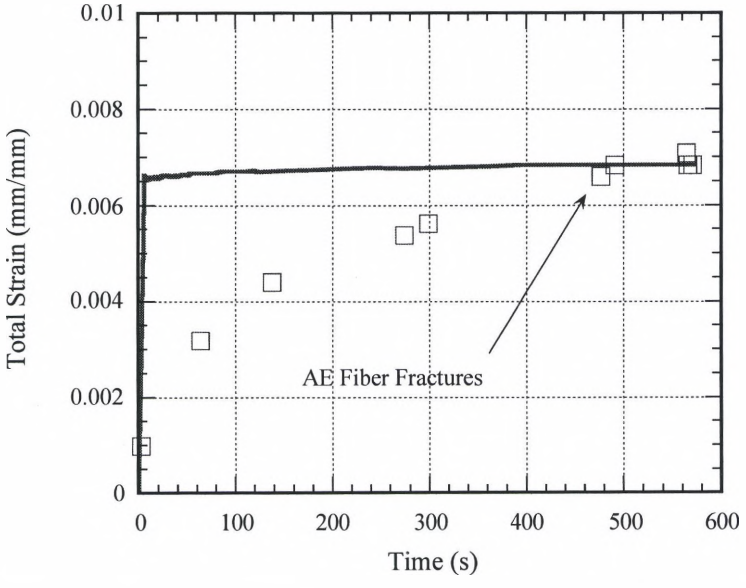

Figure 91. AE data overlaying mechanical strain data. Data confirms fracture approximately 0.25 mm from centerline. Deviation of AE strain values from mechanical data is due to inaccurate recording of strain level values by the AE system.

96-780: Sustained Load at 1050 MPa

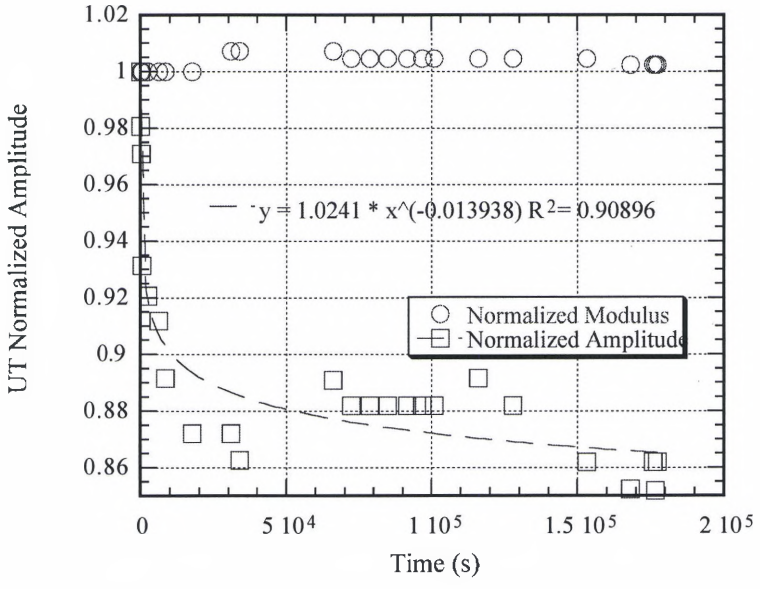

Figure 94. Modulus and amplitude data.

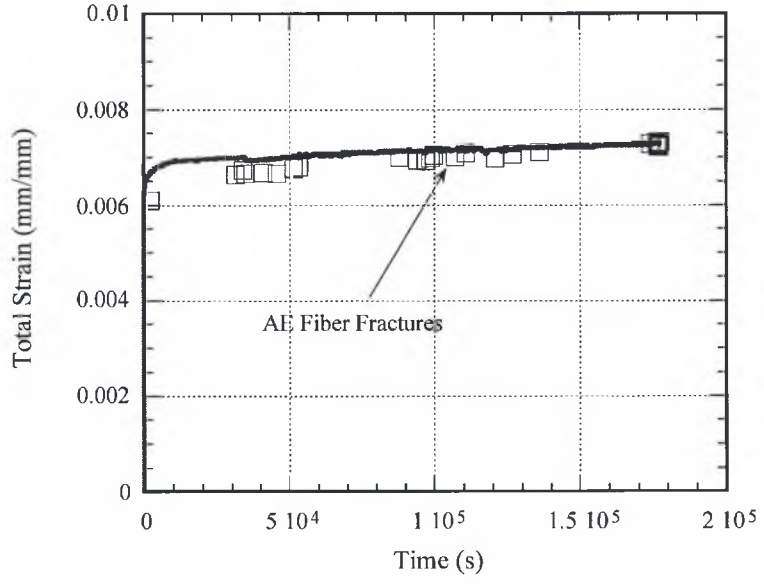

Figure 95. AE data overlaying mechanical strain data.

96-781: Sustained Load at 1000 MPa

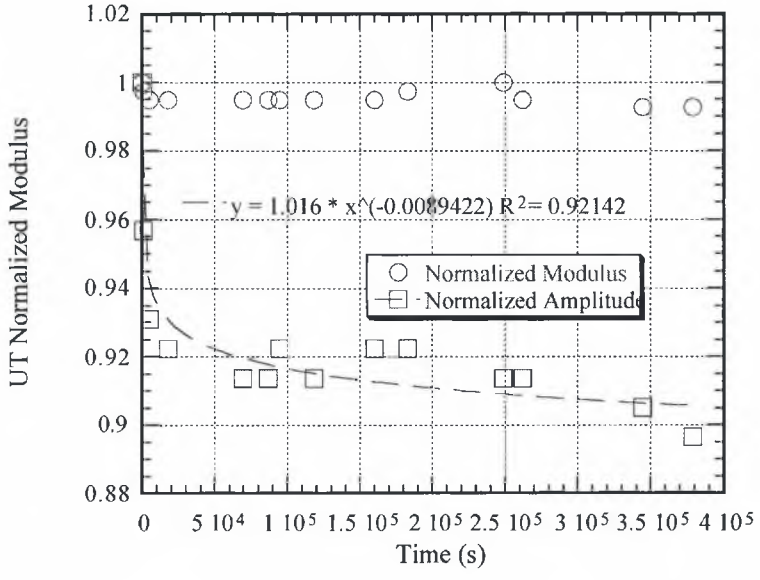

Figure 96. Modulus and amplitude data.

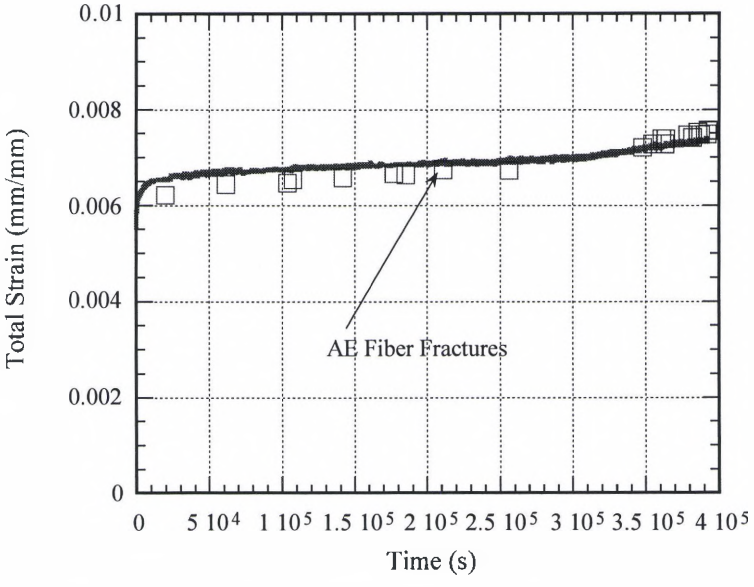

Figure 97. AE data overlaying mechanical strain data.

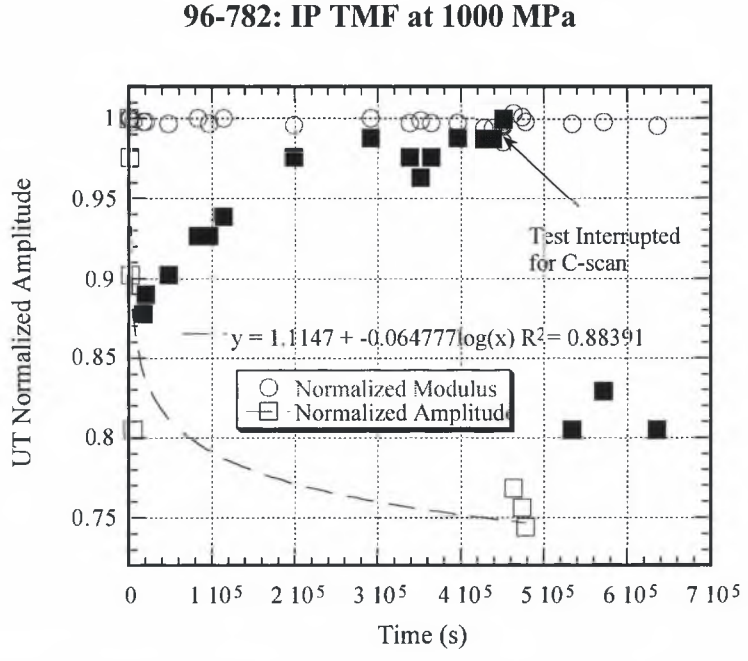

Figure 98. Modulus and amplitude data. Solid data not included in fit due to amplitude increase.

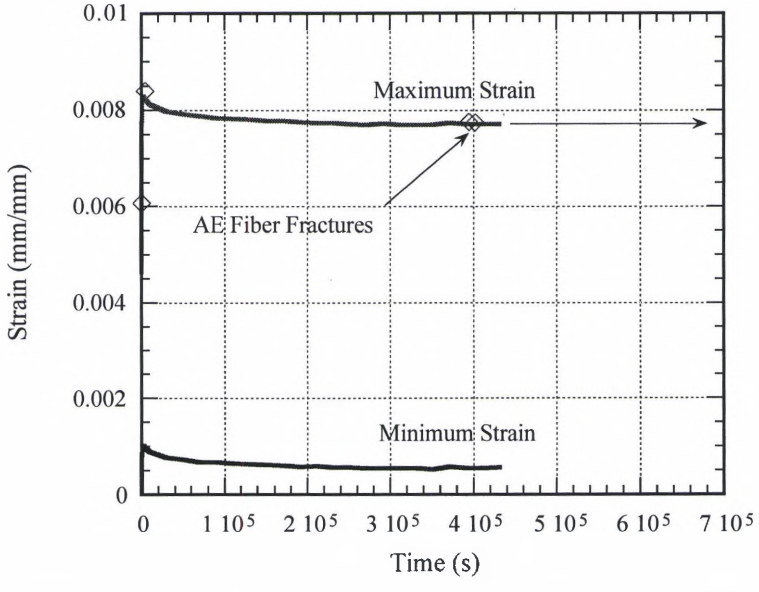

Figure 99. AE data overlaying mechanical strain data. Electrical outage caused loss of data at end of test indicated by arrow.

Appendix I

SEM Images of Composite Defects

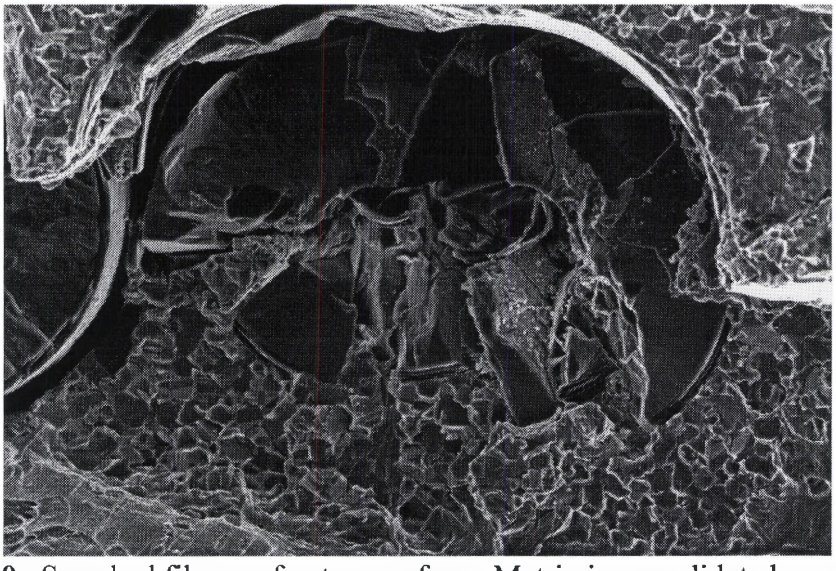

Figure 100. Smashed fiber on fracture surface. Matrix is consolidated around shards indicating fiber failure during consolidation of composite, prior to mechanical testing.

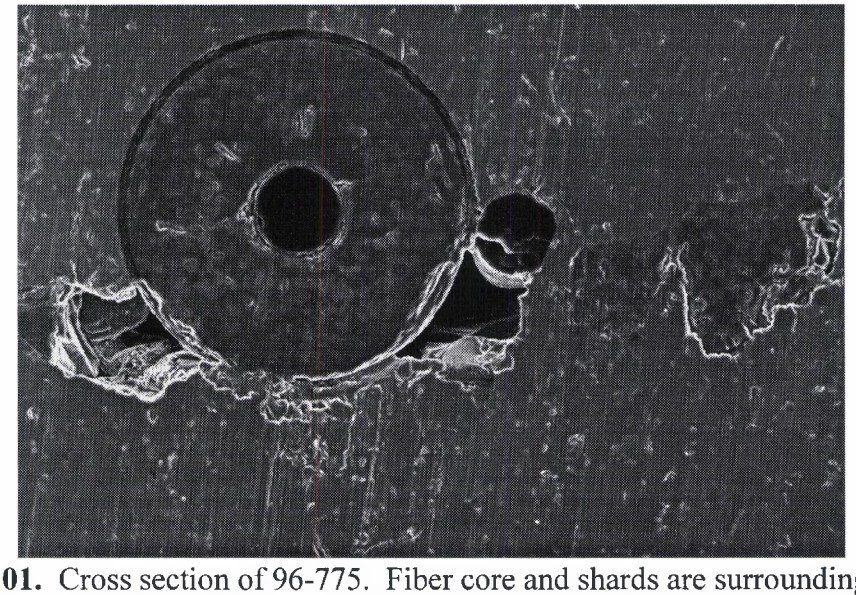

Figure 101. Cross section of 96-775. Fiber core and shards are surrounding another fiber. The matrix was unable to consolidate completely around the fiber, creating voids. This area was detected using ultrasonic immersion C-scan techniques.

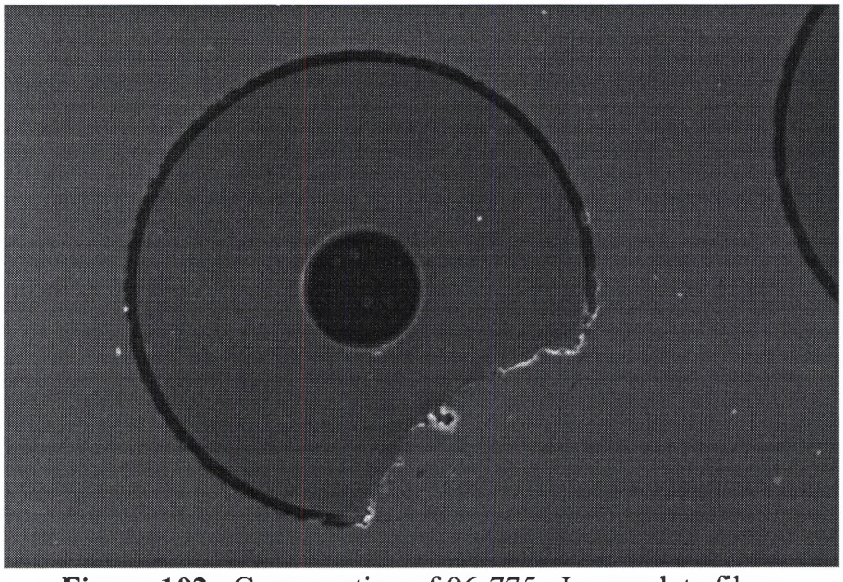

Figure 102. Cross section of 96-775. Incomplete fiber.

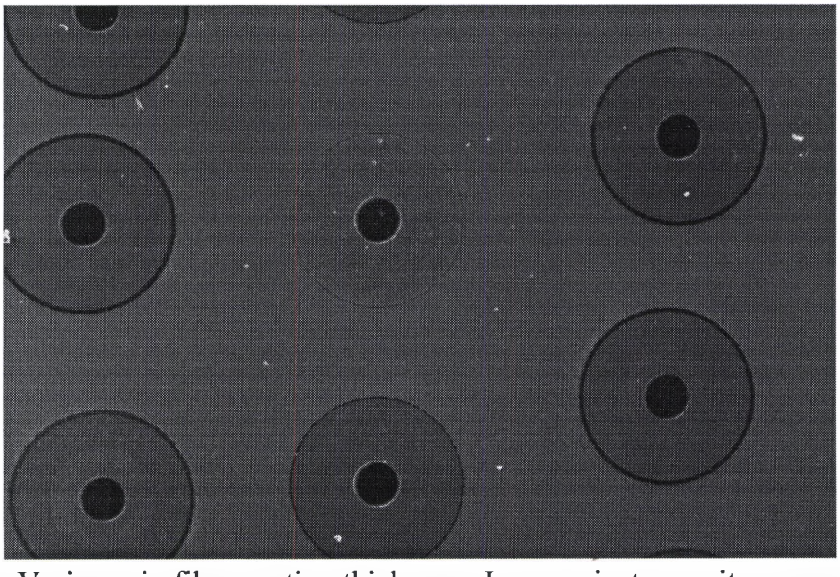

Figure 103. Variance in fiber coating thickness. In some instances it appeared that some fibers had no coating at all on the outer fiber layer.

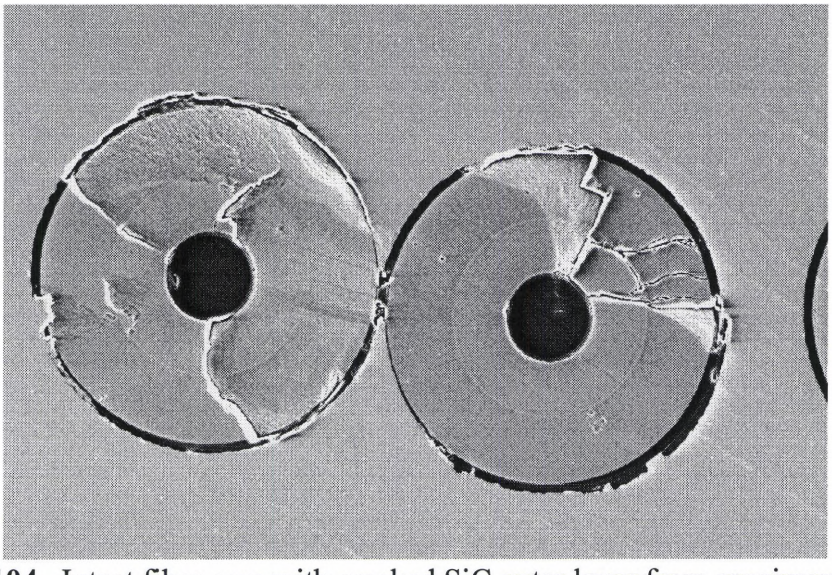

Figure 104. Intact fiber core with cracked SiC outer layer from specimen 96-776.

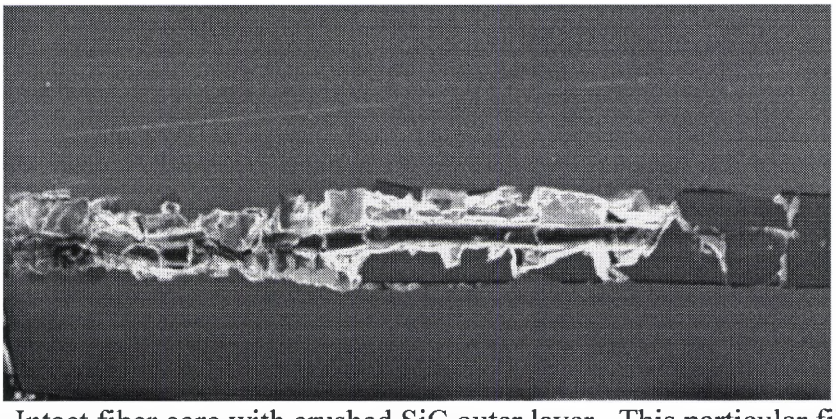

Figure 105. Intact fiber core with crushed SiC outer layer. This particular fiber appears to have been shattered through the length of the reduced section of specimen 96-775 from the high resolution UT reflector plate C-scan of the specimen shown in Figure 56.

BIBLIOGRAPHY

1. Larsen, J. M., Russ, S. M. and Jones, J. W., "**Possibilities and Pitfalls in Aerospace Applications of Titanium Matrix Composites**", *NATO Advisory Group for Aerospace Research and Development (AGARD)*, 77th Structure and Materials Panel Meeting AGARD R-796 Specialized Printing Services Limited, Loughton, Essex IG10 3TZ, 1994, pp. 1-21.

2. Johnson, W. S., "**Fatigue Testing and Damage Development in Continuous Fiber Reinforced Metal Matrix Composites**", *ASTM STP 1032*, W. S. Johnson, Ed., American Society for Testing and Materials, Philadelphia, 1989, pp. 194-221.

3. Gabb, T. P., Gayda, J. and MacKay, R. A., **"Isothermal and Nonisothermal Fatigue Behavior of a Metal Matrix Composite"**, ***Journal of Composite Materials***, vol. 24, 1990, pp. 667-686.

4. Park, Y. H., Narayen, D., Schmerling, M. and Marcus, H. L., **"Fatigue Crack Growth Behaviour of Ti-6Al-4V Metal Matrix/Continuous SiC and B_4C/B fibre Composites"**, ***Journal of Materials Science***, vol. 19, 1984, pp. 2239-2245.

5. Chan, K. S., Davidson, D. L. and Leverant, G. R., "**Relationships of Fatigue Mechanism and Crack Growth Rate in Fiber-reinforced Metal-matrix Composites**", *Advances in Fracture Research*, ICF 7, K. Salama, K. Ravi-Chandar, D. M. R. Taplin and P. R. Rao, Eds., Pergamon Press, 1989, pp. 2957-2964.

6. Chan, K. S. and Davidson, D. L., "**Fatigue Crack Growth in Fiber-Reinforced Metal-Matrix Composites**", *Fatigue of Advanced Materials*, R. O. Ritchie, R. H. Dauskardt and B. N. Cox, Eds., MCE Publications, Santa Barbara CA, 1991, pp. 325-342.

7. Bhatt, R. T. and Grimes, H. H., **"Fatigue Behavior of SiC Reinforced Ti(6Al-4V) at 650°C"**, ***Metallurgical Transactions A***, vol. 13A(11), 1982, pp. 1933-1938.

8. Ashbaugh, N., **Unpublished research on SCS-6/Ti-6Al-4V creep response**, ***University of Dayton Research Institute, 300 College Park, Dayton, OH 45469-0128***, 1996.

9. Rosenberger, A. H., **Unpublished research on SCS-6/Ti-6Al-4V IP TMF response**, ***University of Dayton Research Institute, 300 College Park, Dayton, OH 45469-0127***, 1996.

10. Nicholas, T., **Unpublished research on creep and IP TMF inefficiency factor determination**, ***Wright Laboratory Materials Directorate, Wright Patterson Air Force Base, OH. 45443***, 1996.

11. Nicholas, T. and Johnson, D. A., **"Time- and Cycle-Dependent Aspects of Thermal and Mechanical Fatigue in a Titanium Matrix Composite"**, ***Thermo-Mechanical Fatigue Behavior of Materials ASTM STP 1263***, M. J. Verrilli and M. G. Castelli, Eds., American Society for Testing and Materials, Philadelphia, 1994, pp. 331-351.

12. MacLellan, P. T., **In Situ Ultrasonic Surface Acoustic Wave Characterization of Fatigue Damage in an SCS-6/Timetal®21S Metal Matrix Composite**, Masters Thesis, University of Dayton, 1993.

13. Benson, D. M., **Nondestructive Methods for Evaluating Damage Evolution and Material Behavior in Ti-6242/Sigma Composite**, Masters Thesis, University of Dayton, 1995.

14. Buchanan, D., John, R., Stubbs, D. A., Karpur, P. and Benson, D., **"Ultrasonic Bulk and Surface Wave Methods for In Situ Monitoring of Damage in Metal Matrix and Ceramic Matrix Composites"**, ***ASTM STP 1318***, to be published in 1997.

15. Khobaib, M., John, R. and Ashbaugh, N. E., **"Sustained Load Behavior of SCS-6/Timetal®21S Composite"**, ***Life Prediction Methodology for Titanium Matrix Composites ASTM STP 1253***, W. S. Johnson, J. M. Larsen and B. N. Cox, Eds., American Society for Testing and Materials, 1996, pp. 185-207.

16. Kelly, A. and Street, K. N., **"Creep of Discontinuous Fiber Composites II. Theory for Steady State"**, ***Proc. R. Soc. Looond***, vol. A328, 1972, pp. 283-293.

17. Taya, M., **"Creep Behavior of Metal Matrix Composites"**, ***Metal Matrix Composites: Mechanisms and Properties***, R. K. Everett and R. J. Arsenault, Eds., Academic Press, 1991, pp. 189-215.

18. Mileiko, S. T., **"Steady State Creep of a Composite Material With Short Fibers"**, ***J. Mater. Sci.***, vol. 5, 1970, pp. 254-261.

19. McLean, M., **"Mechanisms and Models of High Temperature Deformation of Composites"**, ***Materials and Engineering Design The Next Decade***, B. F. Dyson and D. R. Hayhurst, Eds., Inst. of Metals, London, 1989, pp. 287-294.

20. Coker, D., Ashbaugh, N. E. and Nicholas, T., "**Analysis of Thermomechanical Cyclic Behavior of Unidirectional Metal Matrix Composites**", *Thermomechanical Fatigue Behavior of Materials ASTM STP 1186*, H. Sehitoglu, Ed., American Society for Testing and Materials, Philadelphia, 1993, pp. 50-69.

21. Khobaib, M., **"Creep Behavior of SCS-6/Ti-24Al-11Nb Composite"**, ***Titanium Aluminide Composites***, P. R. Smith, S. J. Balsone and T. Nicholas, Eds., WL-TR-91-4020, Wright Patterson AFB, OH, February, 1991, pp. 450-466.

22. Neu, R. W. and Roman, I., **"Acoustic Emission Monitoring of Damage in Metal Matrix Composites Subjected to Thermomechanical Fatigue"**, ***Composites Science and Technology***, vol. 52(1), 1994, pp. 1-8.

23. Kolsky, H., ***Stress Waves in Solids***, Dover Publications, Inc. New York, 1963.

24. Morse, R. W., **"Dispersion of Compressional Waves in Isotropic Rods of Rectangular Cross Section"**, ***The Journal of the Acoustical Society of America***, vol. 20(6), 1948, pp. 833-838.

25. Morse, R. W., **"The Velocity of Compressional Waves in Rods of Rectangular Cross Section"**, ***The Journal of the Acoustical Society of America***, vol. 22(2), 1950, pp. 219-223.

26. Prosser, W. H. and Gorman, M. R., **"Extensional and Flexural Waves in a Thin-Walled GRaphite/Epoxy Tube"**, ***Journal of Composite Materials***, vol. 26(14), 1992, pp. 2016-2027.

27. Whitney, J., ***Analytical Mechanics of Composite Materials***, Graduate Chemical and Engineering Dept., University of Dayton, Dayton, OH., 1995.

28. Graff, K., ***Wave Motion in Elastic Solids***, Ohio State U.P. Columbus, OH., 1976.

29. Gorman, M. R., **"Plate Wave Acoustic Emission"**, ***J. Acoust. Soc. Am.***, vol. 90(1), 1991, pp. 358-364.

30. Gorman, M. R. and Prosser, W. H., **"Application of Normal Mode Expansion to Acoustic Emission Waves in Finite Plates"**, ***Journal of Applied Mechanics***, vol. 63, 1996, pp. 555-557.

31. Foster, M. A., Smith, P. R. and Miracle, D. B., **"The Effect of Heat Treatment on Tensile and Creep Properties of "Neat" Ti-22Al-23Nb in the Transverse Orientation"**, ***Scripta Metallurgica et Materialia***, vol. 33(6), 1995, pp. 975-981.

32. Evans, D. J., **Study of Creep Damage Mechanisms and Steady State Creep Regime in SCS-6/Ti-6Al-4V Composites**, Masters Thesis, University of Dayton, 1990.

33. Khobaib, M., **"Damage Evolution in Creep of SCS-6/Ti-24Al-11Nb Metal-Matrix Composites"**, ***Journal of Reinforced Plastics and Composites***, vol. 12(3), 1993, pp. 296-310.

34. Schwenker, S. W., Evans, D. J. and Eylon, D., **"Longitudinal Creep Behavior and Damage in SCS-6/Ti-6Al-4V Metal Matrix Composites"**, ***Titanium '92 Science and Technology***, F. H. Froes and I. L. Caplan, Eds., TMS, Warrendale, PA, vol. 3, 1993, pp. 2593-2600.

35. Schwenker, S. W., Roman, I. and Eylon, D., **"Creep Behavior of SCS-6/Ti-6Al-4V Unidirectional Composites"**, *Advanced Composites '93: International Conference on Advanced Composite Materials*, T. Chandra and A. K. Dhingra, Eds., TMS, Pennsylvania, 1993, pp. 1169-1176.

36. Mall, S., Hanson, D. G., Nicholas, T. and Russ, S. M., **"Themomechanical Fatigue Behavior of a Cross-Ply SCS-6/ß21-S Metal Matrix Composite"**, ***Constituitive Behavior of High-Temperature Composites***, vol. 40, 1992, pp. 91-106.

37. Neu, R. W. and Nicholas, T., **"Effect of Laminate Orientation on the Thermomechanical Fatigue Behavior of a Titanium Matrix Composite"**, ***Journal of Composites Technology & Research***, vol. 16(3), 1994, pp. 214-224.

38. Neu, R. W. and Nicholas, T., **"Thermomechanical Fatigue of SCS-6/Timetal®21S Under Out-of-Phase Loading"**, ***Thermomechanical Behavior of Advanced Structural Materials***, W. F. Jones, Ed., The American Society of Mechanical Engineers, New York, vol. AD-34, AMD-173, 1993, pp. 97-111.

39. Mirdamadi, M., Johnson, W. S., Bahei-El-Din, Y. A. and Castelli, M. G., **"Analysis of Thermomechanical Fatigue of Unidirectional Titanium Metal Matrix Composite"**, *Composite Materials: Fatigue and Fracture, Fourth Volume_ASTM STP 1156*, W. W. Stinchcomb and N. E. Ashbaugh, Eds., American Society for Testing and Materials, Philadelphia, 1993, pp. 591-607.

40. Castelli, M. G., Bartolotta, P. and Ellis, J. R., **"Thermomechanical Testing of High Temperature Composites: Thermomechanical Fatigue (TMF) Behavior of SiC(SCS-6)/Ti-15-3"**, ***Composite Materials: Testing and Design*** *ASTM STP 1120,* G. C. Grimes, Ed., American Society for Testing and Materials, Philadelphia, vol. 10, 1992, pp. 70-86.

41. Neu, R. W., **"A Mechanistic-Based Thermomechanical Fatigue Life Prediction Model for Metal Matrix Composites"**, ***Fatigue Fract. Engng Mater. Struct.***, vol. 16(8), 1993, pp. 811-828.

42. Neu, R. W. and Nicholas, T., **"Methodologies for Predicting the Thermomechanical Fatigue Life of Unidirectional Composites"**, ***Advances in Fatigue Lifetime Predictive Techniques*** *ASTM STP 1292*, M. R. Mitchell and R. W. Landgraf, Eds., vol. 3, American Society for Testing and Materials, Philadelphia, 1996, pp. 1-23.

43. Russ, S. M., Nicholas, T., Bates, M. and Mall, S., **"Thermomechanical Fatigue of SCS-6/Ti-24Al-11Nb Metal Matrix Composite"**, *Failure Mechanisms in High Temperature Composite Materials*, G. K. Haritos, G. Newaz and S. Mall, Eds., Vol. AD-22, AMD-122, American Society of Mechanical Engineers, New York, 1991, pp. 37-43.

44. Castelli, M. G., **"Characterization of Damage Progression in SCS-6/Timetal®21S $[0]_4$ Under Thermomechanical Fatigue Loading"**, *Life Prediction Methodology for Titanium Matrix Composites ASTM STP 1253*, Chelsea, MI, 1996, pp. 412-431.

45. Bartolotta, P. A., Kantzos, P., Verrilli, M. J. and Dickerson, R. M., **"Environmental Degradation of an Intermetallic Matrix Composite During Thermomechanical Fatigue"**, *Fatigue '93*, J. P. Bailon and I. J. Dickson, Eds., Vol. 2, Engineering Materials Advisory Services, Ltd., 1993, pp. 1001-1006.

46. Stubbs, D. A., Russ, S. M. and MacLellan, P. T., **"Examination of the Correlation Between NDE-Detected Manufacturing Abnormalities and Ultimate Tensile Strength of Thermomechanical Fatigue Life"**, ***Cyclic Deformation, Fracture, and Nondestructive Evaluation of Advanced Materials: Second Volume*** *ASTM STP 1184,* M. R. Mitchell and O. Buck, Eds., American Society for Testing and Materials, Philadelphia, 1994, pp. 315-334.

47. Soliman, F. Y., "**Creep and Rupture of Graphite-Epoxy Composites**", *Composite Materials: Testing and Design ASTM STP 460*, Philadelphia, 1969, pp. 254-270.

48. Bakuckas Jr., J. G., Prosser, W. H. and Johnson, W. S., "**Monitoring Damage Growth in Titanium Matrix Composites Using Acoustic Emission**", ***Journal of Composite Materials***, vol. 28(4), 1994, pp. 305.

49. Chen, C. P. and Sachse, W., "**Quantitative Acoustic Emission Source Characterization of Fatigue Cracks in a Thin-Plate of 7075-T6 Aluminum**", ***Journal of Applied Physics***, vol. 64(11), 1988, pp. 6264-6273.

50. Prosser, W. H., Jackson, K. E., Kellas, S., Smith, B. T., McKeon, J. and Friedman, A., "**Advanced Waveform-Based Acoustic Emission Detection of Matrix Cracking in Composites**", ***Materials Evaluation***, September, 1995, pp. 1052-1058.

51. Hamstad, M. A. and Downs, K. S., "**On Characterization and Location of Acoustic Emission Sources in Real Size Composite Structures - A Waveform Study**", ***Journal of Acoustic Emission***, vol. 13(1/2), 1995, pp. 31-41.

52. **ASTM Standard E 976**, American Society for Testing and Materials, 1984.

53. Gorman, M. R. and Prosser, W. H., "**AE Source Orientation by Plate Wave Analysis**", ***Journal of Acoustic Emission***, vol. 9(4), 1991, pp. 283-288.

54. Gambone, M. L., **Unpublished Research on SCS fiber strengths**, ***Wright Laboratory, Materials Directorate, Wright Patterson Air Force Base, OH. 45433***, 1996.

55. Majumdar, B. and Gundel, D., **Unpublished research on fiber interfacial strengths**, ***Wright Laborator, Materials Directorate, Wright Patterson Air Force Base, OH. 45433***, 1996.

56. Karpur, P., Matikas, T. E. and Krishnamurthy, S., "**Ultrasonic Characterization of the Fiber-Matrix Interphase/Interface for Mechanics of Continuous Fiber Reinforced Metal Matrix and Ceramic Matrix Composites**", ***Journal of Composites Engineering***, vol. 5(6), 1995, pp. 697-711.

57. Matikas, T. E., Karpur, P., Pagano, N. J., Hu, S. and Shaw, L., "**In-situ Ultrasonic Characterization of Failure Strength of Fiber-Matrix Interface in Metal Matrix Composites Reinforced by SCS Series Fibers**", *21st Annual Review of Progress in Quantitative Nondestructive Evaluation*, D. O. Thompson and D. E. Chimenti, Eds., Vol. 14B, Plenum Press, Snowmass Village, Colorado, 1994, pp. 1327-1332.

58. Matikas, T. E., Karpur, P. and Dutton, R. E., **"Damage Assessment of Fiber/Matrix Interface in Ceramic Matrix Composites Using Elastic Stress Waves"**, ***High-Temperature Ceramic-Matrix Composites I: Design, Durability, and Performance***, A. G. Evans and R. Naslain, Eds., American Ceramic Society, Westerville, Ohio, vol. 57, 1995, pp. 477-482.

59. Stubbs, D. A. and Clemons, G. S., **"Screening Metal Matrix Composites Using Ultrasonic Reflector plate and X-ray Radiography Nondestructive Evaluation Techniques"**, ***Mechanical Behavior and Damage Tolerance of TMCs***, D. Stubbs, J. Larsen, S. Russ, T. Nicholas and D. Johnson, Eds., NASP Technical Memorandum 1199, vol. VII, 1995, pp. 8-19.

60. Clemons, G. S. and Stubbs, D. A., **"Guidelines for Standardizing the Gain of Ultrasonic Inspection Systems Used to Acquire Ultrasonic Reflector Plate C-scans"**, ***Mechanical Behavior and Damage Tolerance of TMCs***, D. Stubbs, J. Larsen, S. Russ, T. Nicholas and D. Johnson, Eds., NASP Technical Memorandum 1199, vol. VII, 1995, pp. 20-29.

61. Hartman, G. A. and Buchanan, D. J., "**Methodologies for Thermal and Mechanical Testing of TMC Materials**", *NATO Advisory Group for Aerospace Research and Development (AGARD)*, 77th Structure and Materials Panel Meeting AGARD R-796, Specialized Printing Services Limited, Loughton, Essex IG10 3TZ, 1994, pp. 1-9.

62. Hartman, G. A. and Ashbaugh, N. E., **"A Fracture Mechanics Test Automation System for a Basic Research Laboratory"**, ***Applications of Automation Technology to Fatigue and Fracture Testing*** *ASTM STP 1092,* Braun, Ashbaugh and Smith, Eds., 1990, pp. 95-110.

63. RMI Titanium Company, "**RMI 6Al-4V**", Central Region, 1000 Warren Avenue, Niles, Ohio 44446-1168 (330) 544-7700.

64. Yang, C. J., Jeng, S. M. and Yang, J. M., **"Interfacial Properties Measurement for SiC Fiber-Reinforced Titanium Alloy Composites"**, ***Scripta Metallurgica et Materialia***, vol. 24, 1990, pp. 469-474.

65. Schoenberg, T., "**Status of CVD SiC Monofilament at Textron Specialty Materials**", Titanium Aluminide Composites, P. R. Smith, S. J. Balsone and T. Nicholas, Eds., Wright Patterson AFB, OH., Wl-TR-91-4020, 1990, pp. 7-16.

66. Casey, J. D. and Geller, J., "**Elemental Composition Profile of SCS-6 SiC Fiber as Determined by Auger Electron Spectroscopy**", Titanium Aluminide Composites, P. R. Smith, S. J. Balsone and T. Nicholas, Eds., Wright Patterson AFB, OH, WL-TR-91-4020, 1990, pp. 59-72.